UNIVERSITY OF CALIFORNIA

Los Angeles

Characterizing Vertical Temperature and Moisture Structure in the Tropical Atmosphere: Observations and Theoretical Considerations

A dissertation submitted in partial satisfaction of the
requirements for the degree Doctor of Philosophy
in Atmospheric Sciences

by

Christopher Earl Holloway

2008

The dissertation of Christopher Earl Holloway is approved.

Bjorn B. Stevens

Robert G. Fovell

John C. H. Chiang

J. David Neelin, Committee Chair

University of California, Los Angeles

2008

DEDICATION

To my parents for always encouraging me to think and for helping me along the way, and to Gabriel for always being there even when we were apart.

Contents

List of Figures

ACKNOWLEDGEMENTS

Chapter 2 is a version of Holloway and Neelin (2007). For this chapter, the authors thank J. E. Meyerson for graphical assistance and D. Durran, E. Fetzer, E. Olsen, B. Khan, S. Bordoni, B. Medeiros, V. Savic-Jovcic, N. Lovenduski, G. Mullendore, and B. Stevens for helpful discussions. CSU data were obtained from the R. Johnson Research Group Web site. Many thanks to the AIRS project at NASA JPL, NCEPNCAR, and the CARDS project for providing data. This work was supported under National Science Foundation Grants ATM-0082529 and ATM-0645200, National Oceanic and Atmospheric Administration Grant NA05OAR4311134, and NASA Earth System Science Fellowship Grant NNX06AF83H.

Chapter 3 is a version of Holloway and Neelin (2008). For this chapter, the authors were supported in part by National Science Foundation ATM-0082529, National Oceanic and Atmospheric Administration NA05OAR4311134. JDN acknowledges the John Simon Guggenheim Memorial Foundation and the National Center for Atmospheric Research for sabbatical support. CEH was supported by NASA Earth System Science Fellowship Grant NNX06AF83H. We thank K. Emanuel, M. Hughes, B. Lesht, B. Medeiros, R. Neale, L. Nuijens, B. Stevens, J. Tribbia, X. Wu, and G. Zhang for discussions and J. Meyerson for graphical assistance.

Chapter 4 is a draft of a paper manuscript in progress coauthored with J. David Neelin. For this chapter, the authors were supported in part by National Science Foundation ATM-0082529, National Oceanic and Atmospheric Administration NA05OAR4311134. JDN acknowledges the John Simon Guggenheim

Memorial Foundation and the National Center for Atmospheric Research for sabbatical support. CEH was supported by NASA Earth System Science Fellowship Grant NNX06AF83H. We thank M. Cadeddu, M. Moncrieff, and O. Peters for helpful discussions.

I received a grant through the Chancellor's ADA (Americans with Disabilities Act) & 504 Compliance Office for my computer and ergonomic furniture. This was instrumental in allowing me to continue my research. I would like to thank the staff at the Office for Students with Disabilities and the Disabilities and Computing Program, particularly John Pedersen, for all of their help.

I would like to thank my advisor, David Neelin, for his guidance and support. David has been generous with his time and very encouraging of my ideas and my research. His own creative ideas have been instrumental in the development of this research. He has also been consistently supportive of my work and of decisions I have made based on my personal life. David has been a wonderful advisor and mentor.

Bjorn Stevens has been an important teacher and mentor to me as well. He has shared his amazing insight into convection and convective clouds. Bjorn has also made sure to check in on me and make sure I was doing well, and he has given me lots of good advice.

I would also like to thank the other members of my committee, Rob Fovell and John Chiang, for their comments and discussions that have helped this research progress. In addition I would like to thank the rest of my teachers at UCLA.

There have been numerous graduate students and researchers who have helped me enormously with both my work and with my life as a graduate student.

Of these, I am particularly grateful to Mimi Hughes, Nikki Lovenduski, Brian Medeiros, Verica Savic-Jovcic, and Simona Bordoni for providing so much support and friendship. I couldn't have done this without them. I would like to thank all of my friends, at UCLA and elsewhere, for the many good times during graduate school.

Thanks also to my parents for all their support and encouragement. Lastly, I thank my partner, Gabriel, who has stood by me for six long years and who has been my biggest supporter and my best friend.

Christopher Earl Holloway

Los Angeles, California

May, 2008

VITA

April 25, 1979	Born, New Haven, Connecticut, USA
2001	A. B., Earth and Planetary Sciences Harvard University
2002–2003	Chancellor Fellowship University of California, Los Angeles
2004	M. S., Atmospheric Sciences University of California, Los Angeles
2005	Teaching Assistant Department of Atmospheric and Oceanic Sciences University of California, Los Angeles
2006–2008	NASA Earth System Science Graduate Student Fellowship University of California, Los Angeles
2007	Bjerknes Memorial Award Department of Atmospheric and Oceanic Sciences University of California, Los Angeles
2007	Bosart Award Department of Atmospheric and Oceanic Sciences University of California, Los Angeles
2007–2008	Dissertation Year Fellowship University of California, Los Angeles

PUBLICATIONS AND PRESENTATIONS

Emanuel, K., C. DesAutels, C. Holloway and R. Korty (2004). Environmental control of tropical cyclone intensity. J. Atmos. Sci., 61, 843–858.

Holloway, C. E., (March 2007). Vertical temperature relationships in the tropics and convective quasi-equilibrium. Graded Seminar at the Department of Atmospheric and Oceanic Sciences, UCLA.

—, and J. D. Neelin (April 2006). The convective cold top and quasi-equilibrium. Presentation at the 27th Conference on Hurricanes and Tropical Meteorology, AMS, Monterey, California.

—, — (2007). The convective cold top and quasi equilibrium. J. Atmos. Sci., 64, 1467–1487.

—, — (April 2008). Moisture vertical strucutre and tropical deep convection. Presentation at the 28th Conference on Hurricanes and Tropical Meteorology, AMS, Orlando, Florida.

Neelin, J. D., O. Peters, J. W.-B. Lin, K. Hales, and C. E. Holloway (2008). Rethinking convective quasi-equilibrium: observational constraints for stochastic convective schemes in climate models. Phil. Trans. R. Soc. A, in press.

—, M. Munnich, H. Su, J. E. Meyerson, and C. E. Holloway (2006). Tropical drying trends in global warming models and observations. Proc. Nat. Acd. Sci., 103, 6110–6115.

Stevens, B., A. Beljaars, S. Bordoni, C. Holloway, M. Koehler, S. Krueger, V. Savic-Jovcic and Y. Zhang (2007). On the structure of the lower troposphere in the summertime stratocumulus regime of the northeast Pacific. Mon. Wea. Rev., 135, 985–1005.

ABSTRACT OF THE DISSERTATION

Characterizing Vertical Temperature and Moisture Structure in the Tropical Atmosphere: Observations and Theoretical Considerations

by

Christopher Earl Holloway

Doctor of Philosophy in Atmospheric Sciences

University of California, Los Angeles, 2008

Professor J. David Neelin, Chair

To improve understanding of convective processes, especially those important for convective parameterization, the vertical temperature and moisture structure of the tropical atmosphere is investigated with respect to its interaction with deep convection, mainly using observational data. The analyses test assumptions and implications of convective quasi-equilibrium, the main theoretical basis for convective parameterizations which posits that small-scale convection quickly acts to reduce vertical instability caused by slower large-scale forcing. Temperature perturbations are found to be largely in agreement with a moist-adiabatic curve, especially in the free troposphere on large enough space and time scales,

in broad agreement with quasi-equilibrium thinking. Reanalysis of meteorological data as well as climate model output appears to be overly constrained to the moist-adiabatic curve, especially in the boundary layer where observations show less agreement—this is likely due to convective parameterizations that too closely couple the boundary layer and free troposphere via deep convection. A robust negative correlation between free-tropospheric and upper-tropospheric-lower-stratospheric temperature perturbations, termed the "convective cold top", is hypothesized to derive from simple hydrostatic pressure perturbations causing divergence and quantifiable adiabatic cooling above convective heating.

Water vapor perturbations from radiosondes at Nauru in the western tropical Pacific are found to be maximized in the lower free troposphere. That layer, around 800 hPa, also contains the most variance represented by the first vertical principal component, which correlates almost perfectly with column water vapor (CWV). The sharp pick-up of precipitation at high CWV shown in previous satellite-based studies and confirmed in these radiosonde data is therefore particularly associated with a moistening of this lower-free-tropospheric layer. Entraining plume analysis shows that this transition to deep convection at high CWV is associated with higher buoyancy due to moister entrained air in the lower troposphere. Plumes using entrainment profiles based on a simple increasing mass flux profile, and including the effects of freezing, are especially skillful. An overall view of CWV as a predictor variable with relatively long autocorrelation scales that greatly increases probability of shorter-lived precipitation events near and several hours after high enough CWV values is supported by temporal analyses of microwave radiometer CWV and its relationship to precipitation.

Chapter 1

Introduction

Relating small-scale cumulus convection to large-scale dynamics is a long-standing problem in atmospheric science. For any model with a horizontal and vertical grid scale of more than a few kilometers, some kind of large-scale parameterization must be used to estimate the overall effects of convection within each model grid box without directly simulating convection itself. Quasi-equilibrium assumptions, the theoretical basis for most convective parameterizations, hold that buoyancy is consumed by convection as fast as it is created by large-scale forcing (defined as any process leading to vertical instability measured at the grid scale), so that for large enough space and time scales in the tropics moist static energy is constrained to a specific reference profile shape (c.f. Arakawa 2004 and references therein). However, models show great sensitivity to the type of convective parameterization used (Slingo et al. 1996).

As computers become faster, there is hope that global climate models (GCMs) will be able to resolve deep convection, ultimately removing the need for convective parameterizations. However, even operational forecasts using global cloud-system resolving models (CRMs) are still many years away—climate simulations using such models are further still. An approach using 2-D CRMs embedded in large GCM grid cells, known as "superparameterization" or multiscale modeling framework (Grabowski and Smolarkiewicz 1999; Khairoutdinov and Randall 2001), shows encouraging preliminary results. However, this framework, until and unless it becomes completely cloud-system resolving, will still rely on assumptions and approximations regarding how to represent large scale variance (c.f. Neelin et al. 2008), propagation, and organization based on the CRM information, and how best to communicate information between the different scales. Therefore, the need for parameterizations of deep convective processes will remain for very practical reasons.

The idea of convective parameterization is important from an intellectual perspective as well. If a seemingly random, relatively small-scale process can be explained in terms of an adjustment to large-scale equilibrium, this adds to our theoretical understanding of the atmosphere. Indeed, many advances in tropical climate theory have arisen from the application of quasi-equilibrium ideas which largely were developed for practical applications in climate and weather modeling. Simplifications based on quasi-equilibrium also form the basis for many conceptual models of the tropics.

One important means of advancing quasi-equilibrium theory is by testing some of its assumptions and implications in observational data. Models using convective parameterizations must be constrained by built-in quasi-equilibrium ideas, particularly regarding the vertical structure of heating and moistening and the distribution and variance of precipitation. How constrained are observations in respect to these quantities? Can temperature and moisture perturbations be usefully described by a few simple vertical structures, as in some simple models? As observations grow in accuracy and coverage, what new insight can they provide into the relationships between deep convection and the vertical structure of temperature and moisture perturbations in the tropics?

To help answer these questions, we start in Chapter 2 by analyzing the vertical structure of temperature perturbations in satellite data, radiosondes, and reanalysis. Gravity waves smooth out temperature gradients quickly in the tropics, since the Coriolis force is very weak (Nicholls et al. 1991). This means that temperatures could theoretically approach a single temperature profile, or rather a series of profiles (quasi-equilibria) that represent a balance between convective heating and large-scale forcing toward vertical instability consisting of radiative cooling, surface fluxes, and advection (Manabe et al. 1965; Betts 1973; Arakawa and Schubert 1974). Intermediate complexity models such as the quasi-equilibrium tropical circulation model (QTCM; Neelin 1997; Neelin and Zeng 2000) assume that temperature can be expressed by coherent vertical structures—this is one assumption that we test in our analyses. We also test whether temperature perturbation profiles resemble those predicted for a hypothetical series of moist adiabats, which are neutrally buoyant to saturated parcels lifted from their base and therefore form the basis of the proposed quasi-equilibria shapes in the literature.

In some ways, the problem of moisture vertical structure is a more difficult one than temperature. There are no remote mechanisms acting to decrease moisture gradients, so moisture is controlled locally by evaporation, advection, and precipitation. Although satellite measurements, namely those from the Atmospheric Infrared Sounder (AIRS) instrument, have begun to give a glimpse of the vertical structure of water vapor at global coverage, these data are still relatively hobbled by their inability to penetrate clouds (see section 2.2.1). This makes them suitable for temperature signals, which are spread rapidly by gravity waves, but less so for moisture. We therefore focus our efforts in Chapter 3 on radiosondes and precipitation rates from the well-observed Atmospheric Radiation Measurement (ARM) site at Nauru in the western tropical Pacific.

We use the data to relate vertical structures of water vapor variability to deep convection, again motivated by a desire to better constrain assumptions behind convective parameterizations, including stochastic ones. Since the most easily observed measurement of atmospheric moisture is column water vapor (CWV), obtained by microwave satellite instruments even within most clouds, we characterize the structure of moisture variability associated with changes in CWV.

We then link this vertical structure, via entrainment, to empirical satellite-based studies showing a sharp pick-up of precipitation at high CWV values (Bretherton et al. 2004; Peters and Neelin 2006). Many studies have suggested that dry air in the free troposphere is unfavorable to deep convection, with entrainment of this dry air, and subsequent reduction of updraft buoyancy, being the most likely cause of this relationship (Austin 1948; Malkus 1954; Brown and Zhang 1997; Parsons et al. 2000; Tompkins 2001b; Grabowski 2003; Derbyshire et al. 2004). We therefore explore simple entrainment profiles based on increasing mass flux through a deep lower-tropospheric layer—these non-constant entrainment profiles have been seen in large eddy simulations of shallow convection (Siebesma et al. 2007). Since they weight the resulting plume mixture more evenly throughout the lower troposphere, these profiles are especially relevant to questions about the effects of CWV on entraining plume buoyancy.

Having associated CWV with a characteristic moisture perturbation profile, in Chapter 4 we explore the CWV/precipitation relationship at high temporal resolution using microwave radiometer and optical gauge observations at Nauru. Here we attempt to better characterize the precipitation pick-up at high CWV at different lags, investigating the potential for CWV as a predictor of precipitation in models. We also look at the variability of the onset of precipitation events and their size distributions as a function of CWV, testing some implications of viewing precipitation as a continuous phase transition (Peters et al. 2002; Peters and Neelin 2006).

Chapter 2

The Convective Cold Top and Quasi Equilibrium

Abstract

To investigate dominant vertical structures of observed temperature perturbations, and to test the temperature implications of the convective quasi-equilibrium hypothesis, the relationship of the tropical temperature profile to the average free-tropospheric temperature is examined in Atmospheric Infrared Sounder (AIRS) satellite data, radiosonde observations, and National Centers for Environmental Prediction-National Center for Atmospheric Research (NCEP-NCAR) reanalysis. The spatial scales analyzed extend from the entire Tropics down to a single reanalysis grid point or radiosonde station, with monthly to daily time scales. There is very high vertical coherence of free-tropospheric temperature perturbations. There is also fairly good agreement throughout the free troposphere between observations and a theoretical quasi-equilibrium perturbation profile calculated from a distribution of moist adiabats. The boundary layer is fairly independent from the free troposphere, especially for smaller scales.

A third vertical feature of the temperature perturbation profile is here termed the "convective cold top" — a robust negative correlation between temperature perturbations of the vertically averaged free troposphere and those of the upper troposphere and lower stratosphere. The convective cold top is found for observations and reanalysis at many temporal and spatial scales. Given this prevalence, the literature is reviewed for previous examples of what is likely a single phenomenon. One simple explanation is proposed: hydrostatic pressure gradients from tropospheric warming extend above the heating, forcing ascent and adiabatic cooling. The negative temperature anomalies thus created are necessary for anomalous pressure gradients to diminish with height.

2.1 Introduction

This study addresses the typical vertical structure of temperature perturbations in the tropical atmosphere. Assumptions regarding the effects of deep convection on temperature structure are implicit in most large-scale tropical models. More specifically, convective parameterizations being used in current climate models typically involve the consumption of buoyancy and an explicit or implicit relaxation toward a neutral reference profile. Commonly, this reference profile is related to a moist adiabat originating from a parcel in the atmospheric boundary layer. The idea that convection consumes vertical instability, such as convective available potential energy (CAPE), at roughly the rate that it is created by large-scale forcing, is generally called the quasi-equilibrium (QE) theory and is clearly presented in Arakawa and Schubert (1974); it can also be found in various forms in Manabe et al. (1965), Betts (1973), Betts and Miller (1986), Emanuel (1991), Moorthi and Suarez (1992), Randall and Pan (1993), Zhang and McFarlane (1995), and Raymond (1997).

One application of QE theory involves simplifying temperature and moisture structure in the vertical for use in intermediate complexity models, such as the quasi-equilibrium tropical circulation model (QTCM; Neelin 1997; Neelin and Zeng 2000). The main assumption made by such a model is that most of the tropospheric variance can be represented by coherent vertical structures for temperature and moisture that in turn lead to simplified prediction of baroclinic pressure gradients and precipitation, respectively. To calculate baroclinic pressure gradients and resulting velocity fields, the shape of the vertical temperature structures is important.

This study tests both the ability to represent the vertical temperature structure in a simplified manner and the adherence to a moist-adiabatic perturbation profile as predicted by QE. Note that these are two separate questions, although there is evidence that QE should have an important constraining effect in the Tropics (Arakawa 2004).

Several studies have used observations to determine whether and to what degree quasi equilibrium holds. Xu and Emanuel (1989) found that soundings over the western Pacific were nearly neutral to moist adiabats lifted from the upper boundary layer. Brown and Bretherton (1997) found significant correlations between vertical mean temperatures in the troposphere and boundary layer equivalent potential temperature (θ_e), but the constants of proportionality were about half of those predicted by strict QE. Sobel et al. (2004) found fairly large correlations between boundary layer and lower-tropospheric temperatures but lower correlations with upper-tropospheric temperatures. One challenge faced by all of these studies is exactly which boundary layer parcel, in terms of horizontal and vertical location, to choose when making comparisons to free-tropospheric observations. Another challenge is the relatively sparse data available over the tropical oceans.

The present study largely sidesteps the first challenge by regressing temperature perturbations at each level on the vertically averaged free-tropospheric perturbations, and comparing these with corresponding regressions calculated from a range of moist adiabats. This makes the comparisons less sensitive to the specific moist adiabat used, and thus to the specific boundary layer conditions measured locally. We also investigate the degree of vertical coherence of perturbations independent of the particular shape found. Radiosondes, Atmospheric Infrared Sounder (AIRS) satellite data, and National Centers for Environmental Prediction-National Center for Atmospheric Research reanalysis (NCEP-NCAR) are used to maximize the range of time and space scales. A highly coherent free troposphere at all scales and for all datasets is found, with reasonably moist-adiabatic regression curve shapes.

One result not expected from simple QE theory, discussed in section 2.5, is the significant and robust negative correlation between temperature perturbations near and above the tropopause and those of the vertically averaged free troposphere. We refer to this phenomenon here as the "convective cold top," although this assumes that on the analyzed time scales perturbations of vertically averaged free-tropospheric temperature are directly related to deep convection. Given the prevalence with which we encounter this feature, it is not surprising that many previous publications contain instances of what appear to be, in retrospect, similar phenomena. Section 2.5.1 is a brief review of the relevant literature. We argue that one simple explanation can explain why this result is so prevalent. We show that even in a simple linear model in hydrostatic balance broad ascent and thus adiabatic cooling occur slightly above the maximum extent of the convective heating. Negative temperature anomalies are required by simple dynamical constraints. In addition to addressing the coherent free-tropospheric temperature structure and the convective cold top, we note the relative independence of the boundary layer, although this is not our main focus.

Section 2.2 is a description of the data used in this study, followed by the data analysis method in section 2.3 and analysis results in section 2.4. Section 2.5 discusses the convective cold top in relevant literature and in a simple model, and expands our explanation for it. A summary follows in section 2.6.

2.2 Observations and data

2.2.1 AIRS satellite data

We use level-2 version 4 AIRS satellite data soundings averaged over horizontal boxes within 15°S–15°N at standard pressure levels (1000, 925, 850, 700, 600, 500, 400, 300, 250, 200, 150, 100, 70, 50, 30, 20, 15, and 10 hPa). Each footprint has 45 km × 45 km horizontal resolution. The AIRS instrument is aboard the polar-orbiting Aqua satellite and combines microwave passive radiation with infrared radiation, allowing for more accurate vertical representations of temperature and moisture. Daily values have been found by averaging twice-daily swath profiles occurring in each box in a given 24-h period. Only the highest quality (total profile flag = 0) soundings have been retained, meaning mainly those over the ocean and outside of heavily clouded regions (see Susskind et al. 2003). The temperature data at this quality level have rms differences of 1 K or less in the free troposphere, around 1 K near the surface, and around 2 K or less in the lower stratosphere, when compared to collocated and coincident radiosondes, with biases of 0.2 K or less at most levels and up to 0.8 K above the tropopause (Divakarla et al. 2006; Tobin et al. 2006).

The daily time scale data analyzed range over the two years from 19 November 2003 to 18 November 2005, with two missing days. The first three harmonics of the seasonal cycle and an independent 2-yr harmonic [to account for the quasi-biennial oscillation (QBO)] have been removed (see section 2.3). For the smallest spatial scale over half the days were missing, so that the next largest spatial-scale data (10°S–10°N, 140°E–180°) were used on missing days only for purposes of finding harmonics. The monthly time scale was found by averaging the anomalies into 24 monthly values.

2.2.2 CSU TOGA COARE gridded rawinsonde data

The Colorado State University (CSU) sounding data (Ciesielski et al. 2003) come from four months of the Tropical Ocean Global Atmosphere Coupled Ocean-Atmosphere Response Experiment (TOGA COARE) dataset, provided by the R. Johnson research group. These months are during the Intensive Observing Period (IOP), November 1992–February 1993. The source data are from a merged profiler-rawinsonde dataset (Ciesielski et al. 1997) and sounding data from other Priority Sounding Sites (PSSs). These temperature and moisture data are available on a horizontal 1° × 1° latitude-longitude grid at 25-hPa vertical resolution. They have been analyzed at standard pressure levels (as in AIRS, except above 150 hPa there are levels every 25 hPa up to 25 hPa), and the 4 times daily analyses have been averaged into daily values.

2.2.3 CARDS radiosonde data

Three stations on Pacific warm pool islands have been selected from the Comprehensive Aerological Reference Dataset (CARDS; Eskridge et al. 1995) because of their locations and their almost 50 shared years of observations (1953–99). The three stations are Koror (7.3°N, 134.5°E), Chuuk (7.5°N, 151.8°E), and Majuro Atoll (7.1°N, 171.4°E). The CARDS data have 50-hPa vertical resolution between 1000 and 100 hPa, and then include 70-, 50-, and 30-hPa levels above, and have been subjected to a rigorous quality control process by the data team (Eskridge et al. 1995). We have averaged all available daily data into monthly values and then removed the seasonal cycle. The much smaller sample size for pressure levels above 250 hPa (around 85 months, almost all at the very end of the larger time series) made it necessary to slightly adjust the domain of the vertical average being used in our regressions for CARDS data (and the accompanying moist-adiabatic slope curve) from 850–200 to 850–250 hPa. Note that the CARDS dataset has now been superseded by the Integrated Global Radiosonde Archive, although for the purposes of this study there are no major differences (Durre et al. 2006).

2.2.4 NCEP-NCAR reanalysis

The NCEP-NCAR reanalysis (Kalnay and coauthors 1996) consists of model initialization data with assimilated observations that have been analyzed with a GCM in a consistent manner over many years. Temperature data are located on a $2.5° \times 2.5°$ horizontal grid at standard pressure levels (as in AIRS, except without the 15-hPa level). The years 1979–2003 are used because of better data quality in the satellite era. Monthly anomalies are taken for the entire period to remove the seasonal cycle. Daily data have been used for the same two years as the AIRS data, with the same harmonics removed, for comparison purposes. For monthly anomalies, we have removed the four months of the IOP of TOGA COARE (November 1992–February 1993) because of problems during those four months with the assimilation of TOGA COARE data leading to significant temperature outliers in the Pacific warm pool region. NCEP-NCAR is a useful proxy for QE-type behavior, since it assimilates real data but relies on a large-scale numerical assimilation model, which in turn uses a relaxed Arakawa-Schubert convective parameterization with a quasi-equilibrium closure that for deep convection relies on a moist-adiabat-like test of CAPE, accounting for entrainment, for boundary layer parcels (Pan and Wu 1995).

2.2.5 Analysis regions

To compare several different sources of data at many spatial scales in the Tropics, we have defined a few main horizontal boxes for our analyses. We focus on tropical regions, centering our smaller boxes over the Pacific warm pool, an area of active convection where TOGA COARE data was available. We also analyze one largely nonconvecting region in the eastern tropical Pacific.

The exact boundaries of these boxes differ slightly with each dataset. For instance, the latitude-longitude boundaries listed for NCEP-NCAR refer to the grid points used, so that the actual range covered extends 1.25° beyond the stated range. Similarly, the range covered by the CSU TOGA COARE gridded dataset extends 0.5° beyond the stated range. The boundaries in the case of AIRS data refer to the centers of footprints included (and each footprint is 45 km wide). AIRS data are also only over oceans and a few large lakes, and outside regions with high cloud liquid water, as discussed above. The CARDS data used are an average of three radiosonde stations on Pacific islands on or near the line 7°N, 135°–170°E, so we use that label on CARDS plots.

2.3 Method of analysis

This analysis tests the coherence of temperature perturbations in the vertical with an emphasis on the free troposphere, where relatively fast-moving gravity waves caused by deep convection are assumed to spread uniform temperature signals over large regions in short amounts of time (on the order of 1 h over 100 km; Nicholls et al. 1991). At each pressure level, temperatures have been regressed on free-tropospheric column average temperatures and the linear regression coefficient (slope) has been plotted. This approach is related to that used in Fig. 3 of Chiang and Sobel (2002), which shows regressions on monthly anomalies of NCEP-NCAR temperatures (from 800 to 5 hPa) of the first principle component of the same temperature perturbations from 750 to 200 hPa. The first principle component in that study had a 0.95 linear correlation coefficient with the same time series of microwave sounding unit (MSU) channel-2 tropospheric temperature, a measure of vertical average temperature.

For comparison to the regression analysis on the temperature data, the corresponding analysis has been done for a distribution of reversible moist adiabats (neglecting ice). Note that although we refer to these profiles as moist adiabats, they begin along a dry adiabat until reaching the lifting condensation level (LCL), which occurs between 925 and 900 hPa. First, 60 evenly spaced parcels are given a range of temperatures at 1000 hPa, starting with constant relative humidity. For the cases presented in this article, all moist-adiabatic slope curves come from the same temperature range (298–301 K) and the same relative humidity (83%) at 1000 hPa. These values are typical of warm tropical regions under precipitating conditions, as discussed in the appendix. A sensitivity analysis using the daily NCEP-NCAR 1000-hPa data, also described in the appendix, found very little variability in tropical tropospheric regression coefficients. The code for calculating the moist adiabats comes from a script included with Emanuel (1994). These slopes could alternatively have been calculated analytically using a moist-adiabatic equation linearized around a specific moist adiabat. However, we chose the current method because it works just as well, more exactly parallels our data analysis method, and allows us to use ranges of values to make a linear approximation across the nonlinear range (though admittedly the linearization made from the moist adiabat at the center of the range is virtually indistinguishable from our result). This moist-adiabatic perturbation profile lines up closely with the temperature perturbation profile used for the QTCM based on an analytical linearization around the equation for a moist pseudoadiabat (Neelin and Zeng

2000).

At daily time scales for NCEP-NCAR and AIRS we removed the first 2-yr harmonic, since it is independent of the three seasonal cycle harmonics removed and since the QBO cycle over the particular two years analyzed seems to be fairly close to a 2-yr period, based on the National Oceanic and Atmospheric Administration (NOAA) Climate Prediction Center data. The variability associated with this harmonic is small in the troposphere, but significant above the tropopause, and it is clearly of much larger time scale than those of interest for daily data. We did not remove any QBO-related cycle from the longer time series because of difficulties in characterizing a quasi-periodic phenomenon, although this would be useful in future work.

Figure 2.1 shows an example of a scatterplot used to determine one linear regression coefficient (slope). The y axis is the temperature anomaly at a given pressure level (in this case 400 hPa), while the x axis is the free-tropospheric average temperature anomaly between 850 and 200 hPa. Each point represents a single time (1 day in this example) averaged over the spatial box shown. The slope of the linear regression line is the value that will appear in later figures. The dashed gray line represents the same regression using a series of moist adiabats, shifted in position for clarity (the scatterplot is not shown but is almost indistinguishable from a straight line, with a correlation coefficient of 1). Note that all moist-adiabatic slopes shown in the following figures are the same; they do not depend in this study on spatial or temporal considerations.

Our plots of correlation coefficients include gray shading between the positive and negative critical values of statistical significance at the 95% level. To account

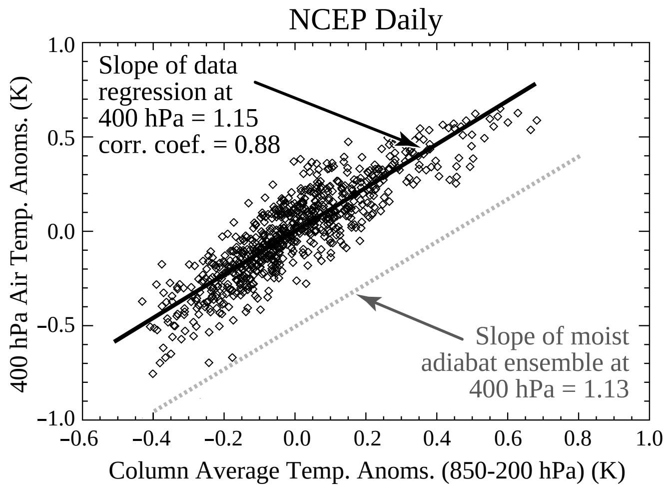

Figure 2.1: Schematic showing the method of regression analysis, for NCEP-NCAR reanalysis temperature anomalies, November 2003–November 2005, 15°S–15°N. The slope of each line will be represented in subsequent figures by single regression coefficient values at that pressure level, with the correlation coefficient on another, similar plot.

for autocorrelation, we calculate the critical value using Student's t test, but with the effective sample size in place of the actual sample size:

$$N_{eff} = N\frac{(1 - r_1 r_2)}{(1 + r_1 r_2)},$$

where N_{eff} is the effective sample size, N is the original sample size, and r_1 and r_2 are the lag-1 autocorrelations of the two time series (Bretherton et al. 1999). Differences between adjacent critical values of less than 0.05 are rounded upward for clarity, provided that the rounded values are not close to the actual data points at their respective levels. Although the correlation coefficients within the free troposphere will be slightly inflated using our method, since temperatures at those levels are also included in the vertical average, tests using vertical averages excluding the actual level in each regression show only about 1%–2% differences for all but the two outermost levels, and differences in correlation coefficients of around 0.01, with a maximum difference of 0.03, again at the outermost levels.

Unlike Brown and Bretherton (1997), we do not include regressions made by reversing our dependent and independent variables. Since the vertical average temperature incorporates many relatively independent temperature observations, it should generally have less noise than the temperature at any given level. Therefore, to minimize regression error, the vertical average is more suitable as an independent variable.

2.4 Vertical structure across scales

2.4.1 Comparison across spatial scales

Figure 2.2a shows linear regression coefficients for temperature at each pressure level regressed on free-tropospheric vertically averaged temperature for two years of NCEP-NCAR daily anomalies at four spatial scales, ordered from largest to smallest, along with the moist-adiabatic regressions discussed in section 2.3. One simple interpretation of the regression coefficients is that each value represents the change of temperature at a single level associated with a 1-K increase of free-tropospheric temperature. To illustrate, the slope in Fig. 2.1 appears as a single point at 400 hPa in the top-left panel in Fig. 2.2a, and the moist-adiabatic slope in Fig. 2.1 appears as the point on the gray line at 400 hPa in all four panels in Fig. 2.2a. The correlation coefficient for Fig. 2.1 likewise appears in the left panel in Fig. 2.2b.

We present the NCEP-NCAR data first in order to calibrate our analysis using a dataset that should be constrained by a version of QE when and where there

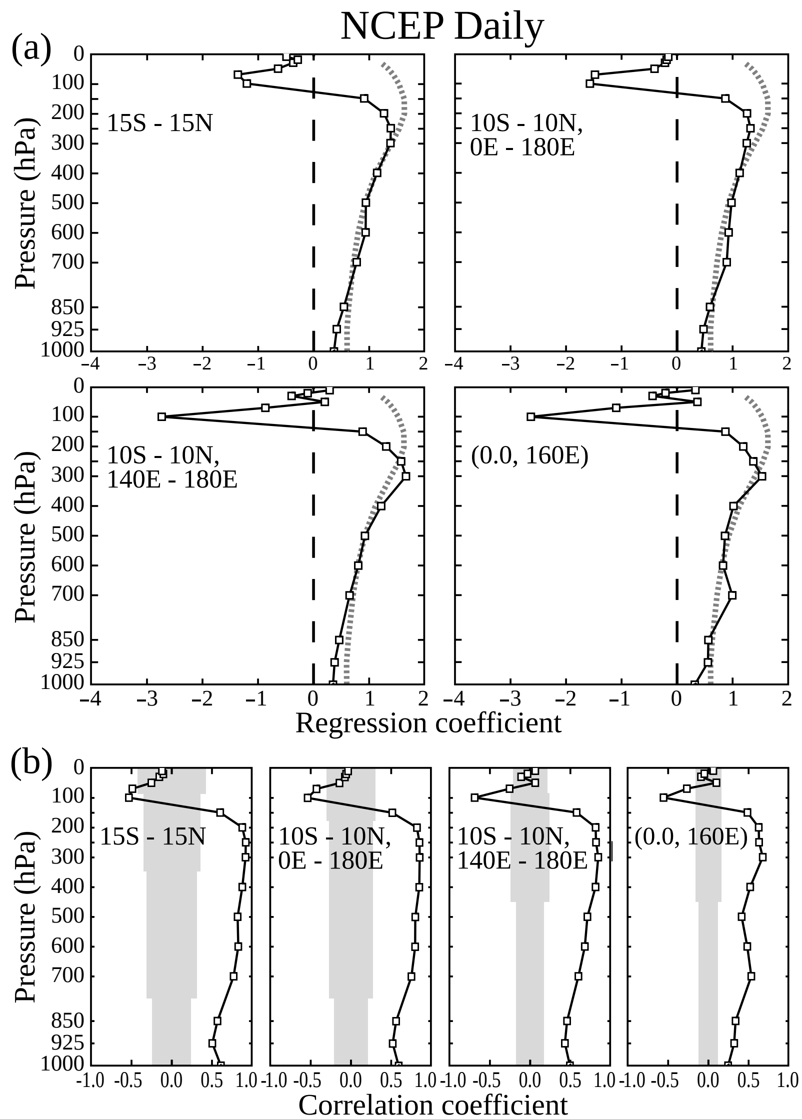

Figure 2.2: NCEP-NCAR November 2003–November 2005 daily anomalies (with three harmonics of the seasonal cycle, and a 2-yr harmonic, removed) for four tropical boxes. (a) Regression coefficients (squares) with moist-adiabatic curve (dashed gray line). (b) Correlation coefficients with gray shading between the critical values for 95% significance.

is deep convection (see section 2.2.4). It is expected that NCEP-NCAR, when compared with pure observations, should have higher correlations reaching even into the boundary layer and closer agreement with the moist-adiabatic curve. Below the LCL, even a strict QE parameterization will have departures from the moist-adiabatic curve since these are only temperature regressions, neglecting the degree of freedom introduced by variable relative humidity.

The values in Fig. 2.2a agree surprisingly well with the moist-adiabatic curve in the troposphere, especially in the free troposphere from 700 to 250 hPa. This middle layer also consistently has the highest correlation coefficients as seen in Fig. 2.2b, especially in the largest regions. The large correlation coefficients in the free troposphere may be partly expected because the quantity being regressed on is simply the free-tropospheric vertical average (see section 2.3), but there is still obviously a high level of coherence among different levels within this layer, and there would be no purely statistical reason to expect the particular regression coefficients to line up with the moist-adiabatic ones. Also, the free-tropospheric average used in the regressions includes 850 hPa, which nevertheless has correlation coefficients and regression coefficients typical of the boundary layer. In fact, repeating the regression analysis using the full-tropospheric vertical average, or alternatively the 400- or 500-hPa temperature only, in place of the free-tropospheric average does not significantly change this agreement in the free troposphere or the features present at other levels.

Above the troposphere, there are always large negative regression and correlation coefficients at some level or levels (i.e., the convective cold top). This is clearly a departure from the moist-adiabatic curve, which is positive at every level. Adherence to that curve is not expected to be as strong at levels that deep convective elements seldom reach, but the negative values clearly require explanation. The negative regression coefficients making up the convective cold top in Fig. 2.2a are larger for the smallest regions (although this is not true for the AIRS data).

There is a significant departure from the moist-adiabatic regressions in the "boundary layer" (which we use hereafter for 1000–850 hPa), with generally lower correlation coefficients as well. Possible reasons for this departure are discussed above and in section 2.6. The boundary layer in general has slightly higher correlations at larger scales.

Figure 2.3 shows the same regions (but only over oceans) and years as Fig. 2.2 (including the smallest region, since one reanalysis grid point covers $2.5° \times 2.5°$), but using daily anomalies of AIRS data. The three main vertical features mentioned above are very distinct. The free troposphere is well correlated with its vertical average. The regression slopes are less in agreement with the moist-adiabatic curve in Fig. 2.3a than in Fig. 2.2a. In particular, there is a noticeable positive bulge in the middle troposphere that we have noticed in other datasets as well. This may be related to regions and places that are not precipitating as much, since an analysis using precipitation masking with NCEP-NCAR reanalysis (not shown) revealed this feature to be much more pronounced during days with low precipitation. The largest AIRS region in Fig. 2.3a appears less moist adiabatic than the second-largest (warmer ocean) region, probably because the largest region includes the less-convecting eastern Pacific (see section 2.4.3). The cold top regressions and significant negative correlation coefficients in Fig. 2.3 are

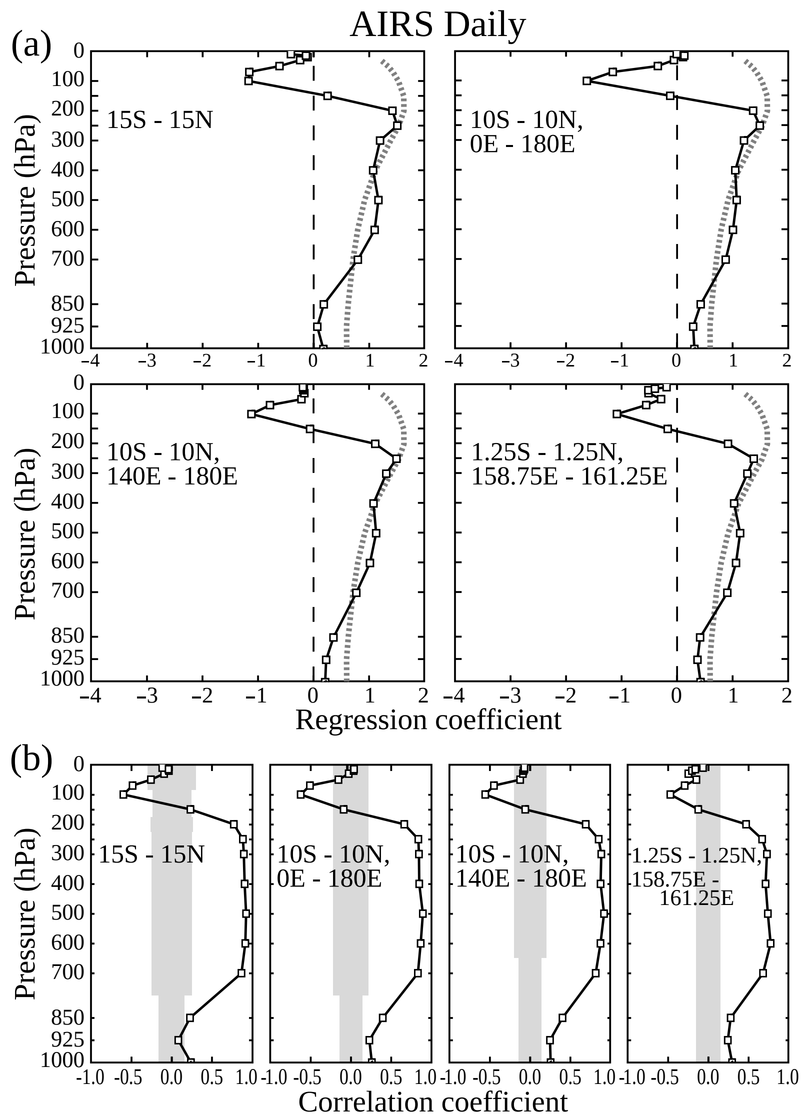

Figure 2.3: AIRS daily anomalies over ocean for the same four tropical boxes as in Fig. 2.2. (a) Regression coefficients (squares) with moist-adiabatic curve (dashed gray line). (b) Correlation coefficients with gray shading between the critical values for 95% significance.

fairly consistent across regions, unlike in Fig. 2.2.

As expected, the boundary layer has lower correlation coefficients than the free troposphere. This is more pronounced than in Fig. 2.2, and does not have an obvious dependence on scale. This fact may be exaggerated by our use of only the best quality AIRS profiles, which exclude deep convection and therefore are weighted toward soundings with less precipitation and less QE constraint. The larger the region, the more significant this effect, since temperatures are not as uniform for a given day (despite the tendency of gravity waves to spread temperature uniformly).

Figures 2.4a,b show analysis of 47 years of CARDS radiosonde monthly anomalies from three west Pacific warm pool islands averaged together. Figures made from each of the islands individually (not shown) are very similar to the average and to each other. Slopes generally follow the moist-adiabatic curve, although they are noticeably lower in the boundary layer and higher in the lower free troposphere. Correlation coefficients are very high (almost 1) in the free troposphere, becoming noticeably lower below 800 hPa. Also, there is a statistically significant cold top above the troposphere. Note that the column-average temperature being regressed upon for the CARDS data and corresponding moist-adiabatic curve is a slightly smaller layer of the free troposphere (850–250 hPa) because of much smaller samples of good-quality data above 250 hPa (see section 2.2.3).

To compare CARDS data with AIRS data, we have averaged the two years of daily anomalies used to make Fig. 2.3 into monthly anomalies over a region similar to, though somewhat larger than, that containing the three CARDS islands. We used this larger size region to ensure that every day had high-quality AIRS

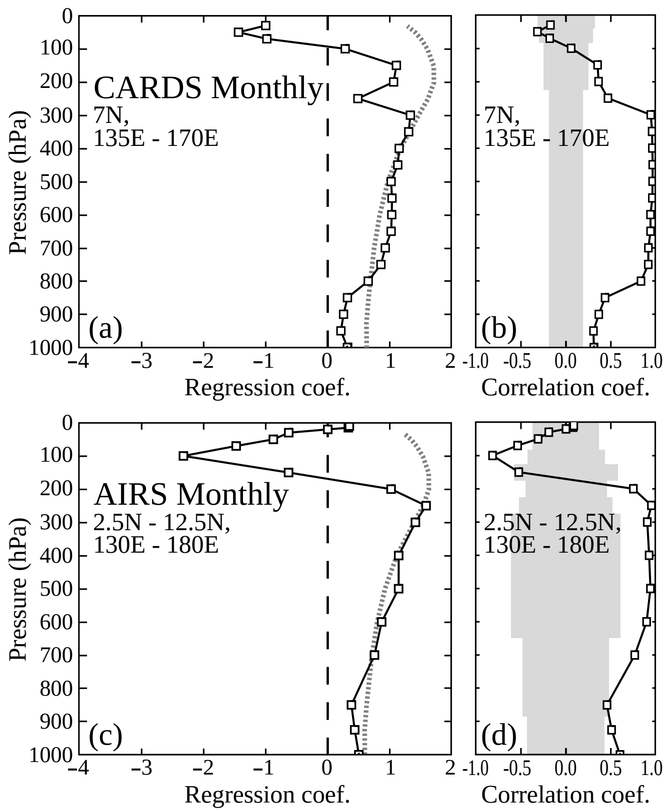

Figure 2.4: CARDS 1953–99, monthly anomalies for an average over three radiosonde stations on tropical western Pacific islands, and AIRS monthly anomalies from two years of daily anomalies. (a), (c) Regression coefficients (squares) with moist-adiabatic curve (dashed gray line). (b), (d) Correlation coefficients with gray shading between the critical values for 95% significance. Note that y-axis labels for both datasets and vertical sampling for CARDS are slightly different from other data analysis figures.

profiles. The resulting regression coefficients in Fig. 2.4c are even closer to the moist-adiabatic curve than the CARDS data, though they are admittedly over ocean, not islands, and for a much smaller time period, which may result in sampling issues. The cold top regression and correlation coefficients for AIRS data (Figs. 2.4c,d) are much larger in amplitude than the corresponding CARDS values in Figs. 2.4a,b, possibly because of the relatively sparse CARDS data at high levels.

Figure 2.4 makes an interesting comparison with Fig. 2.5, which shows monthly anomalies of 25 years of NCEP-NCAR reanalysis over the same four regions as in Figs. 2.2–2.3. The bottom-left panel in Fig. 2.5a, and its associated correlation coefficients in Fig. 2.5b, are from a similar warm pool region and have the same main features as the observational analyses in Fig. 2.4. The slopes are generally closer to the moist-adiabatic curve for NCEP-NCAR, though not much closer than AIRS. Going from larger to smaller scales in Fig. 2.5, the boundary layer becomes more independent, and there is also a slightly less coherent lower free troposphere than upper free troposphere. The convective cold top is present for all regions, though not as large or significant as in Figs. 2.4c,d, and not significant at the 95% level at the largest scales in Fig. 2.5. The QBO is a very large signal in the tropical stratosphere on long time scales (Plumb and Bell 1982; Huesmann and Hitchman 2001), making it difficult to separate from a possible convective signal and also reducing statistical significance given the autocorrelations associated with the QBO.

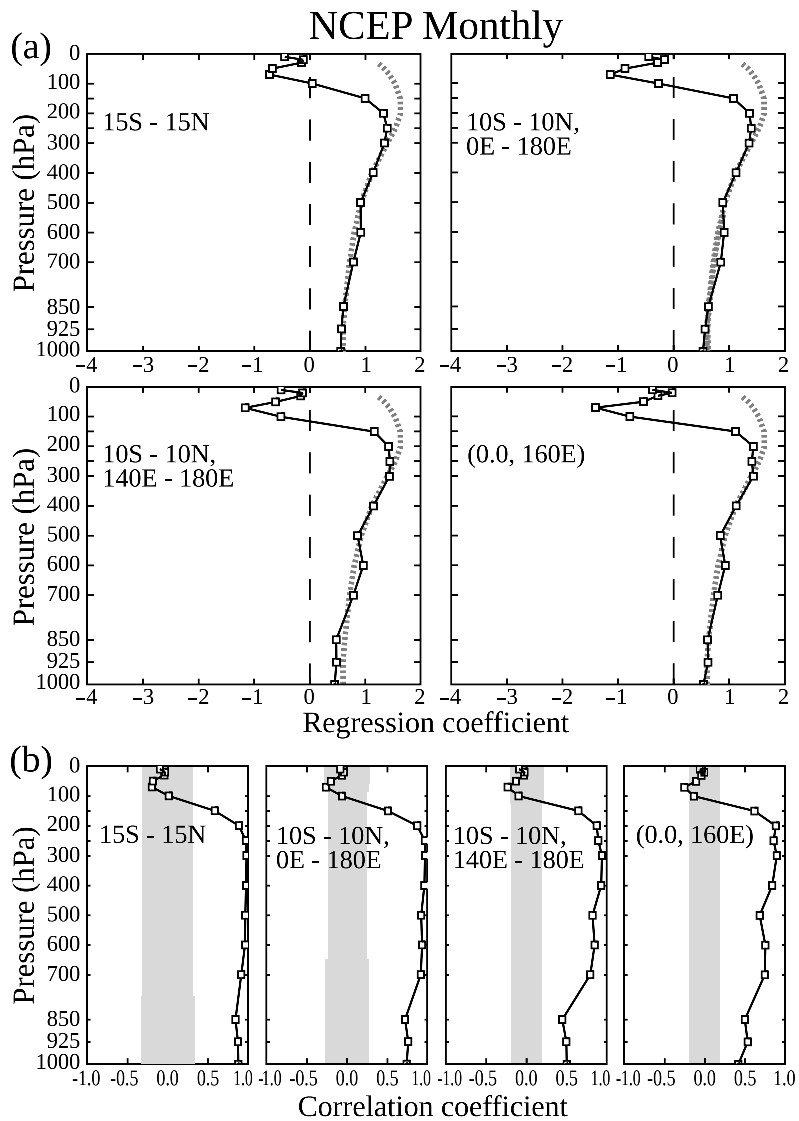

Figure 2.5: NCEP-NCAR 1979–2003 monthly anomalies for the same four tropical boxes as in Fig. 2.2. (a) Regression coefficients (squares) with moist-adiabatic curve (dashed gray line). (b) Correlation coefficients with gray shading between the critical values for 95% significance.

2.4.2 Comparison across time scales and sampling issues

Since it spans many different scales, we employ the NCEP-NCAR reanalysis for a direct comparison over different time scales at various regions. Comparing the monthly anomalies in Fig. 2.5 with the daily anomalies in Fig. 2.2, the most obvious difference is that the convective cold top is larger (in both regression and correlation coefficients) for the daily time scale, particularly at smaller spatial scales, although the AIRS data in Fig. 2.3 do not show this dependence. In the troposphere, as expected, correlation coefficients are generally higher at all vertical levels for monthly anomalies. This agrees with a recent analysis of the tropical vertical temperature structure of the 40-yr European Centre for Medium-Range Weather Forecasts (ECMWF) Re-Analysis (ERA-40) monthly anomalies, which shows large tropospheric vertical coherence mainly related to El Niño-Southern Oscillation (ENSO) variability, as well as an accompanying cold top feature centered from 50 to 70 hPa (Trenberth and Smith 2006). The regression coefficients line up extremely well with the moist-adiabatic curve, even at the boundary layer and at all scales (with a slight deviation at the Pacific warm pool), suggesting as expected that QE dominates temperature perturbations on longer time scales even more so than on daily time scales in the NCEP-NCAR reanalysis.

We now cautiously extend our time-scale comparisons to radiosonde datasets, at different locations in the Pacific warm pool region. Figure 2.6 shows analysis over this region for 4 months of daily average gridded CSU TOGA COARE merged profiler-rawinsonde data. This figure confirms a coherent free-troposphere feature resembling the moist-adiabatic curve even at daily time scales. Also

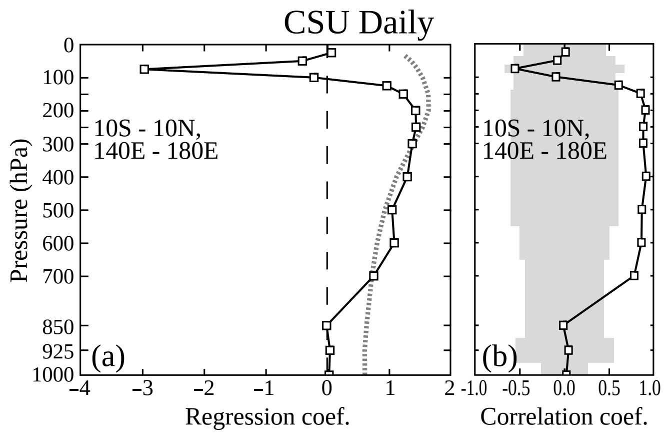

Figure 2.6: CSU TOGA COARE November 1992–February 1993 daily averages for the Pacific warm pool region. (a) Regression coefficients (squares) with moist-adiabatic curve (dashed gray line). (b) Correlation coefficients with gray shading between the critical values for 95% significance.

present are a pronounced cold top regression amplitude (significant at around the 75% level) and an independent boundary layer. Since the CARDS analysis in Figs. 2.4a,b, over three Pacific warm pool islands with a larger time scale and a longer time series, shows extremely high correlation coefficients throughout the free troposphere, fairly low but still statistically significant correlations and slopes in the boundary layer, and a moderately significant, smaller cold top slope above, we can conjecture that our main conclusions about time scales made above with respect to NCEP-NCAR also hold for radiosonde data. Note that the AIRS data in Fig. 2.3 also show many of the attributes mentioned above for daily time scales. Monthly AIRS anomalies analyzed over the same regions (not shown) as those in Fig. 2.3, however, do not differ appreciably from the daily analyses; a longer time series would help resolve this.

To interpret Fig. 2.6, a relatively short daily time series with the seasonal cycle still included, we made comparisons of some similar time series using NCEP-

NCAR reanalysis (not shown). Removing the seasonal cycle improves significance of correlation coefficients, and results in slightly more tropospheric agreement with the moist-adiabatic curve. The particular 4-month period can make a significant difference in the locations of kinks in the curve, and to boundary layer independence, which sometimes approaches the degree seen in Fig. 2.6 even in the reanalysis.

2.4.3 A nonconvecting region

As an example of a nonconvecting region, we consider the eastern Pacific, from the equator to 15°S, where there is climatological annual mean subsidence at 500 hPa (as measured from the NCEP-NCAR data). For monthly NCEP-NCAR data, Figs. 2.7a,b show regression coefficients close to the moist-adiabatic curve in the free troposphere, similar to Fig. 2.5. One difference is that boundary layer regressions are larger, possibly because long time-scale SST changes in this region are of larger amplitude than, but fairly well correlated to, nonlocal tropical convective warming affecting the free troposphere. The cold top feature, as in Fig. 2.5a, is small and not statistically significant.

At daily scales, Figs. 2.7c,d show an analysis of the AIRS and NCEP-NCAR data over the same region. There is clearly less agreement with the moist-adiabatic curve in Fig. 2.7c, especially for the AIRS data. We interpret the conformance to the moist-adiabatic curve in monthly, but not in daily, data as being due to the horizontal adjustment process by wave dynamics. We suspect that deviations from the moist-adiabatic curve in previous figures, specifically positive deviations in the middle free troposphere and negative ones in the upper

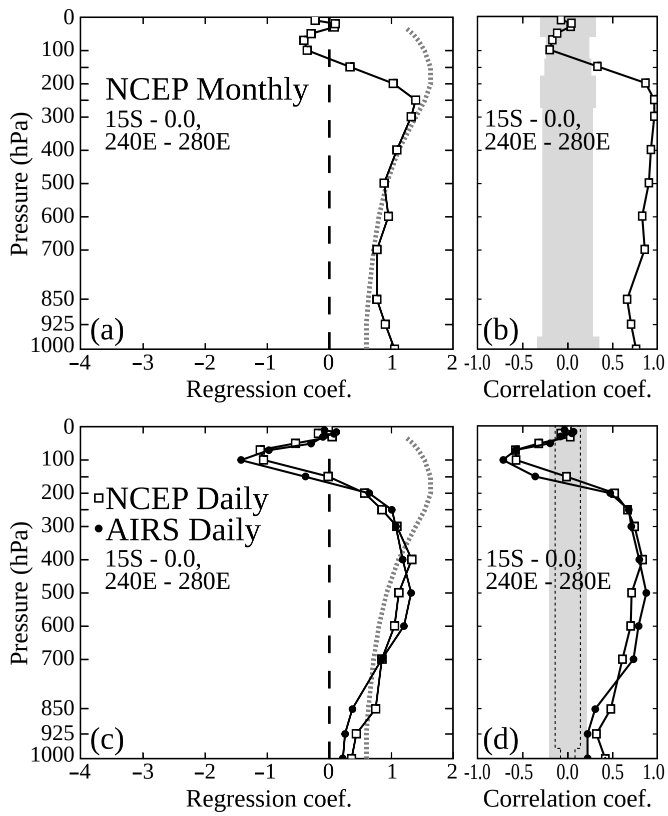

Figure 2.7: An eastern Pacific, largely nonconvecting region. (a) Regression coefficients for NCEP-NCAR monthly anomalies (squares) with moist-adiabatic curve (dashed gray line). (b) Correlation coefficients for NCEP-NCAR monthly anomalies with gray shading between the critical values for 95% significance. (c) Regression coefficients for NCEP-NCAR daily anomalies (open squares) and AIRS daily anomalies (filled circles) with moist-adiabatic curve (dashed gray line). (d) Correlation coefficients for NCEP-NCAR daily anomalies (open squares) and AIRS daily anomalies (filled circles). Critical values for 95% significance are shown by gray shading (NCEP-NCAR) or dashed lines (AIRS).

free troposphere, are related to nonconvecting times and places contributing to those averages. There is also less coherence in the free troposphere in Fig. 2.7d, and the boundary layer correlations are especially low. The cold top feature remains robust at daily scales, suggesting that the shape of the tropospheric warming, and its source (in this case, likely wave dynamics spreading temperature perturbation signals from neighboring tropical regions) is not crucially important in determining the convective cold top.

2.5 The convective cold top

Figures 2.2–2.7 all exhibit a robust negative slope and correlation between the upper-tropospheric-lower-stratospheric temperature and the free-tropospheric average temperature. In nearly all cases, at all scales, this correlation is statistically significant at the 95% level or higher, except for NCEP-NCAR at monthly scales over the largest tropical spatial scales, and for a 4-month raw time series of daily radiosonde data. Given the prevalence with which we find this phenomenon in our results, it is not surprising that an extensive search through the literature has uncovered many descriptions of this type of behavior in various forms, which we believe are all connected to a single underlying mechanism. We include here a brief review of some relevant articles as well as evidence of the convective cold top in a linear Boussinesq 2D model of a uniformly stratified fluid with prescribed heating and a semi-infinite domain. We then present a simple explanation that the cooling results from hydrostatic horizontal pressure gradients that extend above the top of the convective heating, causing divergence and broad adiabatic ascent.

2.5.1 Relevant studies

Early studies of tropical cyclones noted a pool of cold air above the warm central core and hypothesized that this was due to the overshooting of cumulus towers (Arakawa 1950; Koteswaram 1967). Jordan (1960) presented radiosonde observations over islands in the Pacific warm pool and suggested that very cold tropopause temperatures might be related to increased periods of deep convection. Johnson and Kriete (1982) noted observations of cold anomalies at the top of mesoscale anvils in the Indonesian region during the International Winter Monsoon Experiment (Winter MONEX) and discussed several possible reasons for this. One hypothetical cause was cloud-top radiative cooling, and evidence supporting this idea included observations by Webster and Stephens (1980), who found significant radiative cooling at the cloud top, which they defined as approximately 200 hPa. However, as Johnson and Kriete (1982) pointed out, the observed radiative cooling occurs in the upper layers of the clouds themselves, which according to aircraft radar data were no higher than 100 hPa, whereas the maximum cooling occurred about 1–2 km above these anvil tops. They also raised the possibility that ice injected into the lower stratosphere might create radiative cooling there, as well as the theory (by then mentioned in several places) that overshooting updrafts in convective towers could be responsible. More recent observations of cold anomalies above short time-scale equatorial waves include those by Haertel and Kiladis (2004), while Reid and Gage (1996) found negative temperature correlations with the free troposphere at high levels over Truk in the western Pacific using eight years of radiosondes.

Similar observations of mesoscale cold pools above midlatitude summertime convective complexes prompted Fritsch and Brown (1982) to perform numerical experiments using a primitive equation model with 20-km horizontal resolution. They found that a mesoscale cold pool was formed aloft in two almost identical experiments, one in which the detrainment of directly overshooting parcels was parameterized at the cloud top, and the other with this direct cooling omitted. In fact, in the latter case the broad adiabatic ascent that led to all of the cooling in that experiment was stronger than in the case where diabatic cooling was parameterized. Pandya and Durran (1996) used a fully compressible, nonhydrostatic, dry model to show that adiabatic lifting due to gravity waves above and behind squall lines can cause large negative temperature perturbations without overshooting turrets. Reid et al. (1989) and Reid (1994) correlated temperatures from radiosonde stations at various levels with the ENSO index, proposing vertical ascent and adiabatic cooling as an important possible mechanism for negative correlations at high levels. Reid (1994) also argued that, assuming a "capping level" above which ENSO deep convection signals are no longer projected onto geopotential gradients, there must be cooling above tropospheric heating. This argument, applied to more varied scales, is similar to our overall explanation for why the convective cold top is so prevalent. The idea that adiabatic ascent might vary depending on the amount of concurrent diabatic cooling will also be discussed in more detail below.

Highwood and Hoskins (1998) presented several mechanisms by which deep convection might influence the cold point tropopause. They showed that a Gill-type model (Gill 1980) with prescribed heating generates large-scale adiabatic cooling at high levels associated with equatorial Kelvin and Rossby waves. They also discussed downward control via the stratospheric pump (i.e., midlatitude cyclones generate breaking waves in the stratosphere, causing divergence and adiabatic cooling over the Tropics and leading to enhanced deep convection), and the possible contribution of overshooting turrets (e.g., as observed on small scales by Danielsen 1993). Teitelbaum et al. (2000) also discussed these possible mechanisms for stratospheric cooling related to convection.

On long time scales, some authors have proposed that deep convection could be related to the QBO in the stratosphere via several mechanisms, including dynamical cooling of the tropopause layer by the east phase of the QBO, although observations show that that phase does not always accompany cooling (e.g., Collimore et al. 2003). Kuang and Bretherton (2004) argued that cooling at the cold point tropopause (and hence the drying of air entering the stratosphere) is strongly tied to convection, mainly through turbulent mixing (overshooting parcels), contradicting several other studies advocating a more gradual process largely related to radiative effects (e.g., Holton and Gettelman 2001; Thuburn and Craig 2002). Kuang and Bretherton (2004) used a cloud-resolving model (CRM) with continuously active convection, but they could not address the question as to whether turbulence or broad adiabatic ascent is more important, since convectively driven adiabatic ascent would also be correlated with increases in tracer injection by overshooting parcels (their model cannot produce mean horizontal adiabatic temperature change at any vertical level because it has periodic lateral boundaries and a rigid lid). Sherwood et al. (2003) noted a cooled tropopause feature above convection in regional radiosonde data and inferred from a simple numerical model that this was likely caused by a combination of adiabatic ascent and diabatic turbulent mixing, and Robinson and Sherwood (2006) showed similar results using a CRM.

2.5.2 Convective cold top in a linearized Boussinesq model

To simulate the underlying process we believe is responsible for the ubiquity of the convective cold top, we use a simple linearized model of a uniformly stratified hydrostatic Boussinesq atmosphere initially at rest, which is forced by constant sinusoidal heating and has a semi-infinite domain (as opposed to a rigid lid). The equations and parameters are discussed in detail in Nicholls et al. (1991), while a correction to the computational evaluation of the semi-infinite solutions, as well as a simpler equivalent solution for vertical velocity constructed by superimposing a series of pulse buoyancy sources at single levels, are presented by Pandya et al. (1993) [their Eq. (6)].

The basic linearized 2D equations (neglecting rotation) are

$$\frac{\partial u}{\partial t} + \frac{1}{\rho_0}\frac{\partial p'}{\partial x} = 0, \tag{2.1}$$

$$\frac{1}{\rho_0}\frac{\partial p'}{\partial z} = b, \tag{2.2}$$

$$\frac{\partial b}{\partial t} + wN^2 = Q, \tag{2.3}$$

$$\frac{\partial u}{\partial x} + \frac{\partial w}{\partial z} = 0, \tag{2.4}$$

where u, w, p', b, and N are the horizontal velocity, vertical velocity, perturbation pressure, buoyancy, and buoyancy frequency per mass unit, respectively, and Q is the thermal forcing (Nicholls et al. 1991). Following Pandya et al. (1993) and Nicholls et al. (1991), $\rho_0 = 1$ kg m^{-3}, $N = 0.01$ s^{-1}, and Q is constant in time, a heating rate that is sinusoidal in vertical height (only one positive heating mode, maximum at 5 km and going to zero at the surface and at 10 km) with a half-width in the horizontal at $x = 10$ km and a magnitude $Q_{m0} = 2.0$ J kg^{-1}. Vertical velocity (w) is calculated analytically at each time step using Eq. (6) from Pandya et al. (1993). Buoyancy (b) is determined by numerically integrating Eq. (2.3) in time. To compare with our previous analysis, perturbation temperature $T' = b/(\alpha g)$, where α is a linear thermal expansion coefficient such that $\rho' = -\alpha\rho_0 T'$ and g is the gravitational constant. In an isothermal basic-state approximation, $\alpha = 1/T_0$.

Figures 2.8a,b show the progression in time over 2 h of w and b at $x = 0$. At early times, w quickly increases in a deep layer. Then, above the heating, w rapidly diminishes back toward zero, and the steady state is reached with a warm troposphere and the cold top above. Figure 2.8c shows profiles of b after 2 h of simulation for the center of the heating, $x = 0$ (solid black line), and for a remote location with virtually no heating, $x = 100$ km (gray dashed line). The two b profiles after 2 h are nearly the same below the top of the heating, exhibiting the well-known behavior of gravity waves reducing horizontal gradients. The convective cold top is visible in both cases, although at $x = 0$ the cold top is sharper and the maximum cooling occurs at exactly $z = 10$ km, the lowest height, and thus the level with maximum w integrated in time, that has zero diabatic heating. The lower peak magnitude and more vertically spread cold top at $x = 100$ km is due to the effects of vertically propagating gravity waves that are now farther from their source. Note that the higher (in altitude) level of the cold top minimum temperature away from the heating looks more like the observations in Figs. 2.2–2.7. At 2 h of time, b and w can be seen over many values of x in Fig. 1 of Pandya et al. (1993), including a convective cold top feature. A similar simulation (not shown) including both the half sine wave and an equal magnitude full sine wave, with heating in the upper half and cooling in the lower half of the troposphere (as in Nicholls et al. 1991), did not qualitatively change the cold top feature.

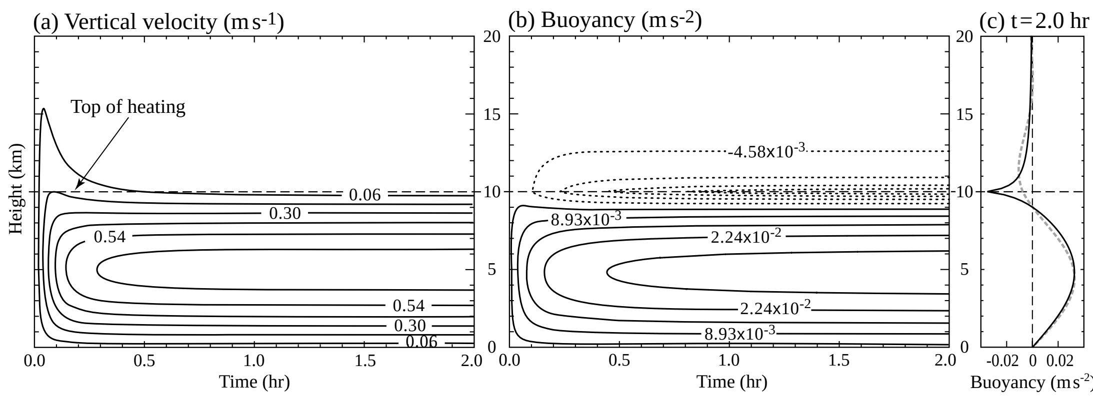

Figure 2.8: Linear Boussinesq model: (a) w in m s^{-1} at $x = 0$; (b) b in m s^{-2} at $x = 0$, dotted contours are negative; (c) b profile at $t = 2$ h for $x = 0$ (solid black line) and $x = 100$ km (dashed gray line). The buoyancy (b) is proportional to T'.

In Figs. 2.9a–c, a profile of w is plotted at three different times at $x = 0$ (solid black line), and the constant Q/N^2 value is shown in gray, with $Q = 0$ above 10 km. Figures 2.9d–f show b at the same 3 times in solid black, along with p' in gray. Pressure is found by vertically integrating b using the hydrostatic Eq. (2.2), with the constant of integration set by the constraint that $\int p'dz = 0$ (which holds if flow vanishes at some x). We approximate this condition by extending the integration to 500 km and enforcing zero vertical mean, verifying that p' approaches zero at the top.

Hydrostatic pressure perturbations created by positive b in the troposphere must be compensated by p' above to satisfy $\int p'dz = 0$. At 0.04 h (Fig. 2.9d)

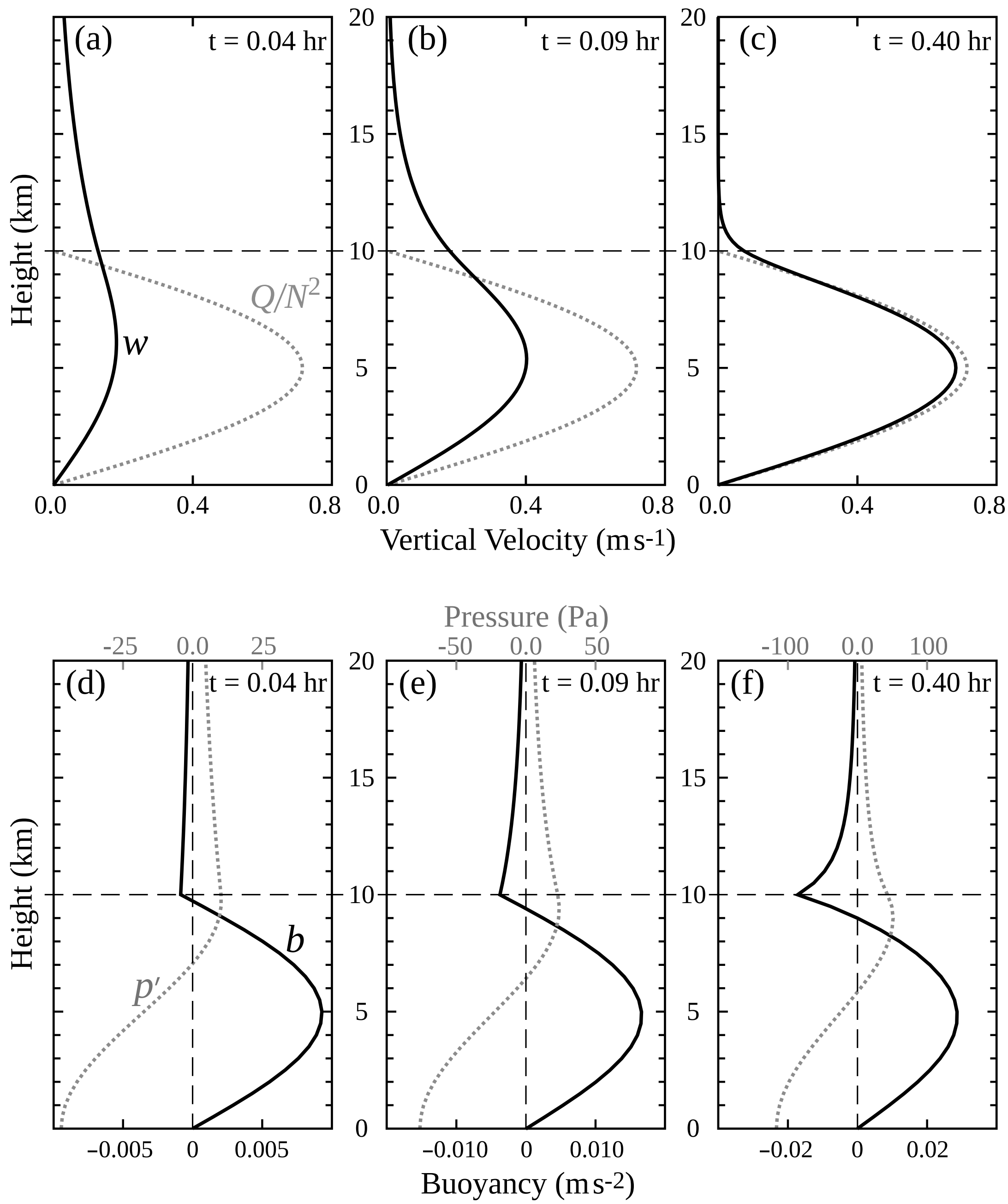

Figure 2.9: Linear Boussinesq model at $x = 0$: (a)–(c) w in m s^{-1} (solid black line) and Q/N^2 (dashed gray line, same units) at three times; (d)–(f) b in m s^{-2} (solid black line) and p' in Pa (dashed gray line). Note that x axes for b and p' double in scale from (d) to (e), and again from (e) to (f).

the troposphere has warmed significantly, but only small-amplitude negative b has developed aloft at any given level. The p' above the heating thus decays very slowly with height, accelerating a very deep horizontal divergence. This produces positive w decaying only slowly above the heating (Fig. 2.9a). There is resulting adiabatic cooling where w is larger than Q/N^2 and warming where w is smaller, via Eq. (2.3). As negative b develops above the heating, where $Q = 0$ and $\partial b/\partial t = -wN^2$, the magnitude of p' (and thus the magnitudes of b and w) can decay more rapidly with height (Figs. 2.9b,c and 9e,f). This leads to a cold top increasingly concentrated around $z = 10$ km (Figs. 2.9e,f), where there is maximum w above the heating function. At 0.40 h w is approaching Q/N^2 (Fig. 2.9c). By 2 h, w is virtually equal to Q/N^2 at all levels, and b reaches a steady state as shown in Fig. 2.8c. The convective cold top in this model thus arises entirely through adiabatic cooling near the top of and above the heating region.

The convective cold top as seen in Figs. 2.8–2.9 should not be thought of as parcels overshooting their levels of neutral buoyancy due to momentum conservation, since this is a hydrostatic model. Instead, horizontal pressure gradients extend above the top of the heating, creating divergence and broad ascent to satisfy continuity. Positive vertical velocity above the heating causes adiabatic cooling, which then reverses the sign of the left-hand side of Eq. (2.2), allowing pressure gradients to become very small aloft. The cold top takes longer to develop farther from the heating, but after a short time the resulting b profiles look relatively similar.

2.5.3 A simple convective cold top explanation

The above model experiment demonstrates the basic mechanism that we believe to be the fundamental cause of the convective cold top. In order for baroclinic pressure gradients generated by convective heating to become small at high altitudes, there must be cooling above the heating. In this simple hydrostatic model, the only mechanism available for this cooling is adiabatic, caused by horizontal divergence and broad vertical velocity reaching above the top of the heating. In the real atmosphere, diabatic cooling due to overshooting cumulus turrets or cloud-top radiation could contribute to part of the necessary cooling, but this would only result in smaller horizontal pressure gradients, less divergence, and less additional adiabatic cooling required to yield the same end result. Note that in the model, the response above the heating spreads to remote regions as fast as the tropospheric warming, a result not expected from local diabatic cooling alone.

To demonstrate quantitatively how temperature perturbations above convective heating relate to free-tropospheric temperature perturbations in the data, we use the hydrostatic equation in pressure coordinates:

$$\Phi'(p) \approx R_d \int_p^{p_s} T'(p) d \ln p + \Phi'_s, \tag{2.5}$$

where Φ' is the perturbation geopotential, R_d is the gas constant for dry air, p is the pressure, p_s is the surface pressure, T' is the perturbation temperature, and Φ'_s is the surface geopotential perturbation. This result, applied to the temperature regression slopes shown earlier in Figs. 2.2–2.6, gives the geopotential perturbation profile associated with 1° of free-tropospheric vertically averaged warming. Because there is a barotropic as well as a baroclinic component to Φ'_s, we then subtract the vertical mean of this profile, $\hat{\Phi}'$, since [Φ' - $\hat{\Phi}'$] is independent of Φ'_s, with $\hat{\Phi}'$ defined as follows:

$$\hat{\Phi}' = (\frac{1}{p_s - p_t}) \int_{p_t}^{p_s} \Phi'(p) dp, \tag{2.6}$$

where p_t is the pressure at the top of the available atmospheric data. This represents baroclinic geopotential perturbations if the barotropic mode is separated from the baroclinic mode (e.g., surface drag effects and vertical shear effects are minimal). To the extent that these two modes are instead interacting, the actual Φ' will be shifted by a vertical constant from the results shown here.

Figure 2.10 shows six plots of [Φ' - $\hat{\Phi}'$], indicating that at most scales the convective cold top brings down the baroclinic pressure gradients significantly relative to their peak values. The $d \ln p$ differential in Eq. (2.5) implies that temperature anomalies at upper levels are especially effective at contributing to net geopotential gradients near the top of the atmosphere. We have included regression coefficients at all available pressure levels, including those that are not statistically significant at the 95% level, since we have no other values to use. The "zero wind" level occurs uniformly near 400 hPa. Figure 2.10a suggests that at large scales cold top effects are not as strong, but this smaller cold top may be due to the QBO signal. In contrast, Fig. 2.10c shows a stronger-than-expected cold top for monthly AIRS data in the western Pacific. Figure 2.10b over a similar region for monthly CARDS data shows an expected cold top magnitude, along with daily analyses in the Pacific warm pool region for three different datasets (Figs. 2.10d–f).

To summarize, combining the analysis above with interpretation from the

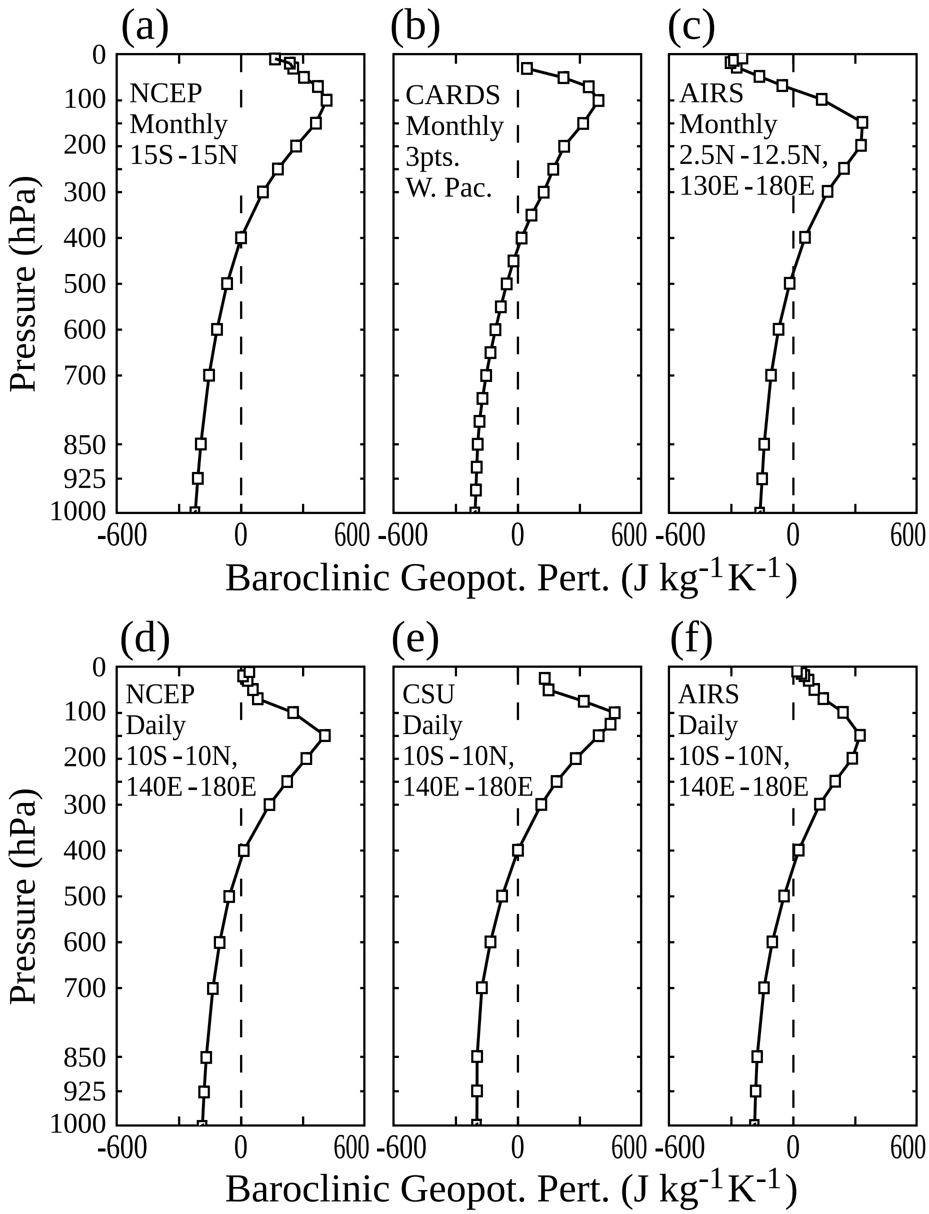

Figure 2.10: Baroclinic geopotential perturbations per vertical average temperature perturbation with the vertical average removed, $[\Phi' - \hat{\Phi}']$, calculated using the hydrostatic Eq. (2.5). (a) NCEP-NCAR reanalysis 1979–2003 monthly anomalies. (b) CARDS 1953–99 monthly anomalies. (c) AIRS monthly November 2003–05 anomalies. (d) NCEP-NCAR November 2003–05 daily averages with three harmonics of the seasonal cycle removed. (e) CSU TOGA COARE November 1992–February 1993 daily averages. (f) AIRS daily November 2003–05 anomalies. Horizontal boxes are labeled.

simple model: a cold top layer is necessary above a warmed troposphere to reduce pressure gradients above the heating. Unless diabatic cooling of sufficient magnitude happens to occur, the circulation due to pressure gradients will tend to yield adiabatic cooling, producing the needed cold top.

2.6 Summary and discussion

The majority of analyses over various datasets, time scales, and space scales show that temperature perturbation regressions at different pressure levels can be divided into three main features: the boundary layer, a highly coherent free troposphere, and the convective cold top above, with a minimum negative correlation near or above the tropopause. These three primary features are evident even when temperatures at individual levels are regressed on temperatures averaged over the entire column, or on temperatures at individual levels within the free troposphere (not shown), instead of on a free-tropospheric average. Figure 2.11 is a schematic illustrating these vertical features, using the CARDS analysis from Fig. 2.4. A brief discussion of each feature and some of its implications follows below.

2.6.1 Coherent free troposphere

The free troposphere, from about 800 to 200 hPa, is the layer with the highest correlation coefficients when the temperature at each level is regressed on the free-tropospheric vertical average temperature. These free-tropospheric temperature perturbations are similar to those derived from an ensemble of moist adiabats with surface conditions typical of warm tropical oceans. Some deviations from

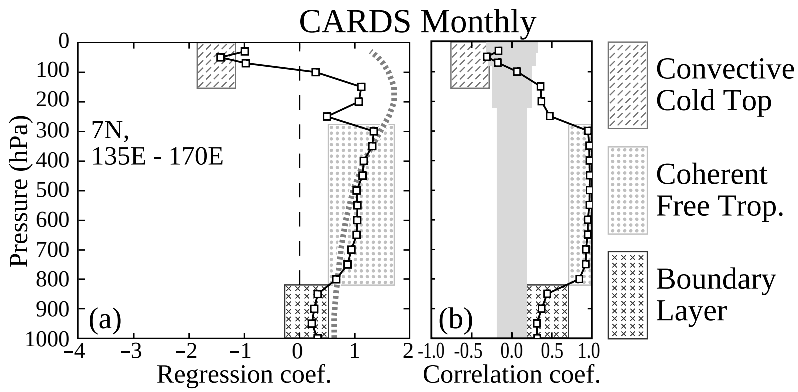

Figure 2.11: Schematic of the three main features of the vertical temperature structure, illustrated for the CARDS monthly anomalies (regression and correlation coefficients) from Fig. 2.4.

the moist-adiabatic curve, especially for AIRS satellite data, may be due to places and times that are not strongly convecting (such as the region shown in Fig. 2.7), or to freezing-melting processes, although this remains a topic for future research. The coherence of the free troposphere tends to decrease at smaller scales, but more so for NCEP-NCAR reanalysis than for other observational data.

Overall, the highly coherent free troposphere is consistent with expectations from theory: namely, QE establishes a coherent vertical mean temperature structure in convective zones and then gravity waves quickly spread this signal over large scales. These results are much more consistent with QE expectations than other approaches that have analyzed relationships between the free troposphere and the boundary layer. This high coherence can be utilized to predict baroclinic pressure gradients and winds using simplified vertical temperature structures.

2.6.2 Independent boundary layer

Below the free troposphere is a largely independent boundary layer, from about 1000 to 850 hPa. For typical tropical ocean conditions this reaches above the LCL, which is between 925 and 900 hPa. The boundary layer generally has a correlation with the free troposphere on the order of 0.5 or less even at monthly time scales and large space scales, and smaller for smaller scales, with regression coefficients usually below those of the moist-adiabatic ensemble. The boundary layer temperature in NCEP-NCAR tends to covary highly with the free troposphere to a greater extent than in AIRS and radiosonde data. This suggests that convective parameterizations may misrepresent the troposphere-boundary layer temperature relationship, even while correctly capturing the temperature perturbation profile in the free troposphere. Preliminary analyses of global climate model (GCM) output and ERA-40 reanalysis (not shown) give results similar to NCEP-NCAR.

One important reason for a distinctive boundary layer is that we are only regressing temperature on temperature, rather than a measure of boundary layer moist static energy such as θ_e, since we are primarily interested in the vertical coherence of temperature signals and corresponding pressure gradients. It is possible that boundary layer θ_e might track that of the free troposphere if changes in boundary layer relative humidity compensate for variations in boundary layer temperature. However, based on studies such as Brown and Bretherton (1997), which did use θ_e in the boundary layer, and a few similar tests we did using NCEP-NCAR and CARDS data, it is not that simple. Another likely explanation is that the free troposphere is more homogeneous, constantly modified by fast-moving gravity waves from various sources of deep convection, especially over the warmest ocean surfaces. The boundary layer should have more influence from local surface fluxes. The relationship to convective heating is complicated at smaller scales by subsaturated downdrafts, which reduce boundary layer θ_e (Cheng 1989). Finally, when convection is locally suppressed, for instance by a lack of conditional instability or by dry air infusions above the boundary layer, QE no longer applies and there is little reason for temperature to behave coherently through the whole troposphere. Likely, all of these effects and possibly others are working simultaneously, and the boundary layer will be a topic of future work.

2.6.3 Convective cold top

A nearly universal finding is a statistically significant negative correlation coefficient (between temperature and free-tropospheric average temperature) somewhere from about 100 to 50 hPa depending on the dataset. We refer to this phenomenon as the “convective cold top.” We find it at many different scales. It is unlikely that the negative correlations seen here on long time scales are related to climate change (i.e., greenhouse gas warming in the troposphere correlating with greenhouse gas cooling in the stratosphere) because we find little trend in free-tropospheric temperatures over the years analyzed for NCEP-NCAR reanalysis and the relatively few years with available stratospheric temperatures for CARDS.

Using a linearized Boussinesq model with constant heating, we illustrate a simple explanation for this feature. We show that as gravity waves spread the warming due to convective heating through the free troposphere, hydrostatic pressure gradients will extend above the heating, causing divergence, ascent, and adiabatic cooling aloft. This extension of outflow above the top of the heating has important implications for calculations of gross moist stability, which have been shown to be sensitive to the top level of integration (Yu et al. 1998).

In the real atmosphere, cooling by some means is necessary above areas of heating in order for hydrostatic pressure gradients to become small at high altitudes. Therefore, any diabatic cooling associated with convective heating should only reduce the amount of adiabatic cooling required by our proposed mechanism. If these horizontal pressure gradients did not go to zero above convective heating, they would cause anomalous divergence and adiabatic cooling, which would then reduce them. The convective cold top should be thought of as an intrinsic response to convective heating, and as an inherent part of quasi-equilibrium temperature adjustment.

2.7 Appendix: Sensitivity of Moist Adiabats

To demonstrate that moist-adiabatic regression coefficients show little variability over typical tropical precipitating conditions, we present an analysis of the original NCEP-NCAR daily data (with no harmonics removed, and no spatial or temporal averaging) used in Fig. 2.2. We use temperatures and specific humidities between 15°S and 15°N, at 1000 hPa, for grid points with more than 2 mm day-1 of precipitation. To facilitate analysis, 10% of these data (73 015 points) have been randomly selected. We produce (with the same code described in section 2.3) an array of reversible moist adiabats starting from each point. Figure 2.12 shows the temperatures at each level plotted against the 850–200-hPa column-average temperatures for each calculated sounding. Pressure has been labeled for each data curve on alternate sides. Diamonds along the horizontal axis mark the location of the distribution octiles (eighth quantiles, defining the boundaries between the eighths). Vertical average temperature correlates almost perfectly with 1000-hPa θ_e (not shown), though the relationship is weakly nonlinear. The 1000-hPa θ_e equals 348.5, 354.4, and 360.1 K at the first octile, median, and seventh octile, respectively. The lines in Fig. 2.12 are very linear above 925 hPa, especially within the center three quarters of the data, signifying little sensitivity of the slopes of moist-adiabatic temperature perturbations at these levels to 850–200-hPa column-average moist-adiabat temperature (and thus to 1000 hPa θ_e) for typical tropical values. The curvature increases slightly above 300 hPa as the transition to nearly dry adiabats occurs sooner for profiles with smaller vertical average temperature values.

Figure 2.13 shows the regression values in black from the data shown in Fig. 2.12 for three ranges: the first to second octiles, the third to fifth octiles, and the sixth to seventh octiles. The curves are nearly identical between 925 and 300 hPa. Above 300 hPa, curves with lower 1000-hPa θ_e values begin curving back toward a linearly decreasing slope (characteristic of dry adiabats) faster, since they have less water vapor left at a given level. To generate the curve shown in Figs. 2.2–2.7, we used a 1000-hPa temperature range (298–301 K) and constant relative humidity (83%) close to the mean values of the analyzed NCEP-NCAR data between the third and fifth octiles (299.8 K and 83.2%, respectively). This curve is shown as a dashed gray line, as in previous figures, and lies between the left and middle curves above 300 hPa. Note that even an analysis using 1000-

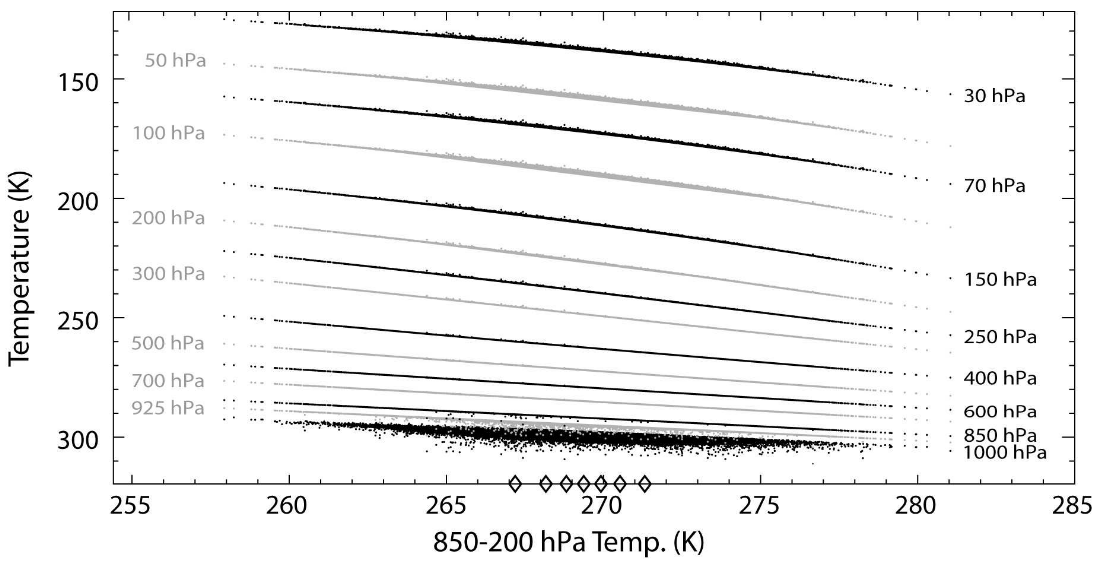

Figure 2.12: Temperature of reversible moist adiabats calculated from 1000-hPa NCEP-NCAR daily temperature and humidity data, November 2003–05, for grid points between 15°S and 15°N, masked for precipitation greater than 2 mm day^{-1}. Note that the vertical axis is temperature increasing downward. The horizontal axis is the 850–200-hPa column-average temperature of each moist-adiabat profile. Pressure levels are labeled alternately at right and left for each data curve. The position of the distribution octiles (eighth quantiles) of column-average temperature are represented with diamonds on the horizontal axis.

hPa ranges that are far from typical tropical precipitating values (292–295 and 304–307 K with 75% and 90% relative humidity, respectively) shows a maximum difference in regression coefficients with the curve shown in Figs. 2.2–2.7 of only 0.09 between 1000 and 300 hPa.

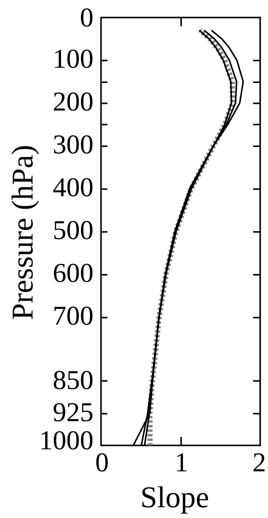

Figure 2.13: Regression coefficients (black lines) of reversible moist adiabats in Fig. 2.12, for data lying between the first and second octiles, third and fifth octiles, and sixth and seventh octiles, respectively (curves appear in this order at upper levels). The gray dashed line is the curve used in Figs. 2.2–2.7, with the same aspect ratio as in those figures.

2.8 Appendix: Additional considerations

2.8.1 Vertical structure in GCMs

Like the NCEP-NCAR reanalysis, GCM output appears to be more constrained to the theoretical moist-adiabatic profile than satellite and radiosonde data. Figure 2.14a shows regression profiles for 25 years of monthly anomalies for the 20th century runs of three GCMs from IPCC AR4 archive data. These profiles are rather similar to each other and to the NCEP-NCAR monthly anomaly curves in

Fig. 2.5. In particular, the agreement with the moist-adiabatic curve reaches all the way down through the boundary layer: this agrees with findings in Wu et al. (2006).

These profiles for temperature perturbations on interseasonal time scales have implications for vertical structures of longer-term climate predictions. Fig. 2.14b shows mean temperature difference profiles for end of 21st century global warming runs minus end of 20th-century runs. Although these curves have not been normalized by their average warming, their shapes in the troposphere, including small kinks in the mid-troposphere, are very similar to the shorter-term perturbations shapes from Fig. 2.14a. This suggests that the shape of warming on interseasonal scales, probably largely constrained by convective parameterizations, will in turn affect the profile of temperature change predicted for global warming in each model. In the upper troposphere, the longer-term warming reaches somewhat higher up than the interseasonal warming profile, but the relationships between models appear to be similar in both cases. The amount of warming in the upper troposphere relative to that in the lower troposphere will have an important effect on the stability of the tropical atmosphere and thus on the amount of weakening of tropical circulations such as the Hadley circulation. Note that the stratospheric cooling in Fig. 2.14b is mainly due to radiative effects of ozone depletion and carbon dioxide emissions, although there may be some contribution from the convective cold top effect.

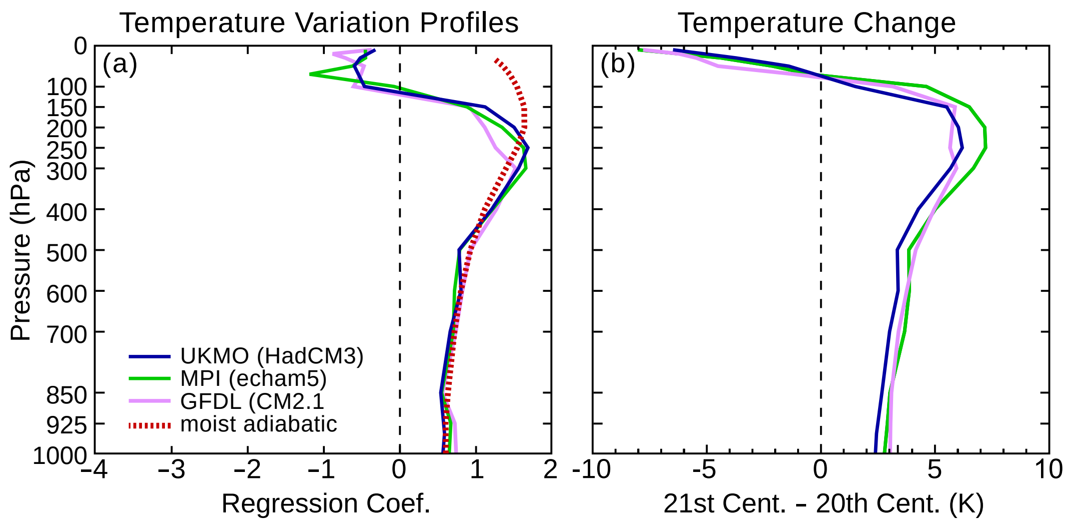

Figure 2.14: Monthly anomalies 1970–1994 for Pacific warm pool region for three GCMs from IPCC 4AR data. (a) Regression coefficients with moist-adiabatic curve (dashed red line). (b) Difference of mean temperature profiles between the end of 21st century (2070–2094) and the end of 20th century (1970–1994) for same three GCMs.

2.8.2 Application of coldtop to QTCM

One application of the convective cold top is the ability for an intermediate complexity model, such as the QTCM, to reduce pressure gradients and winds to zero near the top without imposing any arbitrary, unphysical constraints. For the simplest version of QTCM, which has one temperature perturbation structure, we added negative perturbations above the heating so that the curve matched the shape of the NCEP-NCAR daily Pacific warm pool regression coefficients above 400 hPa, smoothed with a spline fit. We then multiplied this negative portion of the curve by a factor necessary so that the baroclinic geopotential perturbation would be zero at the top. This modified temperature perturbation structure, along with extra vertical levels above the tropopause, was incorporated in an axisymmetric version of QTCM by Bellon and Sobel (2008) as a way to avoid setting baroclinic winds equal to a constant at high levels.

2.8.3 Spatial patterns of vertical structure

To get an idea of spatial patterns of this relationship, we present a map of rms differences between the regression coefficients and the moist-adiabatic curve for the NCEP-NCAR monthly anomalies (Fig. 2.15). These are taken for the free-tropospheric layer 700–300 hPa, which is low enough to be below the tropopause even in midlatitudes. The dark blue end of the spectrum represents grid points that are very close to the moist-adiabatic curve. This color extends over almost all of the tropics and a large part of the subtropics, showing that the relationships shown above for a specific west Pacific grid point does not depend on the exact location chosen.

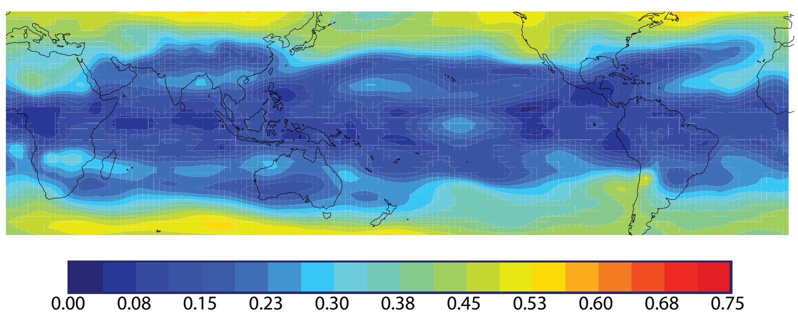

Figure 2.15: Vertically averaged 700–300 hPa rms differences between regression coefficients and moist-adiabatic curve, for individual grid points of NCEP-NCAR monthly anomalies.

Although we have shown that the NCEP-NCAR reanalysis, especially on monthly time scales, shows much more agreement with the moist-adiabatic curve than observations from satellites and radiosondes, it provides us with a well sampled horizontal data set. We use this data so to investigate some of the ways that the boundary layer temperature perturbations can be independent from the free-trospospheric perturbations. In regular observations, we expect that these mechanisms would be more pronounced.

Figure 2.16 shows the difference between regressions at each grid point and the moist-adiabatic curve at 300 hPa, along with correlations at that level. As expected, the points that were close to the moist-adiabatic curve in Fig. 2.15 are also very close to the curve at 300 hPa (light green color).these regions also have very high correlations with the free troposphere, although there are surprisingly high correlations at many midlatitude regions as well.

At 1000 hPa, there is a very different pattern. Figure 2.17a shows that the central and eastern Pacific cold tongue shows much larger regression coefficients in the boundary layer than would be expected from a moist-adiabatic relationship with the free troposphere. Surrounding this, to the west and poleward, there are some areas with lower than expected regression coefficients, many of which are not statistically significant (white shading). Correlation coefficients in Fig. 2.17b follow this general pattern as well, although the high correlations just off the equator in the eastern and central Pacific give way to lower correlations in the Southeast equatorial Pacific cold tongue.

The patterns in Figure 2.17 strongly suggest ENSO effects as an explanation for more independent boundary layer behavior. Since El Niño events generally warm the free troposphere, it is not surprising that regions typically showing enhanced convection and SST during El Niño, such as the ITCZs in the central and eastern Pacific, would correlate well with the free troposphere. Further, the cold tongue boundary layer will tend to be colder at normal or La Niña conditions, meaning it will be colder than the moist-adiabatic temperature corresponding to the average free-tropospheric temperatures during those times, which should be fairly coherent across the tropics. This kind of mechanism has been mentioned in many ENSO studies (e.g., Chiang and Sobel 2002) as they affect the remote tropics.

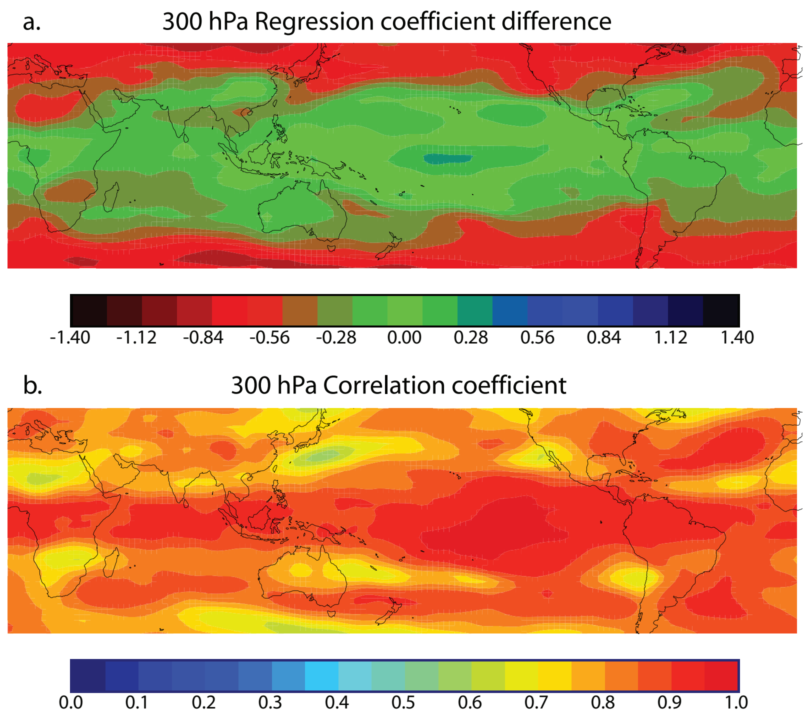

Figure 2.16: 300 hPa individual grid points of NCEP-NCAR monthly anomalies: (a) differences between regression coefficients and moist-adiabatic curve. (b) correlation coefficients.

2.8.4 Reinterpretation of quasi-equilibrium

Figure 2.18 shows a schematic of the adjustments to quasi-equilibrium thinking discussed in this section, including the differing boundary layer effects (middle) due to the non-uniform distribution of SST and deep convection related to ENSO and the local influence of surface fluxes on the boundary layer. The schematic also

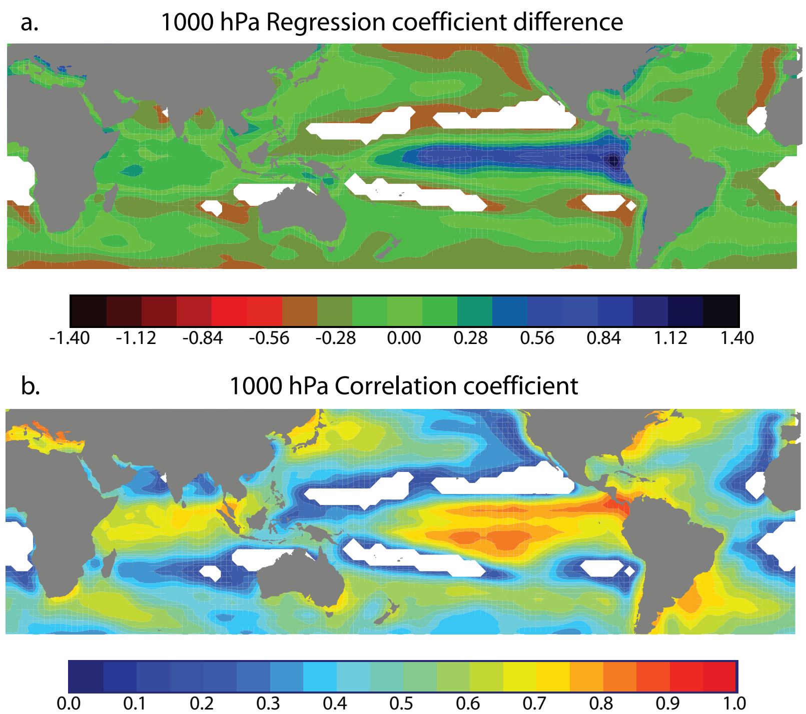

Figure 2.17: 1000 hPa individual grid points of NCEP-NCAR monthly anomalies: (a) differences between regression coefficients and moist-adiabatic curve. (b) correlation coefficients. White spaces show points with values that are less than 95% statistically significant.

includes the effects of the convective cold top (bottom), which can be considered as another adjustment process associated with quasi-equilibrium.

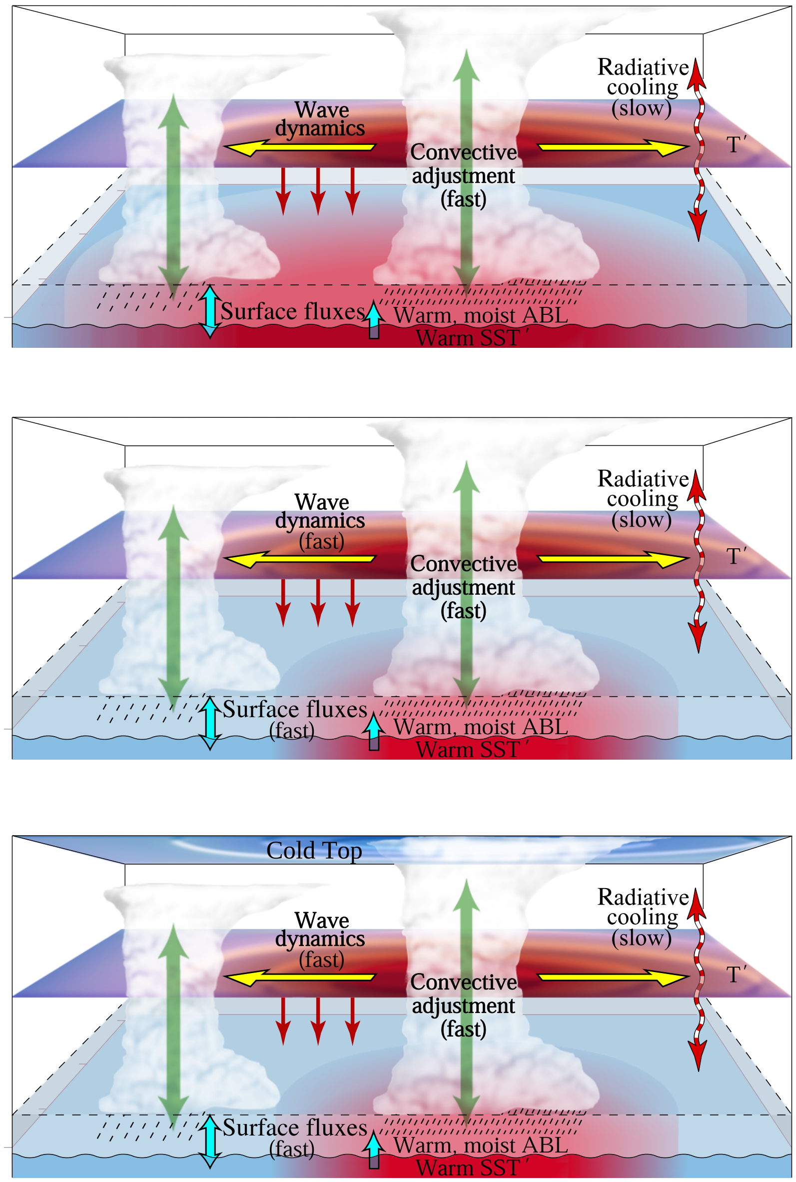

Figure 2.18: Schematic showing adjustments to simple quasi-equilibrium ideas, including boundary layer effects of different SSTs (middle) and the convective cold top (bottom).

Chapter 3

Moisture Vertical Structure and Tropical Deep Convection

Abstract

The vertical structure of the relationship between water vapor and precipitation is analyzed in five years of radiosonde and precipitation gauge data from the Nauru Atmospheric Radiation Measurement (ARM) site. The first vertical principal component of specific humidity is very highly correlated with column water vapor (CWV) and has a maximum of both total and fractional variance captured in the lower free troposphere (around 800 hPa). Moisture profiles conditionally averaged on precipitation show a strong association between rainfall and moisture variability in the free troposphere, and little boundary layer variability. A sharp pick-up in precipitation occurs near a critical value of CWV, confirming satellite-based studies. A lag-lead analysis suggests it is unlikely that the increase in water vapor is just a result of the falling precipitation. To investigate mechanisms for the CWV/precipitation relationship, entraining plume buoyancy is examined in sonde data and simplified cases. Higher CWV results

in progressively greater plume buoyancies for several mixing schemes, notably upper-tropospheric buoyancy that can yield deep convection. All other things equal, higher values of lower-tropospheric humidity, via entrainment, play a major role in this buoyancy increase. A small but significant increase in subcloud layer moisture (and thus equivalent potential temperature) with increasing CWV also contributes to buoyancy. Entrainment based on mass flux increase through a deep lower-tropospheric layer yields a relatively even weighting for the impact on mid-tropospheric buoyancy of all lower levels, explaining the association of CWV and buoyancy available for deep convection.

3.1 Introduction

A number of studies indicate that moist convection is sensitive to free-tropospheric water vapor, including observational analyses (Austin 1948; Malkus 1954; Brown and Zhang 1997; Sherwood 1999; Parsons et al. 2000; Bretherton et al. 2004) and studies using cloud-system resolving models (Tompkins 2001b; Grabowski 2003; Derbyshire et al. 2004). This dependence is apparently not well represented in global climate models (GCMs) (Derbyshire et al. 2004; Biasutti et al. 2006; Dai 2006)—but sensitivity has been shown in some cases (Richter and Neale 2008, manuscript submitted to *J. Climate*, Zhang and Wang 2006). Recent work also suggests that the inability of most GCMs to simulate multi-scale convective organization, including intraseasonal variability associated with the Madden-Julian Oscillation (MJO), may be due primarily to this lack of a positive feedback between free-tropospheric moisture and convection (Grabowski 2006).

Since precipitation processes in climate models are very sensitive to the method of convective parameterization (Slingo et al. 1996), it is of interest to investigate the relationship between tropospheric moisture and precipitation in observations and its representation in convective parameterizations. Regions where the trade winds flow into convection zones tend to exhibit sensitivity to changes associated with teleconnections and global warming, and they are also sites of disagreement in simulated precipitation among different models (Neelin et al. 2003; Neelin et al. 2006). Inflow of drier tropospheric air is typical in these locations. The interaction between inflow across moisture gradients and the difficulty of convective parameterizations in simulating the sensitivity of convection to free-tropospheric moisture could play a role in the model discrepancies in these regions (Lintner and Neelin 2007).

A few recent studies have illustrated an empirical relationship between tropical column water vapor, CWV (scaled by some measure of free-tropospheric temperature, which does not change very much in the deep tropics) and precipitation, including a sharp pick-up of average precipitation at sufficiently high CWV (Bretherton et al. 2004; Peters and Neelin 2006). In the present study, we investigate the vertical structures of water vapor variability at Nauru Island in the western equatorial Pacific. One goal is to better understand the vertical distribution of the moisture variance associated with CWV, a metric easily available from satellite data. Another motivation is to investigate the main vertical structures of water vapor perturbations, providing insight for intermediate-complexity models which represent water vapor with one or a few vertical structures, such as the quasi-equilibrium tropical circulation model (QTCM; Neelin 1997; Neelin and Zeng 2000).

After characterizing the vertical structure of water vapor and its relationship to average precipitation and CWV in section 3.3, we turn to the effects of different environmental profiles of moisture on simple plume models of convection in section 3.4. Analysis in terms of an entraining plume (e.g., Raymond and Blyth 1992; Brown and Zhang 1997; Jensen and Del Genio 2006) is used to connect the increased buoyancy of entraining plumes in moist environments with the sharp pick-up of average precipitation at high CWV. We also investigate the role of sub-cloud layer moistening versus free-tropospheric moistening on entraining plume buoyancy. The sensitivity of the results to assumptions of mixing profiles and microphysics in section 3.5 provide insight into the challenges of incorporating environmental humidity in convective parameterizations.

3.2 Data

The Department of Energy's Atmospheric Radiation Measurement (ARM) Program (Stokes and Schwartz 1994) maintains a climate observation site at Nauru Island (0.5°S, 166.9°E; Mather et al. 1998). We have analyzed radiosonde temperature and moisture data and optical gauge surface precipitation from 1 April 2001 to 16 August 2006. The radiosonde data have been interpolated onto 5 hPa levels. The uncertainty of the Vaisala (RS80, RS90, and RS92) radiosondes is approximately 0.5°C for temperature and 5% for relative humidity, although in the upper troposphere (above 500 hPa) relative humidity uncertainties can be much larger (Westwater et al. 2003). The main observations occur twice a day, at 00z and 12z, with occasional sondes around 14z and 02z.

The precipitation rate is measured at 1-min intervals by an optical gauge with

0.1 mm hr^{-1} resolution and 0.1 mm hr^{-1} uncertainty. For comparison with the radiosondes, a 1-hr average rain rate has been computed, centered at the launch time of each radiosonde. Since the sonde takes about 45 minutes to rise through the troposphere, this averaging window should give a good characterization of the precipitation conditions in the airmass through which the sonde rises. Time averaging also helps reduce the precipitation measurement noise inherent in the use of a single gauge; averaging over many hourly events, as is done in the analyses of this study, further reduces this noise.

The sonde pressure, temperature, and humidity data have had a basic quality check at ARM, and have been further constrained to be within reasonable ranges; the lowest-altitude sonde data have also been checked for agreement with ARM surface data. In total, 3,491 sondes have been retained for the complete analysis (with 200 additional sondes containing acceptable data at some levels included in the water vapor variability analyses). The radiosonde versions analyzed in this study are not thought to have much dry bias, which characterized earlier Vaisala sonde versions (B. M. Lesht 2007, personal communication). The sonde total CWV values compare fairly well with 1-hr averages of microwave radiometer values, with a correlation coefficient of 0.92. A slight tendency for the sondes to be moister than the radiometer at high CWV likely occurs because the radiometer cannot operate during rainfall and may have difficulties when cloud water is large.

3.3 Characterizing the vertical structure of moisture

An important step in investigating the vertical structure of the transition to deep convection is characterizing the vertical structure of moisture variations as a whole. This endeavor is more complicated than the analogous problem for tropical temperature perturbation structures, which tend to follow reversible moist adiabats and are smoothed in the horizontal by gravity waves, at least in the free troposphere on large enough space and time scales (e.g., Xu and Emanuel 1989; Holloway and Neelin 2007). Water vapor has smaller spatial uniformity than temperature in the tropics, and is more locally influenced by evaporation, precipitation, and advection. Here we investigate the vertical variability of water vapor at Nauru and relate this to CWV, which in turn is related to precipitation.

3.3.1 Effect of precipitation on moisture structure

Profiles of specific humidity q conditionally averaged on precipitation (Fig. 3.1) reveal that it is mainly free-tropospheric moisture, rather than boundary layer moisture, which increases with increasing rainfall. The spread among the curves is larger than the maximum confidence interval, indicating that the separation of the mean specific humidity at many tropospheric levels by average precipitation is real. Note that the bins double in width with increasing precipitation and that most of the sondes fall into the first bin (see caption for bin counts), which is basically non-precipitating, so that q profile in that bin is actually fairly representative of the mean profile overall. In the highest precipitation bin, there is actually a decrease in the subcloud layer moisture compared to the other bins, probably due to subsaturated downdrafts forming cold pools (see section 3.3.5).

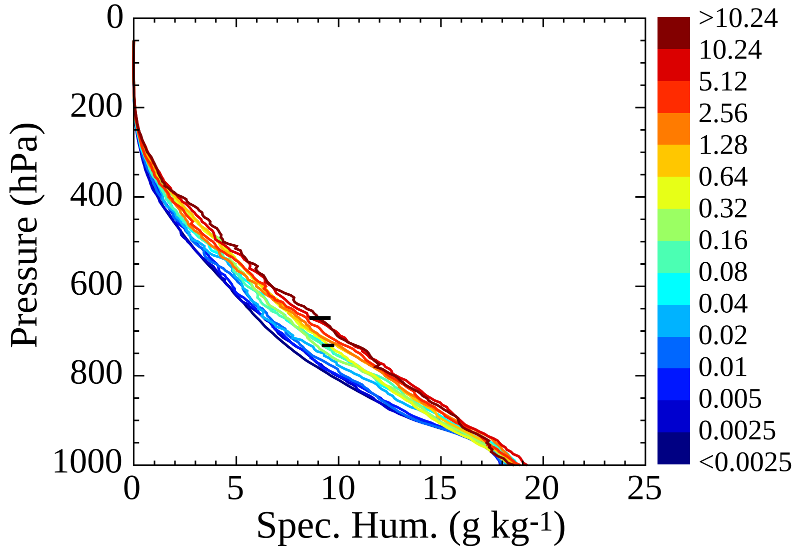

Figure 3.1: Specific humidity (g kg^{-1}) profiles conditionally averaged on 1-hr average precipitation rate in mm hr^{-1} (color bar). Bin counts from lowest to highest precipitation range are: 2805, 93, 90, 59, 32, 40, 36, 49, 47, 43, 44, 30, 21, and 11. Horizontal bars indicate the maximum, as well as a representative, ± 1 standard error (standard deviation divided by the square root of the sample number) range.

Figure 3.1 can be compared to analyses of monthly and daily averages of specific humidity profiles from radiosondes conditionally averaged on precipitation in Bretherton et al. (2004, their figures 9 and 10a). While their monthly means from many long-term tropical radiosonde stations do not show much difference between spread at free-tropospheric levels and spread in the boundary layer, their two months of daily Tropical Rainfall Measurement Mission (TRMM) Kwajalein Experiment (KWAJEX) sondes do show variability similar to that in these 5 years of ARM twice-daily data, although their values are a little lower. Concurrent work by Nuijens et al. (2008, manuscript in preparation) for trade cumulus conditions near Barbuda finds a similar relationship between lower-free-tropospheric humidity and precipitation.

3.3.2 Leading vertical structure and relation to column water vapor

Two recent studies have investigated a statistical link between CWV and precipitation using satellite data. Bretherton et al. (2004) show that, on daily and monthly scales, precipitation increases roughly exponentially with CWV. Peters and Neelin (2006) find that precipitation, conditionally averaged by CWV over many individual events, tends to increase slowly up to some critical value and then rapidly increase above that. This kind of relationship can be detected in these ARM data as well, as discussed below in section 3.3.3. An important question, however, concerns how the variance of CWV is distributed over different vertical levels.

Figure 3.2a shows the results of principal component analyses (using the covariance method) performed on each level of q from 1000–200 hPa for all available sondes and for a much smaller "high precipitation" subset of sondes that occur within ± 3 hours of 1-hr precipitation values greater than 2.56 mm hr^{-1} (red and blue lines, respectively). The solid lines show the variance explained by the first principal component (PC 1) for the two analyses, while the long-dashed lines show the total variance of q at each level. These principal components represent 53% and 49% of the total variance for all sondes and the high precipitation sondes, respectively. In both analyses, the second principal component represents a much smaller fraction of the variance, and is not well separated from the other higher principal components. The dotted red line shows total variance at each level of a hypothetical specific humidity field derived only from temperature and a fixed relative humidity profile (taken from the mean of all original sondes). This shows that observed changes in temperature alone, assuming constant relative humidity, could account for only a small amount of the total moisture variances. This is generally expected in the tropics for these short time scales, and appears to be particularly true at this western Pacific location.

The solid curve can be divided by the dashed curve in each case to get the fractional variance represented by PC 1 at each level, shown in Fig. 3.2b. The square roots of these profiles (the correlation coefficients between PC 1 and q at each level, not shown) line up fairly well with correlations between CWV and water vapor mixing ratio found for an average over soundings from many research vessel cruises in the tropics (Yoneyama 2003, their figure 5a).

The most striking feature of these figures is the large peak in the lower troposphere for both total variance and fractional variance represented by PC 1. It makes sense that variance decreases upwards in the upper troposphere, since increasingly colder temperatures limit the amount of water vapor that the air can hold, and therefore the variance of water vapor as well. Smaller total variance at boundary layer levels is in agreement with many previous studies suggesting that boundary layer q is tied fairly closely to SST, whereas free-tropospheric q can vary greatly due to processes such as dry air intrusions and advection from convective regions (e.g., Liu et al. 1991; Yoneyama 2003). However, the small fractional variances in the boundary layer shown in Fig. 3.2b reveal that the maximum shared variance (PC 1 in each case) is dominated by the lower troposphere even more than would be predicted based on a fixed fraction of the total variance.

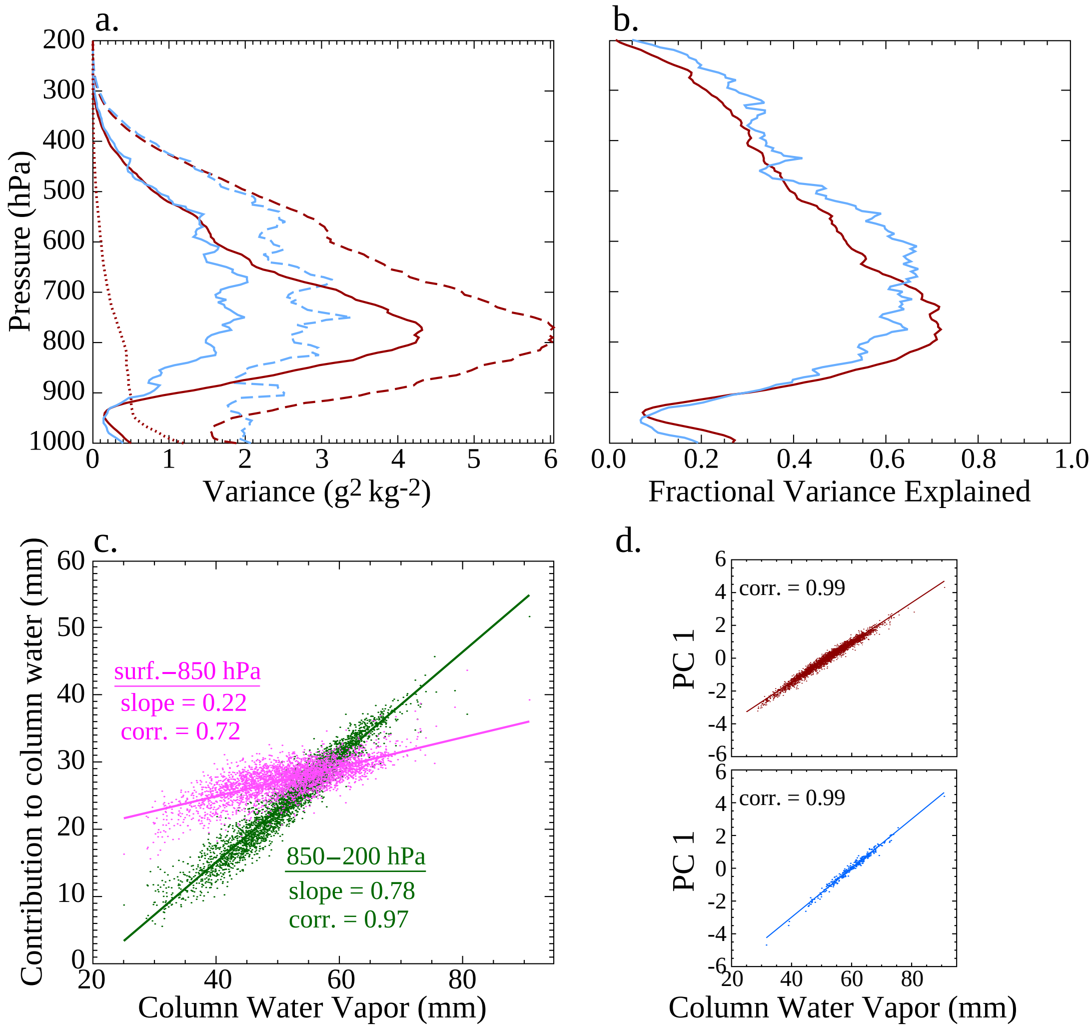

Figure 3.2: (a) Variance of specific humidity (g^2 kg^{-2}) for all sondes (red) and for sondes within ±3 hours of the highest precipitation averages (blue). Long-dashed lines show total variance, solid lines show variance explained by PC 1 at each level. The dotted red line shows total variance at each level of a hypothetical specific humidity field derived only from temperature and a fixed relative humidity profile (taken from the mean of all original sonde relative humidity). (b) Fractional variance explained by PC 1. (c) Scatter plots and linear regressions of the integrated contribution to column water (mm) from the surface to 850 hPa (magenta) and from 850–200 hPa (green) versus the column water vapor. (d) Regressions and correlations of PC 1 versus column water vapor for all sondes (top) and for sondes within ±3 hours of the highest 1-hr precipitation (bottom).

Figure 3.2c shows the contributions to the CWV variance from the vertically-integrated boundary layer (surface–850 hPa) and free-tropospheric (850–200 hPa) water vapor. Even though the boundary layer contains a mean vertically-integrated contribution to column water of 27.5 mm, slightly higher than the corresponding value of 24.5 mm in the free troposphere, it is clear from the correlations and regressions (which add to one, since these two layers add up to give CWV) that a large majority of the total column variance is explained by the free-tropospheric layer.

Figure 3.2d confirms that, for each of these cases, the first principal component shown in Figure 3.2a,b is almost perfectly correlated with CWV, in agreement with Liu et al. (1991). Therefore, the solid curves in Fig. 3.2a represent the variance at each level explained by CWV, which as a whole represents approximately 50% of the total variance in each case as shown in the figure. Applying the above findings for PC 1, this means that free-tropospheric levels contribute the great majority of the total CWV variance, to an even greater extent than would be expected by simply taking a fixed fraction of the total variance at each level, and despite the slightly larger mean vertically-integrated moisture contained below 850 hPa. Not only do free-tropospheric levels have larger q variances than boundary layer levels, they also vary together to a much greater extent than they share variance with boundary layer levels (as shown by the high PC 1 loadings in the lower free troposphere). This implies that, to a very good approximation, CWV could be represented by a free-tropospheric vertically-integrated q added to a mean boundary layer value (or even better, a boundary layer value that is a linear function of the free-tropospheric value).

3.3.3 Free-tropospheric versus boundary layer vertically-integrated water vapor: relationship to moisture structure and precipitation

To illustrate the vertical profiles of moisture associated with different amounts of column water, and specifically with the transition to high precipitation, we conditionally average sonde profiles on water vapor integrated over three different vertical layers. Figure 3.3a shows specific humidity profiles conditionally averaged on total CWV (the bins are equal-width except for the two outer bins, as shown on the color bar). Although there is some spread in the boundary layer, the largest spread occurs around 800 hPa, consistent with Fig. 3.2a.

For CWV bins below about 50 mm, the subcloud layer (below 950 hPa) is more vertically constant and more sharply distinguished from the troposphere, as expected for stable subsidence conditions. Much of the tropospheric variability in these bins is also consistent with subsidence altering air that had once been closer to saturation, with a typical maximum in the middle of the troposphere, causing the stretching at middle levels. Figure 3.3a also fits well with previous descriptions of dry intrusions in the free troposphere, which can suppress deep convection for over a week while shallow convection slowly moistens the lower troposphere (Numaguti et al. 1995; Mapes and Zuidema 1996; Brown and Zhang 1997; DeMott and Rutledge 1998; Parsons et al. 2000).

Much of the variability occurs at the lower end of the CWV range, as discussed above; this is not seen for the humidity profiles conditionally averaged on precipitation shown in Fig. 3.1. This is expected because the lowest precipitation bin in that figure contains the vast majority of sondes, which probably include

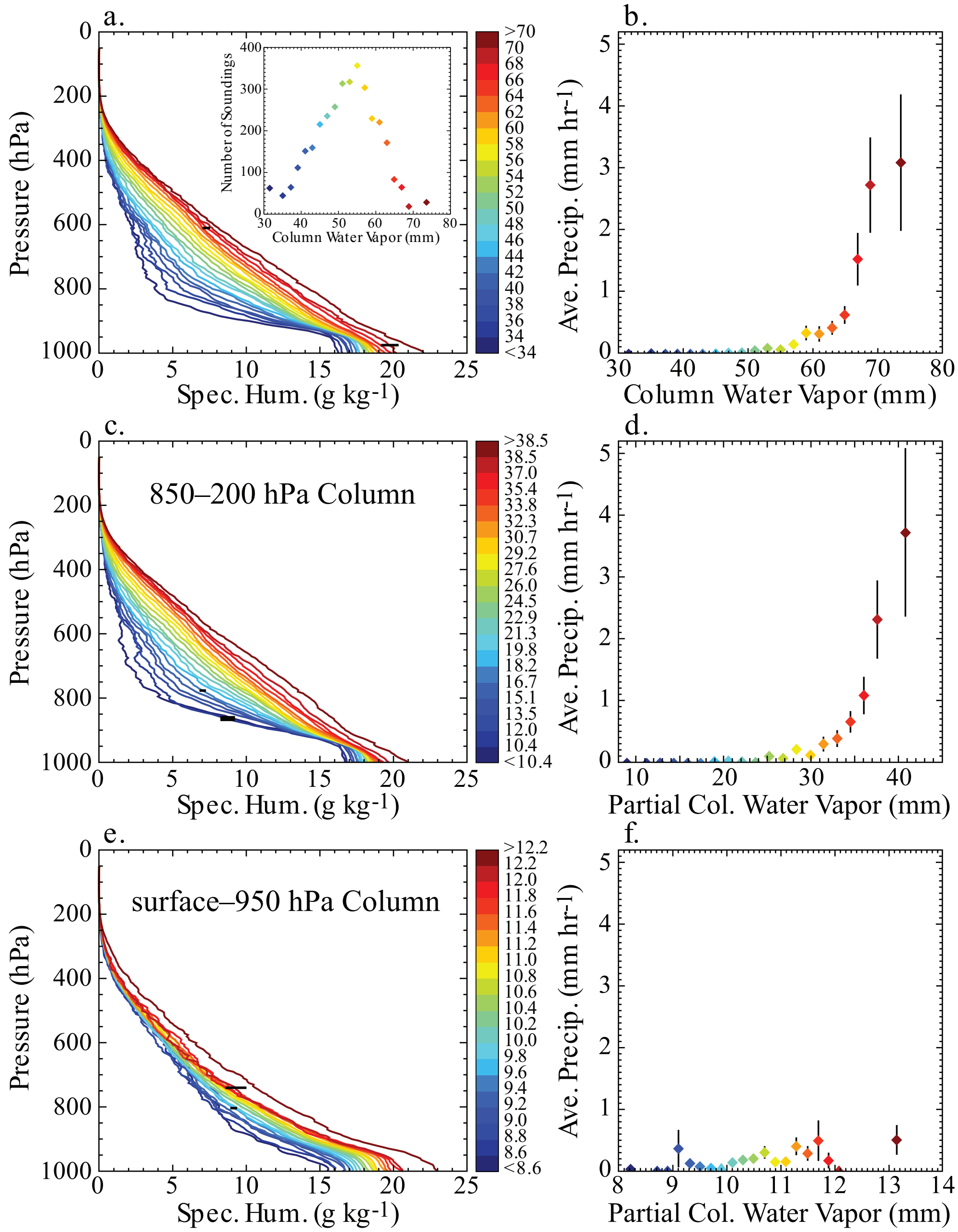

Figure 3.3: Specific humidity (g kg^{-1}) profiles and 1-hr average precipitation rates, respectively, conditionally averaged on: (a), (b) total column water vapor in mm (color bar); (c), (d) column water integrated from 850–200 hPa (color bar); and (e), (f) column water integrated from the surface to 950 hPa (color bar). Vertical bars on precipitation values represent ± 1 standard error. Horizontal bars indicate limits of the maximum, as well as a representative, standard error range. Inset for panel (a) shows number of sondes for total column water vapor bins plotted against each bin's average value.

mostly sondes with middle and drier CWV values, as well as some higher values. This association of near-zero precipitation with the lower half of CWV bins is confirmed by Fig. 3.3b, which shows precipitation conditionally averaged on the same CWV bins as in Fig. 3.3a. There is clearly a sharp pick-up of precipitation above about 67 mm CWV. This jump is significant, as indicated by the vertical bars representing ± 1 standard error. The general increase in precipitation agrees with daily mean values in Bretherton et al. (2004), although their curves stop below 65 mm CWV. The sharp pick-up of precipitation roughly agrees with Peters and Neelin (2006) in both CWV value and shape, although the small number of sondes in the bins with highest CWV (illustrated by the inset in Fig. 3.3a) makes it impossible to confirm whether the curve follows a power law function as observed in that study.

When the specific humidity profiles and precipitation are conditioned on just the free-tropospheric column water (850-200 hPa, with bin edges chosen to correspond as much as possible to those for the total CWV), the results are similar to those found with the total CWV. This is expected, since section 3.3.2 showed that lower-free-tropospheric q variance dominates CWV variance. Indeed, Fig. 3.3c shows even less variance in the boundary layer, which of course follows from the use of a free-tropospheric layer for the conditional averaging. The precipitation averages in Fig. 3.3d actually seem to have an even smoother pick-up of similar shape to that in Fig. 3.3b.

Figures 3.3e,f confirm that the subcloud layer (up to 950 hPa) is much less related to CWV. Little of the free-tropospheric variability illustrated for CWV in Fig. 3.3a is captured in Fig. 3.3e. The precipitation averages in Fig. 3.3f perhaps suggest a slight, noisy increase in precipitation with subcloud layer moisture, but the values are much smaller. This relationship has implications for intermediate-complexity models such as the QTCM. A single vertical degree of freedom in moisture indeed captures much of the effect on precipitation, but its variance is primarily in the free troposphere. Modeling can thus benefit from two degrees of freedom in the vertical (c.f. Neggers et al. 2007; Sobel and Neelin 2006) to allow the free troposphere to be separated from the boundary layer, which tends to be closely tied to surface conditions.

3.3.4 Relative Humidity Structure

A question which naturally follows from Figures 3.1–3.3 is the extent to which the higher values of specific humidity are approaching saturation. Figure 3.4a shows that, for the highest precipitation bins, the average relative humidity ranges from 85–90% in the lower and middle troposphere. The lowest precipitation bin, which contains the vast majority of sondes (and is therefore a much smoother curve) is at the lowest end in relative humidity. However, there is much more of a spread in relative humidity when profiles are conditionally averaged on CWV, as shown in Fig. 3.4b. The relative humidity is around 95% for the very highest bins from 900 hPa through about 600 hPa, and there is also a large amount of variability among the bins at these levels. Clearly, the specific humidity variability shown in Figure 3.3a corresponds to large changes in relative humidity, rather than changes in temperature at constant relative humidity.

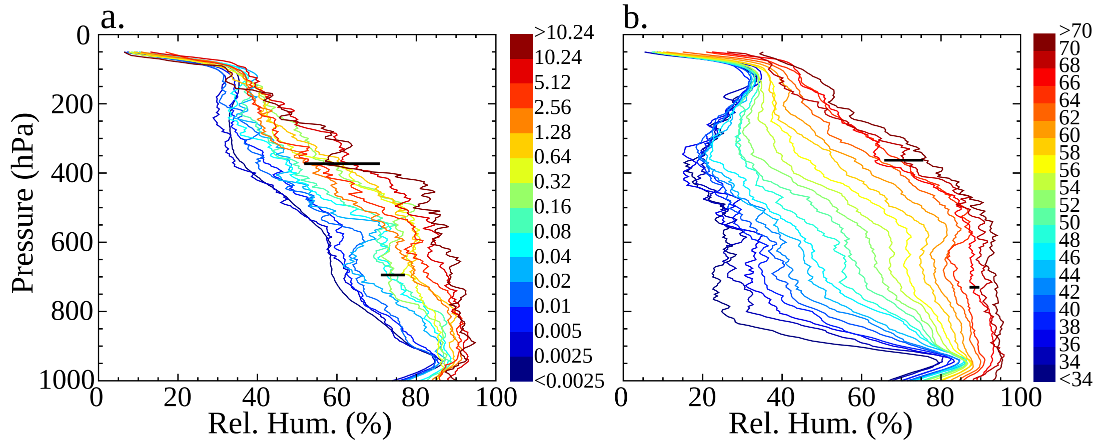

Figure 3.4: Relative humidity (%) profiles conditionally averaged on: (a) 1-hr average precipitation rate in mm hr^{-1} (color bar); (b) column water vapor in mm (color bar). Horizontal bars indicate limits of the maximum, as well as a representative, standard error range below 150 hPa.

3.3.5 Precipitation Lag-Lead Analysis

An important question regarding the association between CWV and precipitation is whether observations can supply an indication of causality. There are reasons to expect feedbacks in both directions. Convection can moisten the column via moisture convergence, detrainment and evaporation (although on a larger scale convection is a net sink of moisture). A likely mechanism by which increased lower-tropospheric moisture could play a causal role in enhancing convection—by allowing entraining plumes to maintain higher buoyancy—is investigated in sections 3.4 and 3.5. Effects of CWV on buoyancy via entrainment (Raymond 2000; Tompkins 2001b; Grabowski 2003) appear to be quite important in Derbyshire et al. (2004) compared to other mechanisms involving downdrafts and cold pools (e.g., Raymond 1997; Tompkins 2001a), although these and radiative mechanisms (Mapes and Zuidema 1996) may also play a role.

A lag-lead analysis on precipitation versus CWV can help strengthen or weaken a causality argument. Figure 3.5 shows profiles of average specific humidity and relative humidity anomalies (taken as differences from the highly populated bin with precipitation less than 0.0025 mm hr^{-1}) for precipitation above 2.56 mm hr^{-1} lagging and leading the radiosonde by up to three hours. The black curves are the same anomaly for no lag, and are placed in all figures for comparison purposes. In general, Figs. 3.5a,b show that q increases slightly in the upper troposphere above 500 hPa during and after precipitation, whereas below 750 hPa q tends to decrease after it rains and is rather constant or even slightly higher before rainfall. This pattern largely holds for the relative humidity profiles shown in Figs. 3.5c,d. Near the surface, temperatures cool on average after precipitation: q is lower than before precipitation while relative humidity is slightly higher. This is likely due to subsaturated downdrafts causing cold pools. Precipitation leading relative humidity in the upper troposphere and lagging relative humidity in the lower troposphere was also found in TRMM KWAJEX data by Sobel et al. (2004). The standard error bars for the q plots give an indication that the lag-lead curves are significantly different from the no-lag curve at most levels, although not necessarily from each other. The relative humidity curves are still significantly different from the no-lag curve at many middle-tropospheric levels, but at upper and lower levels they are not as clearly separate.

This analysis casts doubt on the idea that increased precipitation is the cause of increased CWV, rather than vice versa, at least on these time scales. Following precipitation, there is a small increase in q above 500 hPa, where it does not have much effect on CWV. In the lower troposphere, there is, if anything, a

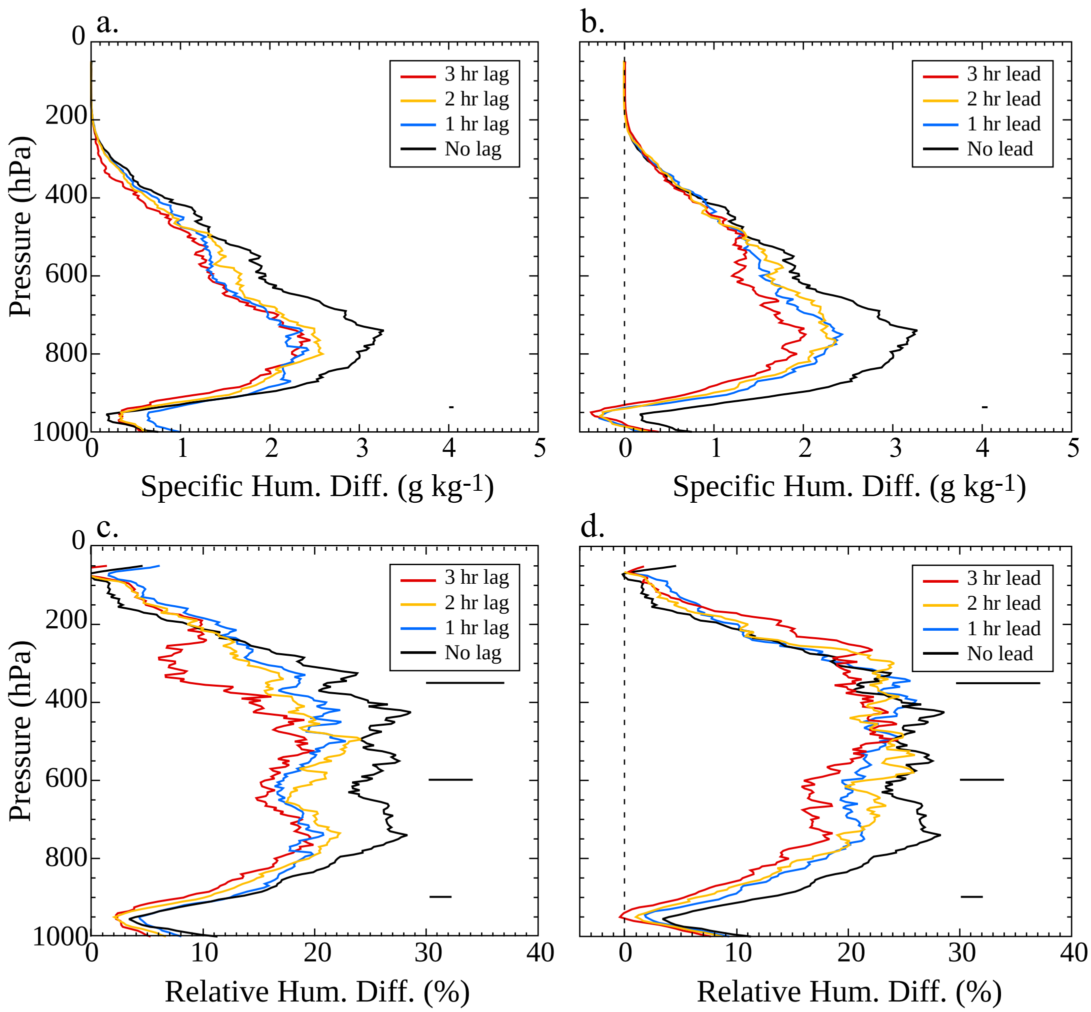

Figure 3.5: Humidity anomalies (taken as differences from the highly populated bin with precipitation less than 0.0025 mm hr^{-1}) for precipitation above 2.56 mm hr^{-1} lagging (before rain) and leading (after rain) the radiosonde by up to three hours, for: (a), (b) specific humidity (g kg^{-1}) profiles; (c), (d) relative humidity (%) profiles. Horizontal bars on right show maximum standard error range for panels (a) and (b), while for panels (c) and (d) they represent the characteristic standard error range for three main vertical regions, with maximums shown in the upper troposphere.

decrease in q after the precipitation. On the other hand, this analysis also does not provide strong evidence for moisture at lower levels increasing greatly prior to precipitation and/or decreasing greatly after precipitation. The moisture at all precipitation lags at nearly all levels tends to be much higher than the moisture for nonprecipitating times, since all of the curves are much closer to each other than they are to zero. Indeed, a comparison with Fig. 3.2 suggests that the main mode of variance for q is captured by all of the curves in Figs. 3.5a,b, regardless of precipitation lag. In other words, within six hours centered around heavy precipitation the atmosphere has already been moistened to near-maximum levels. The smaller amount of variance for these higher precipitation times (Fig. 3.2a, blue lines) is also consistent with the differences between the various curves in Figs. 3.5a,b, which tend to be relatively small but take up a relatively deep layer.

A likely interpretation of these results is that high CWV tends to persist for relatively long times, increasing the chance of precipitation during those times. This is supported by an analysis of microwave radiometer and gauge data from Nauru showing that CWV has much higher characteristic autocorrelation times than precipitation or cloud water (Neelin et al. 2008). These findings also seem compatible with suggestions that much of the variance in water vapor in the tropics may be due to dry air intrusions from the midlatitudes or subtropics that moisten relatively slowly, as mentioned in section 3.3.3 above.

3.4 Impact of tropospheric moisture on buoyancy: basics

3.4.1 Moist stability profiles

Figure 3.6 shows θ_e and θ_{es} for all the bins shown in Fig. 3.3a above 50 mm CWV. (Since we are mainly interested in the changes that occur around and above the precipitation pick-up, which occurs around 67 mm for these data, we have grouped all of the values below 50 mm into only two wide bins, which therefore have proportionately higher counts). An approximate measure (though one that does not account for the effect of condensate on virtual temperature) of parcel buoyancy and convective available potential energy (CAPE) is to draw a vertical line upwards from θ_e at the parcel starting level. Where this line crosses the θ_{es} curve is roughly the level of free convection (LFC) of the unmixed parcel; the area to the left of the vertical line and to the right of the θ_{es} curve is roughly proportional to CAPE. It is clear that, for the highest CWV bins, there are potentially buoyant parcels starting from many lower-tropospheric levels (up to 800 hPa), assuming they can be lifted to their LFCs. This will be discussed further below as it relates to the effect of entrainment at different levels on parcel buoyancies. It is also interesting that the highest θ_e profile is so close to the average θ_{es} bin, indicating that the profiles in the highest CWV bin are close to the saturation specific humidity level of the typical atmospheric temperature profile.

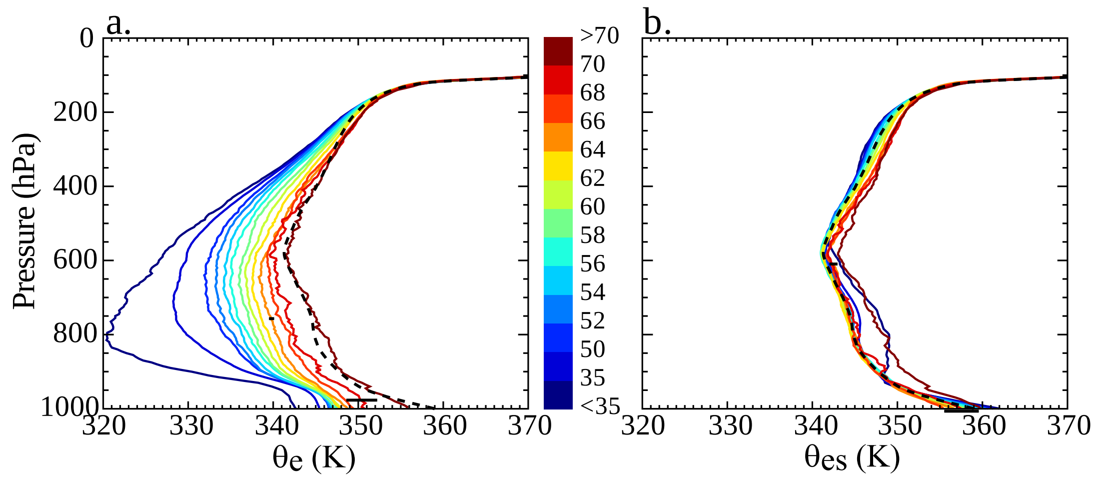

Figure 3.6: Profiles of reversible (a) θ_e (K) and (b) θ_{es} (K). These are conditioned on column water vapor in mm (color bar). The dashed black line, reproduced in each panel, is the bin-count-weighted mean θ_{es} profile for all bins greater than 50 mm. Horizontal bars indicate limits of the maximum, as well as a representative, standard error range below 150 hPa.

3.4.2 Buoyancy contribution for simple entraining plumes

Under the hypothesis that buoyancy effects govern the empirical relationships described above, we calculate the buoyancy perturbation profiles for plumes rising from the subcloud layer under various mixing assumptions. Figure 3.7a shows the resulting virtual temperature perturbations using original sonde data for a hypothetical parcel raised from 1000 hPa that simply conserves total water specific humidity q_t and liquid water potential temperature θ_l, with no entrainment or loss of condensate. These individual sonde perturbation profiles have been conditionally averaged by CWV, with bin spacing as in Fig. 3.6.

Figure 3.7a shows that, without mixing, 1000 hPa parcels easily become buoyant for nearly all the bins. (The CAPE values, obtained by integrating the positive part of these curves times the gas constant over log pressure, range from

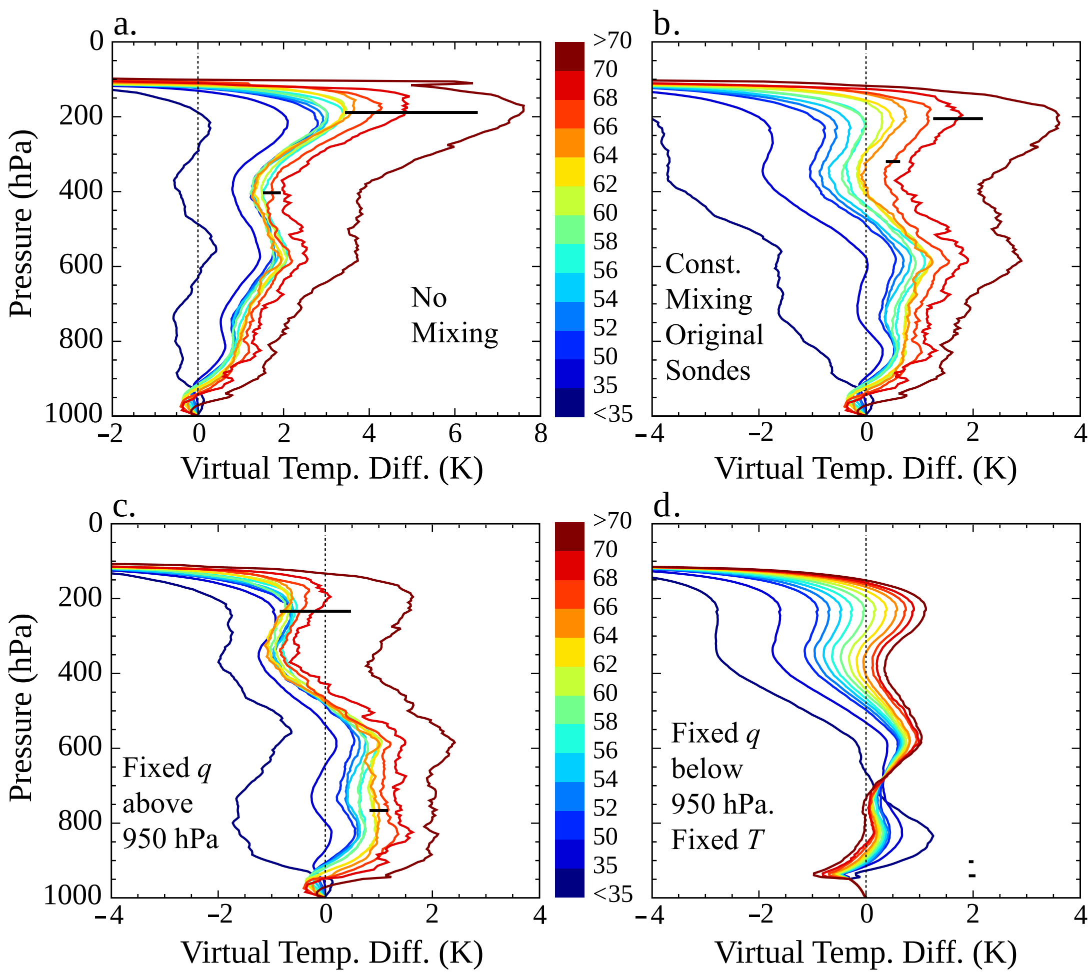

Figure 3.7: Virtual temperature (K) difference profiles conditionally averaged on initial sonde column water vapor in mm (color bar), where the environmental (initial) sonde virtual temperature is subtracted from a profile determined by lifting a 1000-hPa parcel conserving total water and liquid equivalent potential temperature but also including: (a) no environmental mixing; (b) constant 0.5% mixing; (c) mixing with adjusted sonde profiles using mean specific humidity for levels above 950 hPa; (d) mixing with an adjusted sonde profile using mean temperature for all levels and mean specific humidity for levels below 950 hPa. Horizontal bars indicate limits of the maximum, as well as a representative, standard error range below 150 hPa (note that these bars appear on the side in panel (d) for visual clarity). For a few sondes in (c) and (d), q values have been slightly reduced at a few levels to remove supersaturation.

near 0 to around 1,800 J kg^{-1}). This does not correspond to the sharp increase in average precipitation shown for the three rightmost bins as seen in Fig. 3.3b, which have the same bin edges as in Fig. 3.7.

To include entrainment, we begin with a constant isobaric linear mixing with coefficient χ of 0.1% per hPa, following Brown and Zhang (1997), and

$$r_k = (1 - \chi_{k-1})r_{k-1} + \chi_{k-1}\tilde{r}_{k-1}, \tag{3.1}$$

with r a conserved variable, $\tilde{r}$ its environmental value and k denoting pressure level if χ varies.

Brown and Zhang (1997) tuned χ to capture cloud top height in Tropical Ocean Global Atmosphere Coupled Ocean-Atmosphere Response Experiment (TOGA COARE) data. With this mixing, the virtual temperature perturbation profiles (Fig. 3.7b) show a distinctive (and statistically significant) separation around the same bin in which there is a sharp increase in precipitation in Fig. 3.3b.

To show the relative importance of subcloud versus free-tropospheric moisture on plume buoyancy, Figs. 3.7c,d are based on constant entrainment as above but holding q and/or temperature (T) to constant (mean sonde) profiles in different layers. Figure 3.7c shows virtual temperature perturbation profiles for lifted parcels using a constant profile of q above 950 hPa, with T and subcloud q unchanged. Most of the bins have a reduced buoyancy above the subcloud layer, showing the importance of relatively dry air being entrained by the plume (note again that most of the bins chosen have greater than average CWV, since this is the transition region we are interested in). However, the subcloud layer moisture and θ_e, which increase along with CWV, also have an important effect on the buoyancy, which is especially noticeable by the spread in the lower troposphere despite the identical dry air entrainment. If T is also held constant above 950 hPa (not shown), there is an even larger spread throughout the troposphere, implying that tropospheric T tends to increase with increasing CWV, most likely as a result of convection. These increasing tropospheric temperatures offset the higher parcel buoyancies due to higher θ_e in the subcloud layer; this explains the low amount of spread in the upper troposphere seen in Fig. 3.7c.

The results of analysis converse to that of Fig. 3.7c, such that T and q are held to constant mean profiles except for q above 950 hPa, which varies as in the original sondes, are shown in Fig. 3.7d. Clearly, with nothing allowed to vary but the free-tropospheric moisture, there is a significant spread (as measured against standard error ranges) for mixed lifted parcels by the time they reach the upper troposphere. The parcels mixing with the driest air, from the lowest CWV bins, reach negative buoyancy rapidly in the mid-troposphere. The middle and higher bins show significant spread in the upper troposphere, and the top three bins have a small but noticeable separation from the middle ones above approximately 600 hPa. The significance of this differentiation is not certain, but the fact that these are the only three bins which remain positive above 400 hPa is intriguing.

In the lower troposphere, without the compensating effects of higher moist static energy in the subcloud layer, the bins with larger tropospheric water actually show significantly lower buoyancy. This is because moist air is less dense than dry air of the same temperature, so, all else being equal, parcels lifted into a drier environment are more buoyant (until they entrain enough dry air to lose their high moist static energy amounts). The effect of q on virtual temperature also explains the large separation in the lower troposphere in Fig 3.7c. Note that the curves in Fig. 3.7d are much smoother than the other three panels of Fig. 3.7: this is because the environmental temperature, the main component of environmental virtual temperature and the main contributor to the wiggles in the difference profiles, is held constant.

A test of buoyancy profiles conditionally averaged by precipitation rather than by CWV (not shown) showed less spread and less of a trend toward higher buoyancy values with higher precipitation. This is likely due to cold pools and other processes reducing subcloud layer θ_e during actual precipitation (indeed, the lack of trend was reduced when profiles were conditioned on precipitation occurring 3 hr after the sonde launch). Another factor is that, as Fig. 3.1 shows, there is less spread in tropospheric water vapor when conditionally averaged on precipitation as opposed to CWV.

3.5 Water vapor impact on buoyancy: entrainment formulation and microphysics

3.5.1 Sensitivity to entrainment assumptions

The above analysis makes clear that linear mixing (used under the same assumptions, such as neglect of freezing, for which the coefficient was tuned) can yield a transition to buoyant deep convective plumes at a CWV value corresponding to the pick-up in precipitation. However, there are a number of ways in which constant mixing is unsatisfying. Jensen and Del Genio (2006) find that a significant range of constant entrainment values are necessary to reproduce cloud top heights; Kuang and Bretherton (2006) estimate substantially larger values in

CRM simulations, which if implemented in these soundings would not yield the right transition to deep convection.

Recent analysis of Large Eddy Simulations (LES) of convective boundary layers (Siebesma et al. 2007; de Roode et al. 2000; de Haij 2005) points towards a different dependence: a mixing coefficient proportional to z^{-1}, where z is height, in the layer in which plume mass flux is growing. Here we argue that such entrainment arises naturally in plume models, and leads to appealing consequences for thinking about the relative importance of different vertical layers. We then show sensitivity tests for two cases of such mixing. In section 3.5.2 we discuss the sensitivity of the buoyancy analysis to microphysics assumptions.

Deep inflow mixing

Austin (1948) first hypothesized that entrainment due to mass continuity must be necessary for buoyant updrafts with the shapes observed in cumulus clouds. This idea of entrainment as an "ordered inflow" was first termed "dynamic entrainment," as opposed to turbulent entrainment, by Houghton and Cramer (1951). A standard continuity expression for updraft mass flux m (Stommel 1947; Siebesma et al. 2007) is

$$\frac{1}{m}\frac{\partial m}{\partial z} = \epsilon - \delta, \tag{3.2}$$

where ϵ and δ are the entrainment and detrainment rates, respectively. If a deep convective plume consists of increasing mass flux through the whole lower troposphere, with entrainment dominating detrainment, then (3.2) implies large lower-tropospheric entrainment rates. Such deep inflow may be seen in observed core updraft velocity to about 5 km in GATE cumulonimbus (Fig. 5 of LeMone and Zipser 1980) and in cloud-system resolving model (CRM) simulated updraft velocity up to about 6 km (Fig. 8 of Robe and Emanuel 1996). Here we seek simple examples that allow us to visualize the consequences of such "deep inflow" mixing. This can provide a contrasting approximation to "constant" mixing implementations such as that used in section 3.4.2, which effectively assume a large entrainment rate (m increases from 0 to a finite value) through the first layer, and then a much smaller rate of increase in subsequent layers.

From (3.2), we can compute an entrainment coefficient for any mass flux profile, if we neglect detrainment (Ogura and Cho 1973). We consider a family of mass flux profiles increasing smoothly from zero at low levels (and connecting to some other dependence in mid-troposphere):

$$m \propto z^{\alpha}. \tag{3.3}$$

An exponent $\alpha = 1$ would be a linear increase in height, which might correspond to a lower-tropospheric response to a baroclinic wave, or to an entraining plume under circumstances outlined below. An exponent $\alpha = 1/2$ might correspond to the $z^{1/2}$ updraft velocities seen in dimensional arguments as early as Scorer (1957). In (3.2), this mass flux family yields

$$\epsilon - \delta = \alpha z^{-1}, \tag{3.4}$$

which corresponds to the entrainment vertical dependence of Siebesma et al. (2007).

Entrainment effects on a conserved quantity in the plume (e.g., Siebesma et al. 2007) are given by

$$\frac{\partial r}{\partial z} = \epsilon(\tilde{r} - r). \tag{3.5}$$

For clarity we use z coordinates here, although our computations will use the corresponding equation in pressure (p) coordinates. Using (3.5) for potential temperature to diagnose entrainment rates in LES simulations of convective boundary layers (de Roode et al. 2000; de Haij 2005; Siebesma et al. 2007) led to an empirical fit for the mixing coefficient $\epsilon = c_\epsilon z^{-1}$, with $c_\epsilon \approx 0.4$–0.55 (Jakob and Siebesma 2003). For these boundary layer LES studies, ϵ can contain another term that has a maximum near the trade inversion (Siebesma et al. 2007) but we omit this for the present focus on low levels of a deep convective plume.

Relationship to updraft velocity equation

For additional justification, consider an updraft velocity equation (e.g., Siebesma et al. (2007))

$$\frac{\partial w_u^2}{\partial z} = -\frac{c}{z} w_u^2 + aB, \tag{3.6}$$

where w_u is the updraft velocity, B is the buoyancy term, and c and a are constants. The z^{-1} in the first rhs term comes from assuming that ϵ has the form (3.4). The pressure term can be considered as part of B or the coefficients depending on assumptions. Values of the coefficients will be unimportant to the results used here. A solution for this is

$$w_u^2 = z^{-c} \int_0^z a \grave{z}^c B d\grave{z}. \tag{3.7}$$

If B does not vary strongly with height this gives $w_u \propto z^{1/2}$, which yields $c_\epsilon = \alpha = 0.5$ (neglecting detrainment, and assuming that density and plume area coverage do not change rapidly such that m has approximately the same vertical dependence of w_u). This is close to the LES value for shallow convection (Siebesma et al. 2007; Jakob and Siebesma 2003), thus roughly explaining that value. If B instead increases linearly with height, one obtains an updraft velocity that increases roughly linearly with height, $w_u \propto z$. Buoyancy profiles are of course more complex, but roughly linear increases may be seen above 0.6 km in simulated CRM updrafts (Kuang and Bretherton 2006, their Fig. 5). We note that in Fig. 3.7, for different CWV bins, the buoyancy through the lower troposphere can be increasing or relatively constant, and thus for sensitivity studies it is reasonable to use mixing coefficients motivated by each of these two cases.

Deep inflow mixing cases

We thus choose two cases of mixing coefficient vertical dependence: Deep Inflow A corresponds to the Siebesma et al. (2007) LES-based dependence; Deep Inflow B corresponds to an increase in mass flux that is linear at low levels, tapering in mid-troposphere. If detrainment is neglected, these would correspond to an exponent α of 0.4 and 1, respectively, in (3.3) and (3.4). Where z and w are needed for calculations, we use the mean height and density over all sondes to convert to/from p-coordinates.

Specifically, for Deep Inflow A,

$$\chi_k = c_\epsilon z_k^{-1} \Delta z, \tag{3.8}$$

where χ_k is the coefficient in (3.1) (which was held constant in the previous section), Δz is a positive finite difference layer depth, and $c_\epsilon = 0.4$.

For Deep Inflow B, we choose a lower-tropospheric w_u profile that increases nearly linearly at low levels, namely a quarter sine wave in z with zero at 1000 hPa and maximum at 430 hPa (7 km). This roughly approximates the Robe and Emanuel (1996) updraft velocities, and is loosely consistent with observational studies of convective regions (e.g., LeMone and Zipser 1980; Cifelli and Rutledge 1994; LeMone and Moncrieff 1994). Small variations of the m-profile shape have little overall effect, and the magnitude is irrelevant. Mixing coefficients are computed from the p-coordinate version of (3.2), neglecting entrainment, using $\chi_k = -m^{-1}(\partial m/\partial p)\Delta p$, with Δp defined positive. Below 900 hPa, where small mass flux requires caution in finite differencing, we use analytical results from (3.10) below, yielding $\chi_k = (p_0 - p_k)^{-1}\Delta p$. Above 430 hPa, where the mass flux no longer increases, entrainment is set to zero for simplicity.

Vertical weighting of environmental values

For a plume increasing from zero mass flux at pressure p_0 the value of conserved quantity r within the plume at level p is related to the environmental value $\tilde{r}$ by

$$r(p) = \frac{1}{m(p)} \int_{p_0}^{p} \tilde{r} \frac{\partial m}{\partial \grave{p}} d\grave{p}, \tag{3.9}$$

from the p-coordinate version of (3.5) and neglecting detrainment in (3.2). The vertical rate of increase of mass gives the weighting of the environmental variable. For the case of a linearly increasing plume $m = c(p_0 - p)$, this reduces to the vertical average over all levels below:

$$r(p) = (p - p_0)^{-1} \int_{p_0}^{p} \tilde{r} d\grave{p}. \tag{3.10}$$

Therefore, although ϵ and χ decrease rapidly above the surface, this linear case shows that this does not necessarily result in strong dependence on near-surface values. Equal increments of mass are brought into the plume at each level, and the apparent high entrainment is simply because the mass flux is small near the surface. This can also be thought of as plumes rising more slowly having more time for dilution, related to the Neggers et al. (2002) argument for modeling entrainment rates as the inverse of updraft velocity.

This linear case further makes clear why CWV is a very reasonable indicator of buoyancy for deep entraining plumes. For this mass-flux profile, mid-tropospheric buoyancy depends on the environmental water vapor vertically integrated through the lower troposphere, a quantity similar to CWV. Different mass flux profiles yield different vertical weighting. For instance, for z^{α}, the weighting is $z^{\alpha-1}$, which weights lower levels more heavily (when $\alpha < 1$). For $\alpha = 1/2$, and linear decrease in the environmental variable, the level equivalent to the weighted mean occurs at $(p - p_0)/3$, instead of $(p - p_0)/2$. However, even when the vertical mean is not the optimal weighting, CWV will be a reasonable buoyancy estimator for any mass flux increasing through a deep lower-tropospheric layer, especially given the preponderance of variance occurring in the lower free troposphere.

Sensitivity to deep inflow mixing profiles

Figures 3.8a,b show entraining plume buoyancy profiles resulting from Deep Inflow A and Deep Inflow B cases. Although these different mixing profiles show different values in Fig. 3.8 for the exact level of sign change (neutral buoyancy) for the different buoyancy profiles, the qualitative spread and order of the curves is not much different among these two mixing schemes or from those in the buoyancy profiles for the constant mixing in Fig. 3.7b. As in the constant mixing case, only the top few curves (corresponding to the precipitation pick-up in Fig. 3.3b) are buoyant at certain levels (although the vertical levels for which this is true are lower in these latter two mixing cases—the inclusion of ice processes discussed in section 3.5.2 below offers one explanation for this). There is less sensitivity to 1000 hPa θ_e in these vertically dependent mixing cases, as should be expected given the greater emphasis placed on entraining lower-tropospheric air through a relatively deep layer.

For Deep Inflow B (Fig. 3.8b), few CWV bins have buoyant shallow cumulus plumes, but this is not surprising since strong entrainment occurs through the whole lower troposphere. For shallow cumulus, the Deep Inflow A profile—or the full LES-based mixing profile of Siebesma et al. (2007)—is likely more suitable.

Even more than the Deep Inflow A mixing scheme, the Deep Inflow B scheme places importance on all of the lower-tropospheric values, not just the subcloud layer. Since CWV captures variance throughout the lower free troposphere, but includes contributions from the subcloud layer as well, CWV would be a good predictor of buoyancy if real mixing occurred as described by the deep inflow theory, for locations that already have wind profiles typical of deep convection regions. As mentioned above, (3.10) results in equal weighting of all lower-tropospheric levels in the plume buoyancy, implying that CWV, which weights many lower-tropospheric environmental moisture levels, should indeed be a good indicator of deep convection and precipitation.

3.5.2 Sensitivity to microphysics assumptions

An analysis of the sensitivity of the above buoyancy profiles to microphysics assumptions reveals a large amount of uncertainty in the specific values of buoyancy, though not in the monotonic order of the curves. Figures 3.8c,d show the effects of including ice mixing above the freezing level for the Deep Inflow A

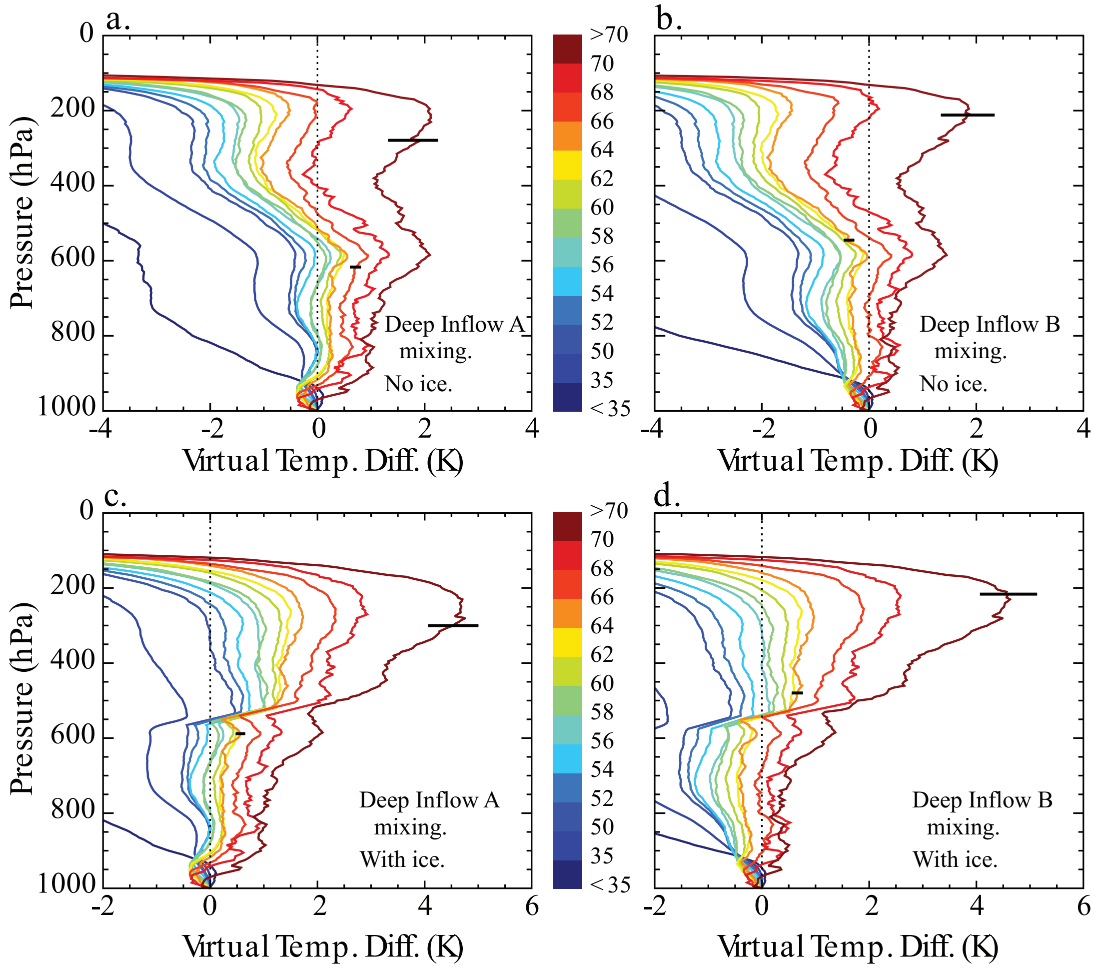

Figure 3.8: Virtual temperature (K) difference profiles conditionally averaged on initial sonde column water vapor in mm (color bar), where the environmental (initial) sonde virtual temperature is subtracted from a profile determined by lifting a 1000-hPa parcel conserving total water and liquid equivalent potential temperature but also including: (a) Deep Inflow A mixing; (b) Deep Inflow B mixing; (c) Deep Inflow A mixing with conversion of liquid to ice, and following an ice-vapor reversible adiabat, above the freezing layer; (d) same as (c), but for Deep Inflow B mixing. In (c) and (d), the jumps in virtual temperature difference at the freezing level for all but the 1 uppermost and 2 lowermost column water vapor bins have been extended from about 10–15 hPa to 30 hPa, with a straight line connecting the otherwise original upper and lower curves, for visual clarity. Horizontal bars indicate limits of the maximum, as well as a representative, standard error range below 150 hPa.

and Deep Inflow B mixing schemes, respectively. The mixing process is similar to that used above, except that instead of conserving the liquid water potential temperature, θ_l, we instead conserve the ice-liquid water potential temperature, θ_{il} (Bryan and Fritsch 2004, their Eq. 23). This reduces to the reversible liquid water potential temperature used above (from Emanuel 1994) when there is no ice. To make the contribution from freezing obvious, all liquid is converted to ice when the plume reaches 0°C; this is the only irreversible process other than the mixing, and is accomplished by equating the total enthalpies of all states before and after the freezing process (Emanuel 1994). The rapid freezing is chosen to make the warming associated with freezing clear in the plots. Implementing the phase change gradually between 0 and -40°C (e.g., Raymond and Blyth 1992; Bryan and Fritsch 2004) would spread this warming through a layer extending upward to about 250 hPa.

The curves including ice for the top CWV bins in Figs. 3.8c,d are buoyant throughout the troposphere; in the Deep Inflow B case, only the top two CWV curves retain their buoyancy, though the third-highest bin becomes only slightly negatively buoyant through a portion of the lower troposphere. Buoyancy above the freezing level for plumes that are negatively buoyant below is unlikely to be realized in practice. Again, the Deep Inflow B mixing is not appropriate for shallow convection, as seen by the lack of shallow buoyant plumes in Fig. 3.8d. In both of these ice cases, there is still a large separation in the curves corresponding to CWV, and a particularly noticeable separation between the top three bins and the lower ones, as discussed in previous figures. This again relates well to the precipitation pick-up seen in Fig. 3.3. The constant mixing case, with freezing including, would not correspond well to this pick-up, since most bins would yield deep convection.

Another aspect of microphysics that affects the buoyancy values of mixing profiles is the treatment of hydrometeors. In all of the above analyses, all liquid and/or ice is retained in the mixed parcels (though of course q_t is one of the mixed variables). Using a pseudo-adiabatic entropy as the conserved variable above saturation, and thereby removing condensate and its effects on buoyancy, tends to increase the buoyancy by as much as 2 K in the mid-troposphere, with lower increases above and below this, and with slight decreases at very high levels (figure not shown). This level of sensitivity to hydrometeor removal, as well as the sensitivity seen for ice processes above, is broadly consistent with the approximately 3 K differences seen in Raymond and Blyth (1992). Again, the order and separation of the curves is not affected much. The positive change comes from the removal of condensate loading in the virtual temperature calculation, while the reduction and eventual reversal of that change at upper levels reflects the lack of additional enthalpy transferred from condensate to air (Emanuel 1994). While the removal of all condensate below the freezing level is unrealistic, above that level it is expected that some of the additional buoyancy gained from the removal of condensate could further increase the strength of updrafts.

3.5.3 Sensitivity to column temperature and relative humidity

The relationship between moisture and precipitation should depend on temperature. For this deep tropical location, temperature variations are small enough that they could be ignored to a first approximation. This was addressed in Fig. 3.2a and Fig. 3.4b, showing that most of the changes of q associated with changes in CWV are due to changes in relative humidity, not to changes in temperature.

A plausible next approximation might be to consider column relative humidity (the ratio of CWV to saturation CWV) following Bretherton et al. (2004). However, the rapid pick-up in precipitation actually has a different temperature dependence (Neelin et al. 2008), occurring at a subsaturation that increases with temperature.

We examined both possibilities in the ARM sonde data. The analyses of Fig. 3.3, Fig. 3.7 and Fig. 3.8 were repeated (i) using column relative humidity; (ii) binning the data by 1000-200 hPa column average temperature (with 1 K width). The precipitation pick-up occurred with similar magnitude to Fig. 3.3 for all cases, and the shifts as a function of temperature appeared consistent with those in (Neelin et al. 2008), whereas normalization by saturation CWV caused overcompensation. However, the results of these analyses were noisy because of small sample size, even for bins only 1 K from the mean. Definitive results would require data through a larger range of temperatures. The buoyancy relationships were noisy as well, but the spread was similar to Fig. 3.7.

3.6 Conclusions

Five years of radiosonde and precipitation gauge data from Nauru Island are used to examine the relationship of the vertical structure of water vapor to tropical deep convection. The leading vertical principal component of specific humidity, which is highly correlated with CWV, peaks in the lower troposphere around 800 hPa and has a relatively small contribution from subcloud levels. The variances associated with CWV are due predominantly to fluctuations in relative humidity, not to changes in temperature at constant relative humidity. Although there is a larger average amount of partial CWV contained between the surface and 850 hPa than there is above 850 hPa, nearly all CWV variance can be explained by the variance in the layer above 850 hPa. The boundary layer contains slightly more water vapor but, since it is tied closely to the surface by turbulent and convective processes, its variance is much smaller, and that smaller variance is itself correlated with the free-tropospheric variance.

Moisture profiles conditionally averaged on precipitation show a strong association between rainfall and moisture variability in the free troposphere, and little boundary layer variability. When precipitation is conditionally averaged on CWV, a sharp pick-up occurs at high enough CWV, consistent with other observational studies (Bretherton et al. 2004; Peters and Neelin 2006). Furthermore, this same pick-up can be reproduced by conditionally averaging precipitation only on the partial CWV from 850–200 hPa, while averaging only on subcloud layer (below 950 hPa) water vapor shows little corresponding response in precipitation. This suggests that moisture above the boundary layer is the key component in the relationship between CWV and the transition to deep convection and higher average precipitation rates.

Because CWV is widely observed from satellite retrievals, we seek to understand why it proves such a useful indicator of favorable conditions for tropical deep convection. The buoyancy of plumes rising under different conditions, for several entrainment assumptions, provides insight. The transition to high precipitation rates at sufficiently high CWV appears to depend primarily on free-tropospheric moisture, which can greatly affect the buoyancy of lifted parcels undergoing entrainment. There is also a dependence on the small but significant correlation between CWV and subcloud layer moisture and θ_e.

Entraining plumes tend to be far more buoyant at middle and upper levels for profiles with larger CWV values. This is robust for all three mixing profiles analyzed, although the level at which positively buoyant parcels reach neutral buoyancy differs, as does the relative weighting of entrainment from the free troposphere and boundary layer. Constant mixing, similar to many convective parameterizations, must be rather small to not kill convection by the time it reaches the middle troposphere, and thus tends to emphasize boundary layer θ_e. Using mixing values from Brown and Zhang (1997) can give the transition to deep convection at the approximate CWV value at which precipitation picks up, but only if freezing is neglected. Two "deep-inflow" mixing profiles based on increasing mass flux through a deep lower-tropospheric layer are considered. One is based on LES studies of entrainment in convective boundary layers (Siebesma et al. 2007), and a second assumes entrainment associated with a mass flux profile increasing linearly at low levels, to a maximum at mid-troposphere. Both yield the increase in buoyancy as a function of CWV. When simple freezing physics is included, the deep inflow mixing cases both give better correspondence than constant mixing between the pick-up in precipitation in the upper few CWV bins and buoyancy available for deep convection. Analytic results for these mixing profiles show how buoyancy in the mid-troposphere depends on a weighted vertical average over the lower troposphere; in the case of a linearly growing plume, all lower-tropospheric levels are weighted equally. In the presence of such entrainment, CWV is thus a very reasonable measure of the buoyancy available to a deep convective plume.

These results underline the key role that free-tropospheric moisture plays in the transition from shallow to deep convection. The observed pick-up of precipitation with CWV is linked to increased buoyancy of entraining plumes, and the importance of accurately representing the entrainment process to obtain this sensitivity is shown. This adds an observational constraint on entrainment that may be useful in revising GCM convective parameterizations, and points toward entrainment schemes associated with more realistic mass flux profiles than the commonly used constant mixing.

Chapter 4

Temporal Relations of Column Water Vapor and Precipitation

Abstract

Empirical studies using satellite data and radiosondes have shown that precipitation increases with column water vapor (CWV) in the tropics, and that this increase is much steeper above some critical CWV value. Here, eight years of 1-minute resolution microwave radiometer and optical gauge data at Nauru Island are analyzed to better understand the relationships between CWV, column liquid water (CLW), and precipitation at small time scales. CWV is found to have large autocorrelation times compared with CLW and precipitation. Before precipitation events, CWV increases on both a synoptic-scale time period and a subsequent shorter time period consistent with mesoscale convective activity—the latter period is associated with the highest CWV levels. Probabilities of precipitation increase greatly with CWV: 10–12 hr after high CWV, there are still significantly higher probabilities. Even in periods of high CWV, probabilities of initial precipitation in a 5-minute period remain low enough that there

tends to be a lag before the start of the next precipitation event. High CWV, then, can be thought of as a suitable predictor variable for precipitation. Power law scaling of precipitation events, noted in previous studies, is seen to depend on CWV.

4.1 Introduction

In the previous chapter, we showed that high column water vapor (CWV) corresponds to high precipitation at little or no lag. Furthermore, there is evidence that boundary layer and lower-tropospheric moisture can lead precipitation by an hour or two while middle- and upper-tropospheric moisture tends to lag precipitation by the same amount of time, in agreement with Sobel et al. (2004). Here we explore the relationship between CWV and precipitation at various lag times (from a few minutes to a few days).

One question motivating this study is the extent to which causality can be inferred in the CWV/precipitation relationship. Although observations cannot completely prove that one field controls the behavior of the other, evidence that changes in one of them precede changes in the other can lend credibility to a causality argument. We first investigate the separation of characteristic autocorrelation time scales for these two fields, since this separation is important to understanding the relationship.

We argue that CWV can be seen as a relatively slowly changing predictor variable that increases the probability of precipitation events, which have much shorter characteristic time scales. Of course, there are likely to be feedbacks leading each field to increase the other, at least in certain circumstances (e.g., Grabowski and Moncrieff 2004). However, these feedbacks are usually thought of as happening at the mesoscale, whereas it will be shown that CWV can also increase over longer time scales without obvious interactions with precipitation until higher CWV are reached.

4.2 Data and Methodology

The Department of Energy's Atmospheric Radiation Measurement (ARM) Program (Stokes and Schwartz 1994) maintains a climate observation site at Nauru Island (0.5°S, 166.9°E; Mather et al. 1998). We have analyzed microwave radiometer (MWR) CWV and column liquid water (CLW) data as well as optical gauge surface precipitation rates from 20 November 1998 to 16 August 2006. The data are at 1-min temporal resolution. The precipitation rate has 0.1 mm hr^{-1} resolution and 0.1 mm hr^{-1} uncertainty.

The MWR instrument passively measures downward microwave radiation reaching the surface at 23.8 and 31.4 GHz. To remove version inconsistencies in the retrievals of CWV and CLW, we have re-analyzed the MWR brightness temperatures using the latest ARM algorithms based on Liljegren et al. (2005). These algorithms are weighted linear combinations of the optical depths of the two channels (which are derived from the brightness temperatures), with the weights determined by linear regression over a climatological range of conditions co-measured by radiosondes. The MWR instrument showed large agreement with high-quality radiosondes from the Japanese R/V *Mirai* during the Nauru99 campaign, with a maximum CWV difference of 3 mm (Westwater et al. 2003).

There is fairly good agreement between CWV from the MWR and that from the radiosondes analyzed in Holloway and Neelin (2008), with a correlation of 0.92, although at high CWV values the radiosondes tend to be moister. This could have something to do with the wet window problem: the radiometer cannot function correctly when its window becomes moist. When this happens, a heater and fan turn on until the window dries. The data is flagged as missing until the heater and fan shut off and the window is dry.

Because we are interested in CWV and CLW values near precipitating times, we need to find a way to estimate these fields when the MWR window is wet. We have chosen to interpolate over gaps less than 12 hr long for CWV and CLW values, and we identify these fields as "gap-filled" data hereafter (discussed further in section 4.3 below).

4.3 Temporal autocorrelation scales and gap-filled data

Figure 4.1 shows that CWV has fairly long autocorrelation times compared with CLW and precipitation. The autocorrelation is still above 0.7 even at 24-hr lag. This has a number of potential implications for the CWV/precipitation relationship, and we explore or make use of some of these implications in this study. These include links to mechanisms of mesoscale organization as well as the extent to which CWV might be used as a predictor of future precipitation, for instance in stochastic parameterization.

In this study, there is a practical reason to utilize this long autocorrelation time in order to justify interpolating over gaps less than 12 hr long caused by the wet window problem, which eliminates CWV and CLW measurements during

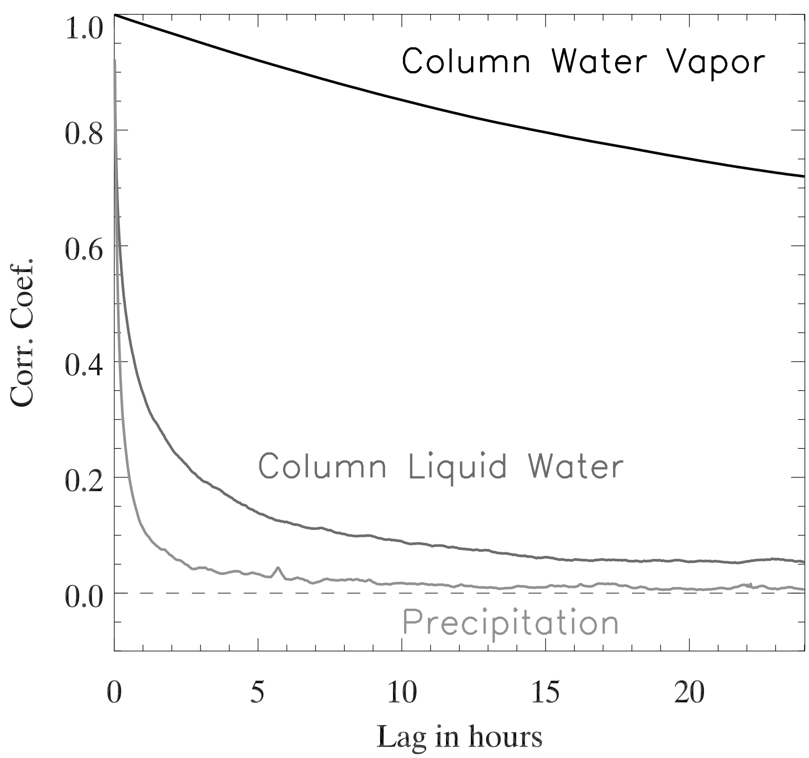

Figure 4.1: Autocorrelation versus lag for column water vapor (black), column liquid water (dark gray), and precipitation (light gray), for all data.

and just after rainfall as discussed in section 4.2. This interpolation is harder to justify for CLW, which has relatively short autocorrelation scales, so gap-filled values for that field should be considered with more caution.

Figure 4.2 shows examples of five 5-day time series of CWV (black dots) with gray circles showing gaps filled by interpolation and red open circles showing precipitation. These five series were chosen from 20 randomly-selected periods, and represent the main features and variability contained in those time series. It is clear that many CWV peaks are still cut off, meaning we are undersampling the highest values. One gap is even longer than 12 hr and is not filled. Large gaps seem to be preferentially cut off before the peak, leading to interpolated lines that slope upward in time—this could affect some composites done in later sections. There are also some times, such as in the top panel of Fig. 4.2, when the interpolation is done over very small gaps, mainly due to temporary changes in instrument temporal resolution, and should not affect the results at all. The other gaps are all due to precipitation, with the wider gaps generally associated with stronger precipitation that lasts longer.

Comparing histograms of gap-filled and non-gap-filled CWV, we can see from Fig. 4.3 that the higher bins tend to be disproportionately increased for gap-filled data. From Fig. 4.2 we know that observations falling in the highest bins are being attributed to slightly lower bins in the gap-filled data, but this problem is not so severe as to create a spurious bump in the histogram. Since gap-filled data still underestimate the occurrences of high CWV, indications of the importance of high CWV are likely to be conservative. Gap-filled data are clearly superior to non-gap filled data for the purposes of this study, since the gaps are not random,

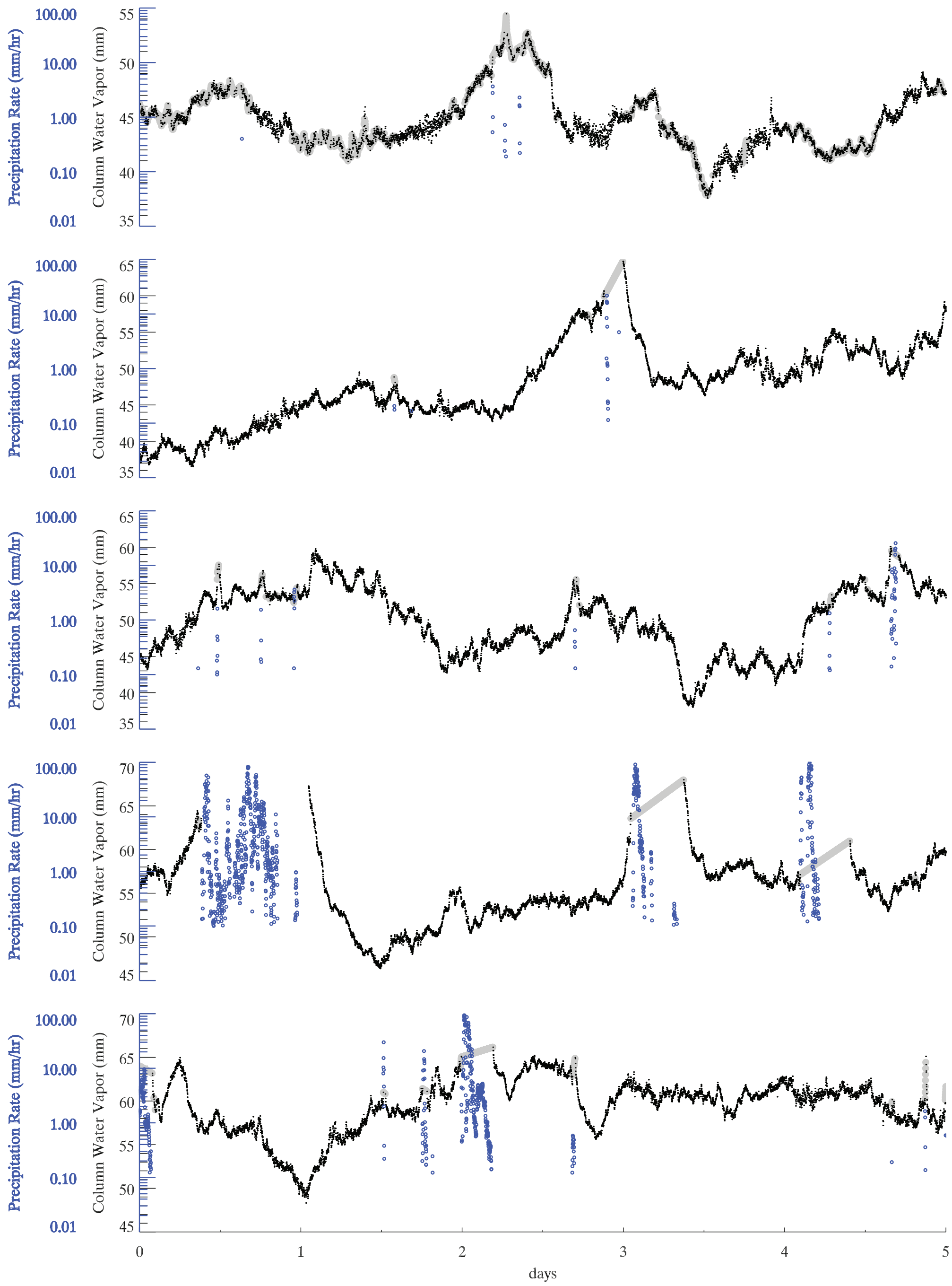

Figure 4.2: Five example 5-day time series of column water vapor (black dots), showing filled gaps in gray. Red open circles show precipitation (log scale).

occurring preferentially at the most important part of the distribution and the most relevant parts of the time series—those surrounding precipitation and high CWV values.

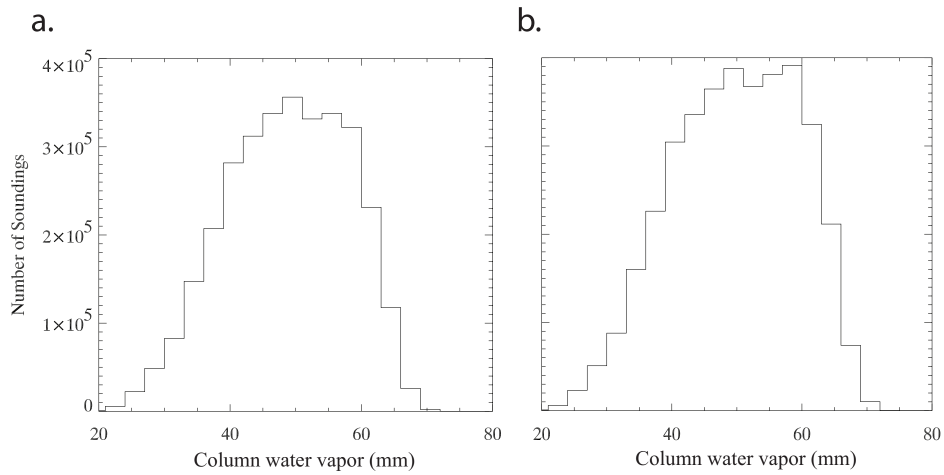

Figure 4.3: Histograms of column water vapor values for (a) original data; (b) gap-filled data. Bins are 3 mm wide.

4.4 Precipitation pick-up as a function of lag

Even at 3-hr lag and for non-gap-filled data, Fig. 4.4 shows that we can reproduce the pick-up of precipitation at high CWV seen in earlier satellite-based studies (Bretherton et al. 2004; Peters and Neelin 2006) and in radiosondes at the same Nauru ARM site (Holloway and Neelin 2008). This lag is necessary here to avoid the wet window problem discussed above. There are proportionately few values of very high CWV available even for the gap-filled data, as compared with the radiosonde data in Holloway and Neelin (2008), probably because of the wet window problem and the problems the MWR can have at high CLW values. This makes it impossible to test the power law relationship at high CWV as seen in

Peters and Neelin (2006).

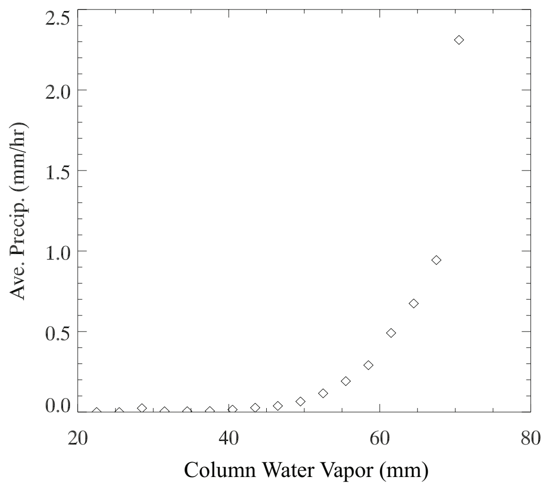

Figure 4.4: Precipitation conditioned on column water vapor 3 hrs. earlier, with 3-hr bin width. Bins with fewer than 1000 counts are excluded.

Figure 4.5 shows the CWV relationship to average precipitation rate (on log-scale) at ±12-hr lags (measured in time after CWV measurement), using gap-filled data. There is certainly an increase of precipitation with CWV at all lags. There is an overall fairly symmetric pattern in time, although the center of the precipitation peak tends to occur about an hour before the high CWV measurement. On the other hand, there is more precipitation at long lags (6–12 hr) after high CWV than there is for those same lead times. This suggests that the CWV/precipitation relationship is not simply due to rain moistening the air immediately around it, which would cause a reversed lag relationship.

4.5 Time composites on precipitation events

To investigate the average behavior of CWV around a precipitation event, we have made composites centered on locally high precipitation (above the median

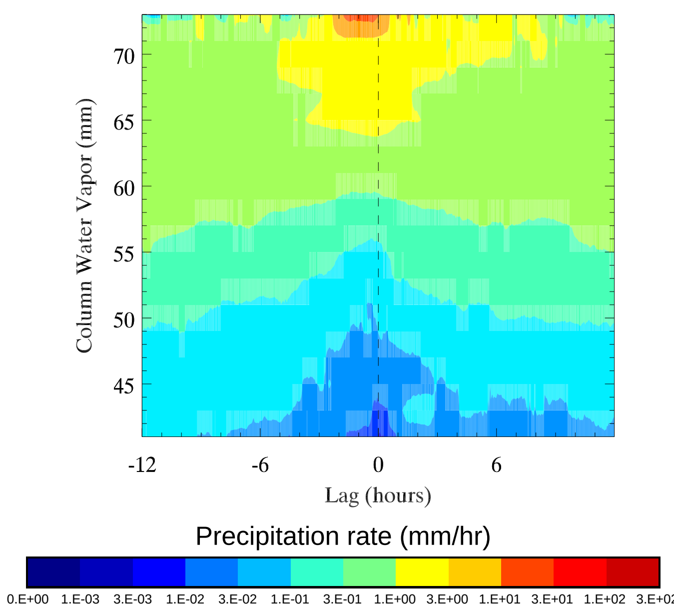

Figure 4.5: Precipitation rate conditioned on gap-filled column water vapor at various leads/lags. Lag axis measures time after CWV measurement (i.e. CWV leads rainfall on the right side of the diagram).

positive precipitation rate, 0.97 mm hr^{-1}, and higher than neighboring events within the composite window). Figure 4.6 shows these composites for gap-filled CWV and CLW, as well as for precipitation itself in logarithmic scale, for $\pm$48 hr of a precipitation maximum (330 events). The relatively long, gradual approach to higher CWV values (as compared with the narrow peaks of CLW and precipitation) stands out and is consistent with the autocorrelation scales shown in Fig. 4.1.

The gradual rise from mean gap-filled CWV conditions, labeled "synoptic-scale increase", starts about 40 hr before the precipitation peak and lasts about 33 hr. If we assume advection by a mean wind of 10 m s^{-1}, this translates to a spatial scale of almost 1200 km. In contrast, about 7 hr before the peak there is a much steeper increase in CWV. This seems to be a separate, "mesoscale" feature (whose corresponding spatial scale by the same estimation would be about 250 km), which is larger than both the precipitation increase (deep convective element) and the CLW increase. The existence of such a feature suggests a role of CWV, and therefore lower-free-tropospheric moisture (Holloway and Neelin 2008), in mesoscale convective organization, consistent with the positive moisture-convection feedback found in many previous studies (e.g., Parsons et al. 2000; Tompkins 2001b; Grabowski 2003; Derbyshire et al. 2004; Bretherton et al. 2004). Specific mechanisms potentially explaining this feature include the initial upward motion of a gravity wave propagating ahead of a convective system with top-heavy heating (e.g., Nicholls et al. 1991; Mapes 1993; Liu and Moncrieff 2004) and a "mesolow" (c.f. Houze 2004).

In the CLW composite, there seems to be a somewhat slower decrease after

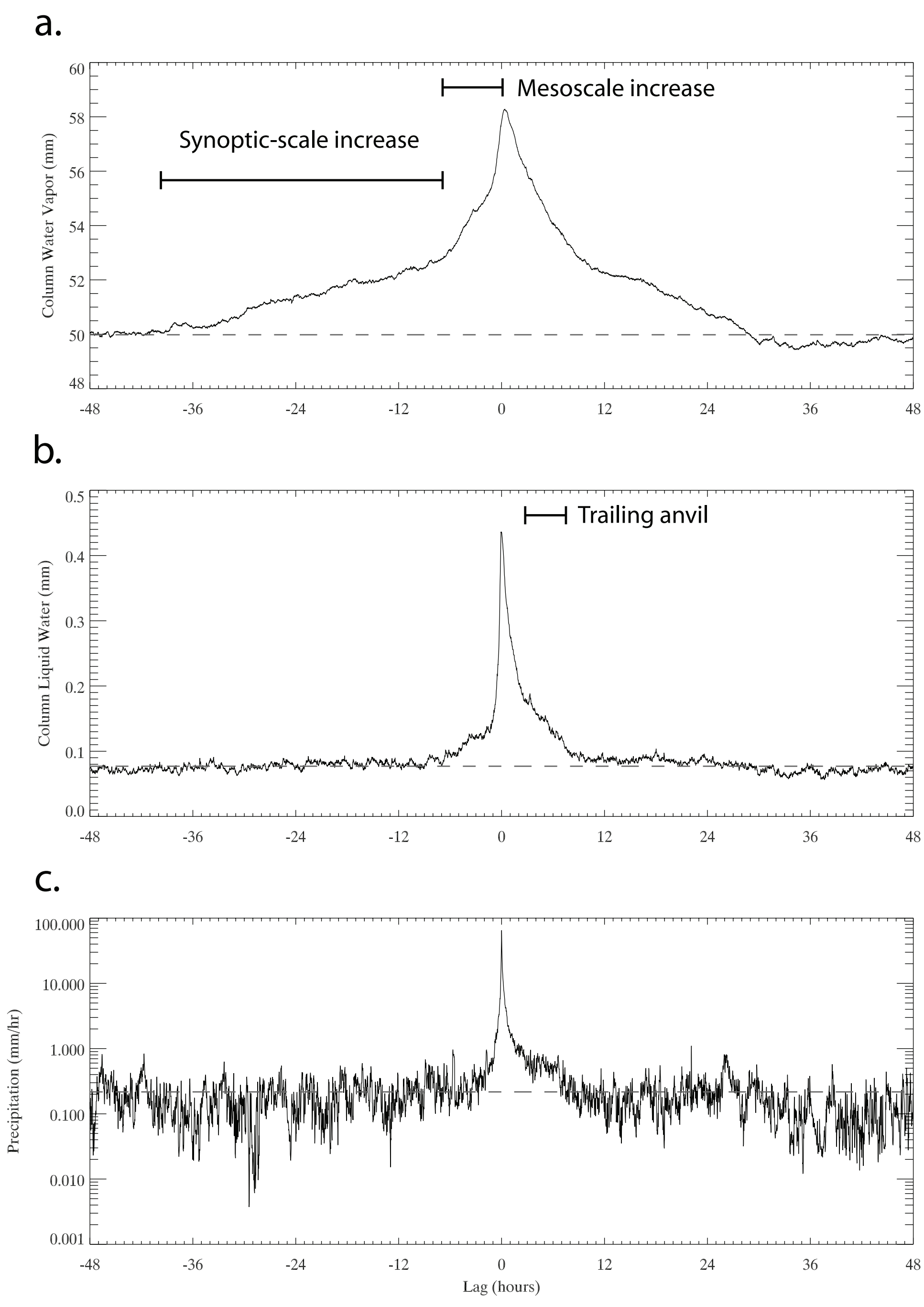

Figure 4.6: (a) Gap-filled column water vapor, (b) gap-filled column liquid water, and (c) precipitation rate (log-scale), composited on locally high (above 0.97 mm hr^{-1}) precipitation events for ±48-hr lags (330 events). Dashed lines are longterm means. Labels indicate periods for which interpretations are discussed in the text.

the peak than increase before it. This decrease could be the indication of a "trailing anvil," and can also be seen in the precipitation composite. Convective anvils, composed of upper-tropospheric stratiform cloud fed by outflow of liquid water from deep convective updrafts, tend to trail the deep convective element because of propagation and/or wind shear (Houze 2004). In fact, the relatively long time with somewhat elevated precipitation in Fig. 4.6, compared to the shorter time around the peak, could support other studies that show around 40% of tropical rain caused by stratiform clouds, typically in anvils blown from the tops of convective systems (Schumacher and Houze 2003). On the other hand, the asymmetric CLW and precipitation peak could suggest a hysteresis in the system—once a threshold is crossed, for instance in CWV, the system tends to rain for a while, perhaps because of the positive feedbacks between CWV and deep convection discussed above.

Figure 4.6 indicates that the synoptic-scale rise before the precipitation event is fairly slow and constant, whereas the corresponding decline afterwards, while perhaps delayed by a few hours, is somewhat steeper, resulting in values after 24 hours that are lower than the values at 24 hours before peak. This does not support the idea that precipitation is the main cause of high CWV. A different proposed mechanism for slow CWV rise during relatively suppressed conditions such as a dry intrusion (Numaguti et al. 1995; Mapes and Zuidema 1996; Brown and Zhang 1997; DeMott and Rutledge 1998; Parsons et al. 2000), namely that shallow cumuli form and then evaporate into the free troposphere, does not show up in the CLW composite. However, it may be that the presence of average CLW over an extended time helps increase lower-free-tropospheric moisture, and thus

CWV, without showing up as an increase in CLW.

Figure 4.7 shows composites within ±12 hr of a precipitation event (982 events total), again using gap-filled CWV and CLW fields. Note that this is not just a magnification of the 24 hours around the peak in Fig. 4.6, since there are more events here due to the smaller window for which to exclude lower-value neighbors. These plots show CWV peaking just after the precipitation, with CLW peaking just before. Again, values seem to decrease more slowly after the event than they increase before the event, especially for the CLW and precipitation composites. This is likely related to a trailing anvil (stratiform rain) and/or a possible hysteresis linked to system memory after crossing a CWV threshold required for deep convection, as discussed above.

The precipitation rate in Fig. 4.7c stays mostly below the longterm average until well after the CWV begins to rise, again suggesting that precipitation is not causing the main CWV increase. It is somewhat difficult to see a scale separation at 7 hr before the peak, the "mesoscale increase" seen in Fig. 4.6, although there is a slow increase of CLW beginning at that time. There is perhaps a somewhat steeper rise in CWV starting about 6 hours before the peak, and there is an even steeper rise in all three composites starting about an hour before zero lag. Since this composite contains more small precipitation events, there may be a tendency to see smaller scales of CWV increases than in Figure 4.6, since it is likely that we are averaging over somewhat sharper increases starting at different times, and likely having longer scales for higher precipitation maxima.

Figures 4.8–4.9 show corresponding figures for composites made on the beginning of events larger than the median positive precipitation rate (0.97 mm hr^{-1})

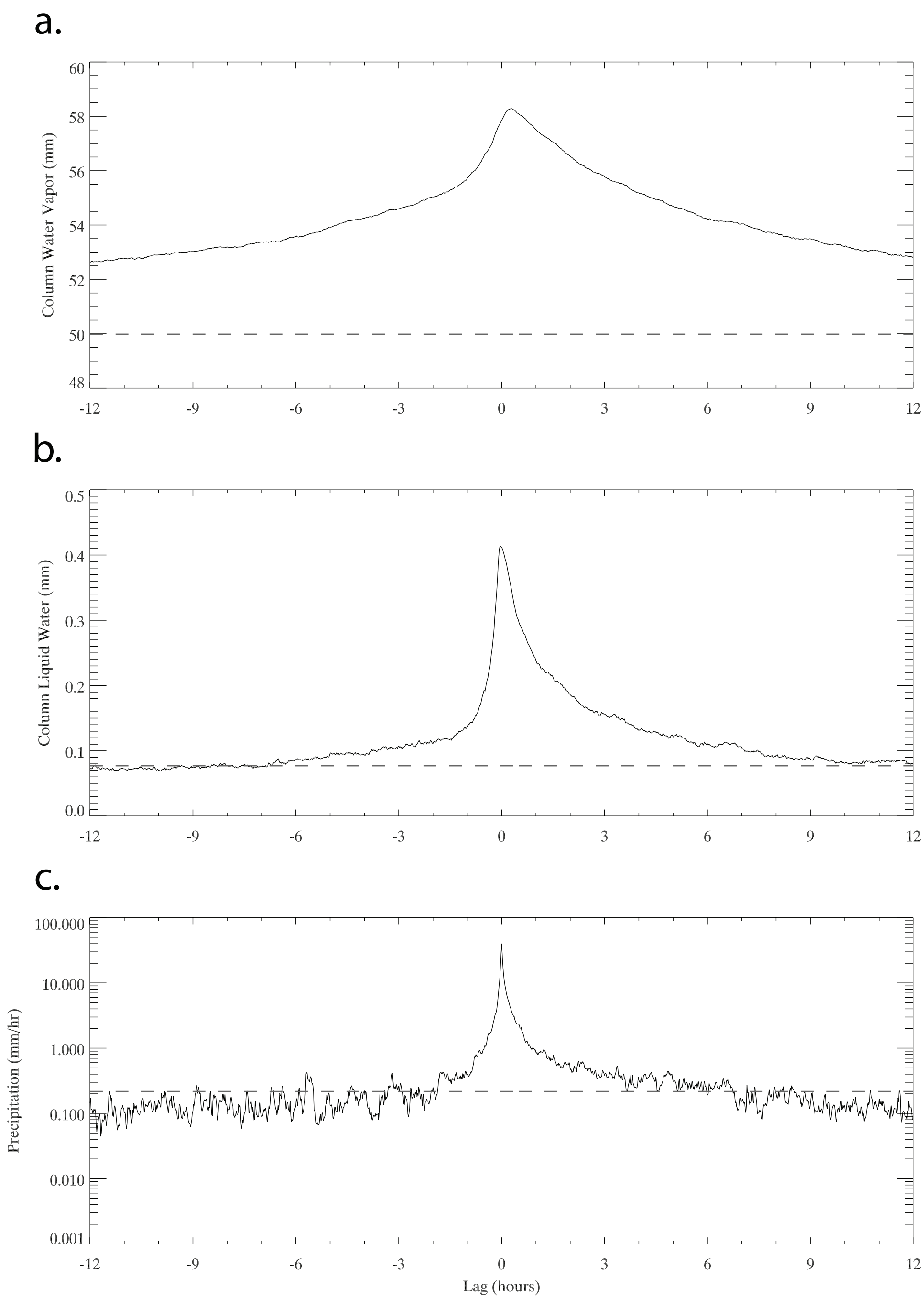

Figure 4.7: (a) Gap-filled column water vapor, (b) gap-filled column liquid water, and (c) precipitation rate (log-scale), composited on locally high (above 0.97 mm hr^{-1}) precipitation events for $\pm$12-hr lags (982 events). Dashed lines are longterm means.

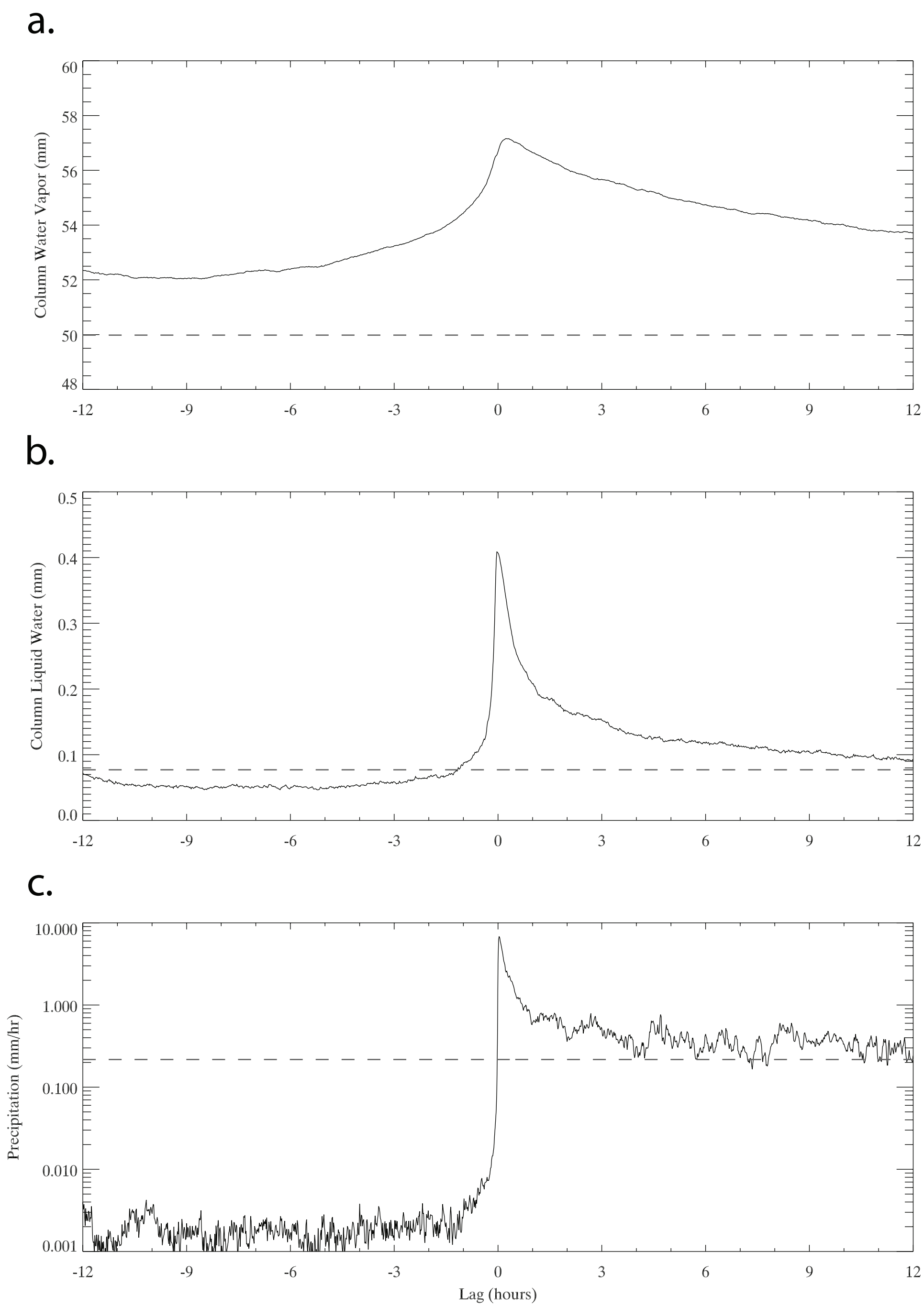

Figure 4.8: (a) Gap-filled column water vapor, (b) gap-filled column liquid water, and (c) precipitation rate (log-scale), composited on the ends of 12-hr low-precipitation (below 0.97 mm hr^{-1}) periods for $\pm$12-hr lags (1109 events). Dashed lines are longterm means.

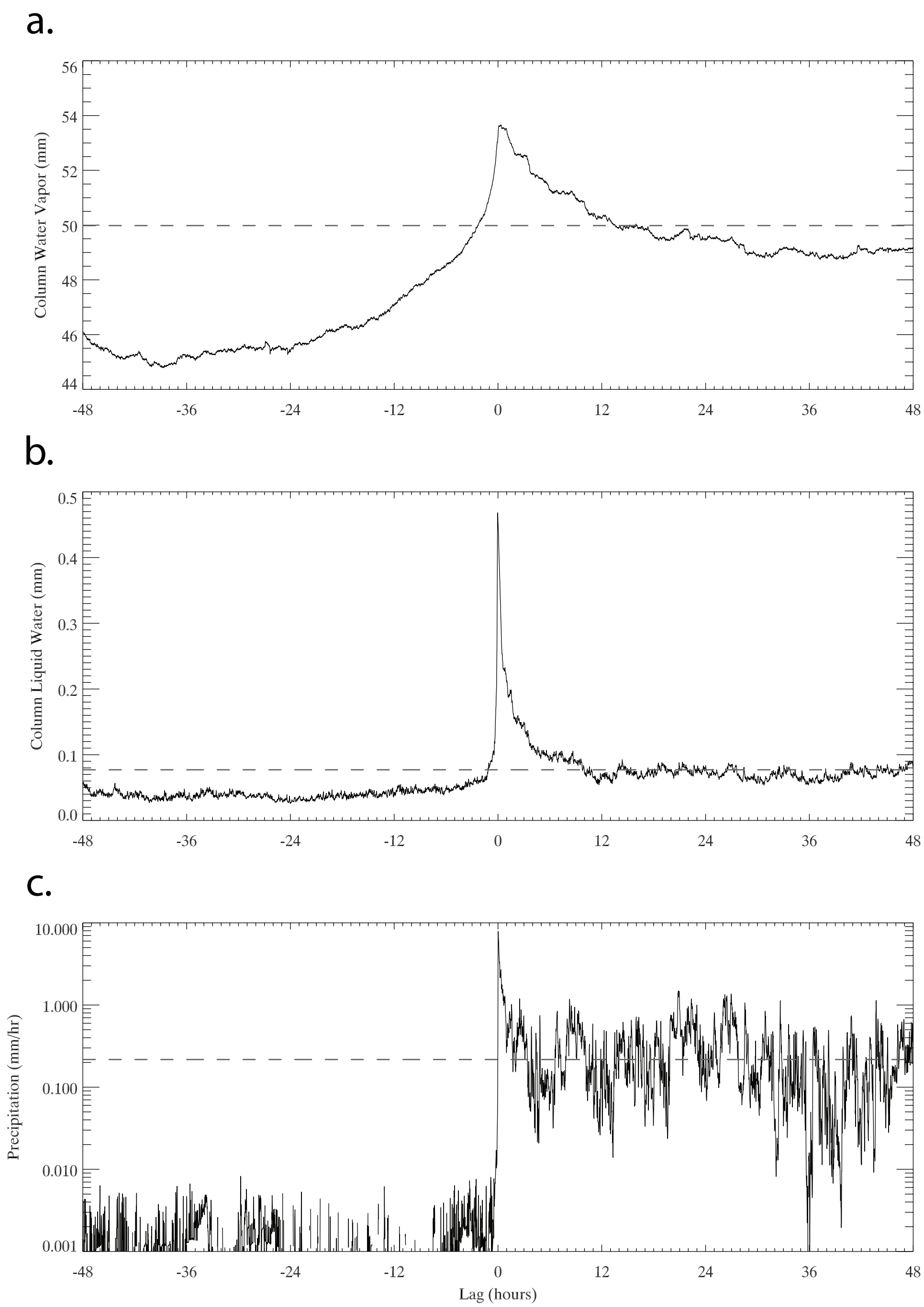

Figure 4.9: (a) Gap-filled column water vapor, (b) gap-filled column liquid water, and (c) precipitation rate (log-scale), composited on the ends of 48-hr low-precipitation (below 0.97 mm hr^{-1}) periods for ± 2 day lags (184 events). Dashed lines are longterm means.

and preceded by periods below that rate (lasting for 12 hr and encompassing 1109 events for Fig. 4.8 and lasting 48 hr and encompassing 184 events for Fig. 4.9). These figures show that, even in the absence of significant rain at Nauru, there is a rise of CWV preceding the return to normal rainfall. The CWV and CLW values before precipitation are lower than normal in Fig. 4.9, with higher levels afterwards corresponding to wetter conditions.

4.6 Transition Probabilities

Figure 4.10 shows the probability of precipitation during the subsequent 5 minutes or 1 hr after a given CWV value, conditioned on there being no rain at the time of the CWV measurement. In other words, the figure shows the probability of transition from no rain to rain as a function of CWV. This conditional probability exhibits a pick-up at high CWV similar to the pick-up of the mean precipitation (although the mean precipitation also has a contribution from an increase in the expected value of the precipitation given that it is raining). These probabilities are not very high for the water vapor values that most commonly occur. Hourly probabilities rise to not quite 45% even at high values (69–72 mm) of CWV. At still high but more common values of CWV, around 54 mm, the probability of rain in a given hour is less than 15%. Thus as CWV rises, there will typically be a lag before the rain begins, which should average a couple of hours long—for instance, using an hourly precipitation probability of 15% typical of CWV around 55 mm, and an independence assumption, the probability of *no* rain in two hours is $(1 - 0.15)^2 = 72\%$. For the highest CWV bin, 43% precipitation probability yields a probability of no rain in two hours of over 30%.

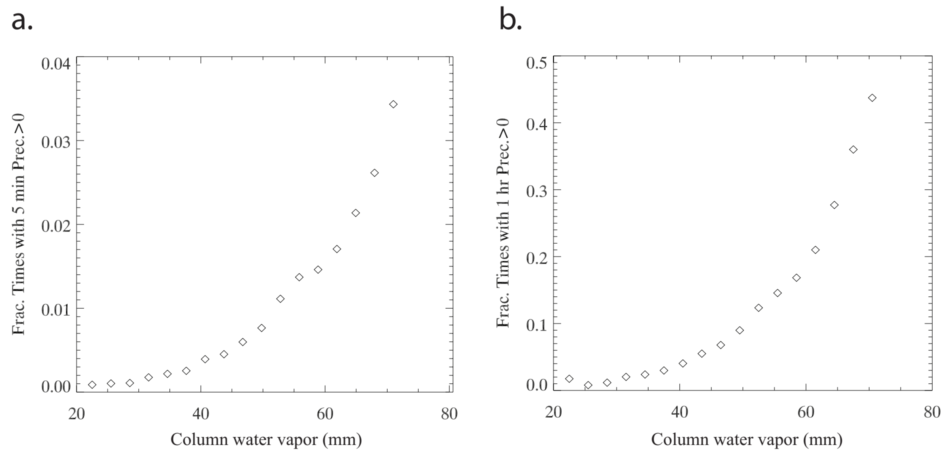

Figure 4.10: Fractional probability of positive precipitation, given no initial precipitation, in the next (a) 5 minutes, and (b) 1 hr. These are conditionally averaged on column water vapor 1 minute earlier at 3-mm bin width. Bins with fewer than 1000 counts are excluded.

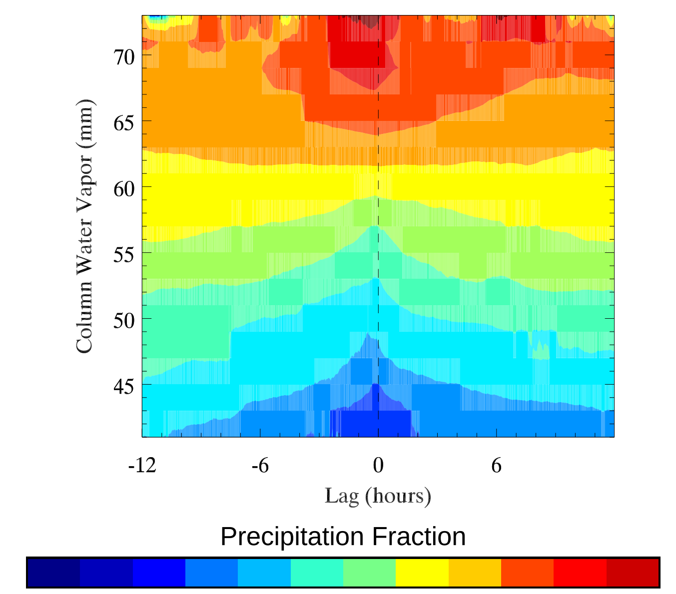

Figure 4.11: Fraction of positive precipitation conditionally averaged on gap-filled column water vapor at various leads/lags. Lag axis measures time after CWV measurement (i.e. CWV leads rainfall on the right side of the diagram).

The independence assumption should only be used to give rough estimates. As a check, using the probabilities based on the 5-min data in Fig. 4.10a, the probability of having no rain for one hour with initial CWV at 69–72 mm is 65%, somewhat higher than the correct value of 57% (taking 1 minus the 1-hr rain probability at that CWV value in Fig. 4.10b). We also note that the wet-window problem (see section 4.2) can affect the estimated probabilities slightly (using gap-filled data, not shown, gives slightly larger estimated probabilities).

This conditional probability is similar to a statistic one might use in a stochastic convection scheme: the probability of launching a convective element, for a given state of the water vapor (and temperature), given that the grid cell is not yet convecting. The measurement here is an imperfect analog, since it is for the initiation of precipitation, and we do not know precisely the spatial area to which this probability corresponds. Nonetheless, it provides motivation for revising parameterization assumptions that initiate deep convection and precipitation deterministically and immediately upon reaching a certain state of temperature and moisture.

The precipitation probability without conditioning on zero precipitation at time zero also shows a similar shape pick-up to the curves in Fig. 4.10. The lag behavior of this probability (Fig. 4.11) has a similar pattern to that of the mean precipitation pickup at many lags and leads (see discussion of Fig. 4.5 above). The values are higher for the probabilities in (Fig. 4.11) than for the corresponding values conditioned on zero at each value of CWV—this is because dry times are much more likely to follow other dry times than they are to follow wet ones, and because there is also some tendency for wet times to follow each other. This behavior should be most pronounced for probabilities with small time windows.

4.7 Periods of high column water vapor

Fig. 4.10 shows that even at relatively high CWV values the probability of rainfall, given no initial rain, is still not that high. This makes it interesting to look at high CWV times and see how precipitation behaves in those times. Another question that arises from the above analyses is whether the CWV increase, and the precipitation pick-up at high enough CWV, are actually sharper than they appear from composites and averages. We may be smoothing these increases by averaging over many different, sharp increases that occur at different lags.

To investigate these points, we composite CWV, CLW, and precipitation rate on locally high CWV. However, we then center our composite window not on these maxima, but on the crossing point from below to above 54 mm CWV that precedes and occurs closest to the maxima in each case (even if this is before the beginning of the initial time window used to identify maxima).

These composites are shown in Fig. 4.12, which include 282 events. Note that there is indeed a rather sharp increase of precipitation rate, and an even more pronounced sharp increase in CLW, along with the sharp increase in CWV that is partly a product of the compositing method. The values of CLW and precipitation respond immediately, although the increases are relatively small compared with those in Fig. 4.6, which centered its composite on the relatively narrow deep convective peaks.

To measure this effect further, we composite precipitation rate over one hour starting at the first precipitation at or following the transition to 54 mm CWV

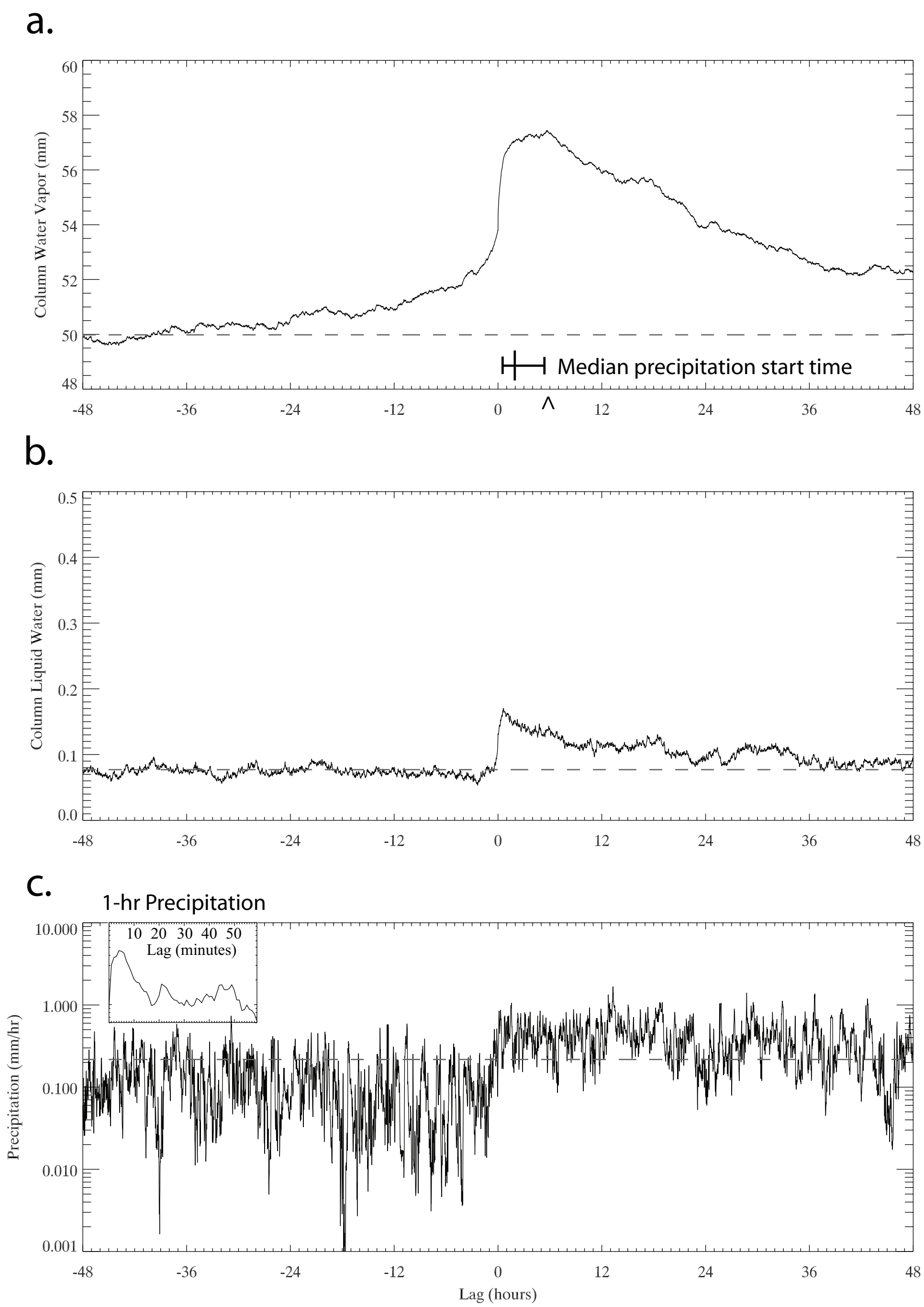

Figure 4.12: (a) Gap-filled CWV, (b) gap-filled CLW, and (c) precipitation rate (log scale), composited on locally high CWV (above 54 mm and largest value within ±48 hours), but centered on last value below 54 mm CWV before maximum (282 events). Inset shows 1-hr precipitation event composites (see text). In (a), median and 1st and 3rd quartiles (bars), and mean (carat), of event start times are shown.

(zero lag in Fig. 4.12), excluding events with missing values (270 events total). This composite, shown in the inset of Fig. 4.12c, shows higher maximum values than in the main composite of Fig. 4.12c, as expected—there is fairly large variability in the start time for precipitation, with a median of 117 min, a mean of 348 min, and an interquartile distance of 286 minutes (as shown by the bars and carat in Fig. 4.12a). In addition, 5% of the events had already started at zero lag, and these are counted as having zero start time. Since the median start time is about 2 hr, this gives a probability of *not* raining in this time of 50%. We can compare this to the probability of no rain in the next hour (given no rain at time zero) in Fig. 4.10b, which is about 0.8 at 54 mm CWV—for two hours, the probability drops to $0.8^2 = 0.64$, which is fairly consistent. Also, the precipitation rate composited over these different events peaks near the beginning, as expected from the compositing criteria, but remains fairly high throughout the period, suggesting that, once started, many events last an hour or more.

4.8 Precipitation event distributions

In the previous section, we showed that precipitation can start within a range of times during or after high CWV values. The composite in the inset of Fig. 4.12c is also likely influenced by the variability of the length of continuous precipitation events. Here we examine precipitation event length and size distributions. Peters et al. (2002) found a long power law range for event size distribution and related quantities, and hypothesized that this is associated with self-organized criticality. In Peters and Neelin (2006), the statistics of precipitation are seen to conform to those of a continuous phase transition as a function of CWV, with the critical point determined explicitly. One expects scale-free behavior with power law size distributions to occur near this critical point. The size distribution should alter substantially as a function of CWV. Peters et al. (2008) find such behavior for cluster sizes in satellite radar, although they note the caveat that the methodology of defining clusters by a threshold creates the possibility of a geometric phase transition, analogous to percolation, that need not occur at the same point as the physical phase transition for precipitation. For the western Pacific, for vertically averaged tropospheric temperature values ranging from 271 to 274 K, satellite microwave estimates give critical values of CWV ranging from 63 to 71 mm. Figure 4.4 suggests that the critical value for the precipitation pickup at Nauru is around 67 mm (Neelin et al. 2008).

Figure 4.13a shows the number density (number of counts divided by bin width) of the length of continuous precipitation events. This is a time-dimension analog of cluster size, with points defined by the condition of non-zero rain. Conditioning the distribution by CWV indeed shows a strong change in behavior, with much higher probabilities of large cluster sizes occurring for higher values of CWV. For lower CWV values, the number of long events drops off more quickly than for higher CWV values, consistent with findings for 2D cluster sizes in satellite radar (Peters et al. 2008).

Figure 4.14a shows similar behavior for number density of event size (total column of rain during event), following Peters et al. (2002). A power law range appears, but with steeper drop beyond around 5 mm. Figure 4.14b seems to show a longer continuous single power law as CWV approaches the critical value, as well as larger numbers of events just below and around critical, with still fairly large numbers of events in the bin near and above critical, agreeing with theory.

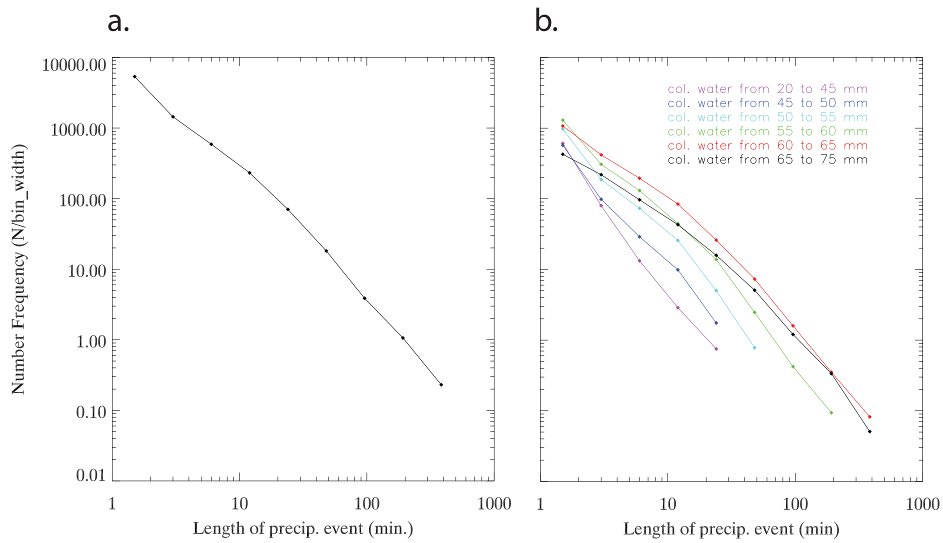

Figure 4.13: (a) Number density of the duration of continuous precipitation events. (b) The same, conditioned on gap-filled column water vapor. Bins with fewer than 10 counts are excluded.

4.9 Conclusions

Analysis of eight years of 1-min resolution microwave radiometer and optical gauge data at Nauru Island reveals that high column water vapor (CWV) is associated with a strong pick-up of precipitation even 10–12 hours in the future. CWV is found to have large autocorrelation times compared with column liquid water (CLW) and precipitation, which helps explain how CWV can have skill in predicting precipitation probability. Before precipitation events, CWV slowly rises starting about 36 hr ahead, well before there are increases in average precipitation or CLW, suggesting that there is some synoptic-scale cause of increased CWV. Within around 7 hr of the event, there is a much sharper CWV peak which is likely associated with mesoscale convective events. This supports arguments

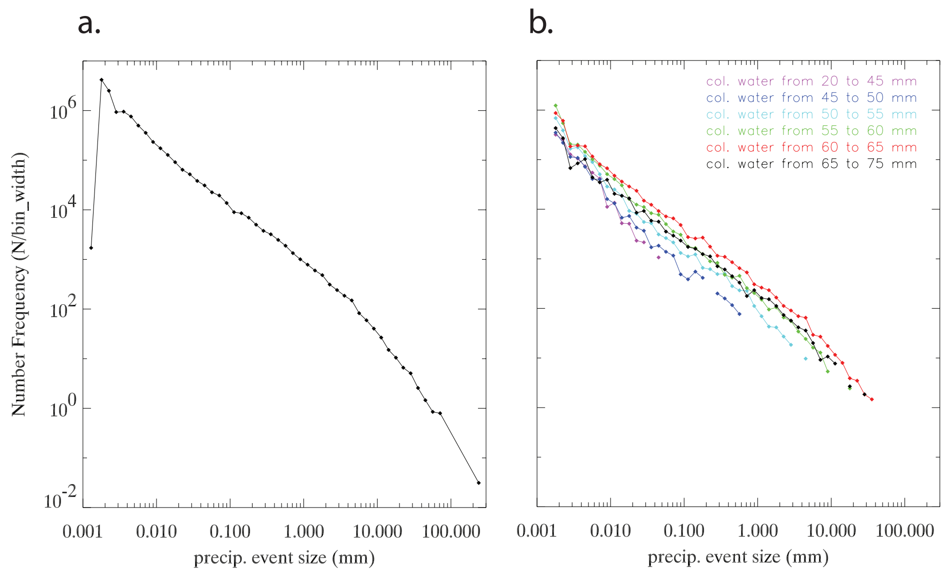

Figure 4.14: (a) Number density of event size (integrated rain amount of continuous precipitation events). (b) The same, conditioned on gap-filled column water vapor. Bins in (b) with fewer than 10 counts are excluded.

(Mapes 1993; Grabowski and Moncrieff 2004) that the interaction between convective cells, via free-tropospheric moistening and thus higher CWV, can create a positive moisture-convection feedback that allows for organization of convection on larger scales. This tendency towards scale-free distributions of convection, as seen in Peters et al. (2008), is also supported by the power law scaling of precipitation events that tends to span larger ranges for higher CWV values.

Even in periods of high CWV, probabilities of initial precipitation in a 5-min period remain low enough that there tends to be a lag before the start of the next precipitation event. High CWV, then, can be thought of as a suitable predictor variable for precipitation. This framework suggests applications to the stochastic prediction of precipitation in models—however, such a scheme would also require the accurate simulation of processes such as free-tropospheric moistening by convection and the advection of dry intrusions from the subtropics in order to predict CWV.

Chapter 5

Concluding Remarks

Observational analyses show that simplified vertical structures of temperature and moisture perturbations can be useful in representing the tropical atmosphere. In the free troposphere, a single temperature perturbation profile (derived from a distribution of moist adiabats lifted from warm and moist surface conditions) corresponds very well with data at a range of scales. This temperature structure is negatively correlated to temperature perturbations above the free troposphere (the convective cold top), likely because of simple hydrostatic pressure gradient constraints which lead to adiabatic cooling above convective heating. The boundary layer is more independent, and is linked more locally to SST.

Similarly, over half of the variance of specific humidity measured by radiosondes at Nauru in the western tropical Pacific can be explained by a single vertical structure, the first vertical principal component, which is almost perfectly correlated with column water vapor (CWV). This vertical structure has very low weighting in the subcloud layer and maximizes around 800 hPa, just above the boundary layer's fairly constant moisture and yet low (and therefore warm) enough to allow for significant amounts of water vapor at saturation. At high enough CWV, and therefore high enough moisture levels in the lower free troposphere, there is a sharp pick-up in precipitation, as seen in a few previous studies. This sharp increase can be shown to correspond to larger buoyancies of entraining plumes at high enough CWV. Entrainment profiles based on dynamic "deep inflow" due to increasing upward mass flux and continuity are especially skillful in capturing the transition to higher precipitation, since they heavily weight the environmental moisture at all lower levels where the mass flux is assumed to increase. The results are sensitive to mixing assumptions, such as freezing processes.

CWV (as measured by a microwave radiometer on Nauru), and the lower-free-tropospheric moisture that explains most of its variance, provides the tropical atmosphere with memory, since it changes relatively slowly compared with tropospheric temperature, precipitation, and column liquid water (CLW). The characteristic CWV autocorrelation time scale of over a day, larger than that of convective activity but smaller than that of SST, means that CWV can convey important information from several hours up to several days in advance. CWV increases before precipitation events on both a synoptic-scale period and a smaller mesoscale period, which is likely associated with mesoscale convective organization, such as squall lines, that in turn depends on positive feedbacks between convection and CWV. High CWV significantly increases the probability of precipitation even 10–12 hours in advance—at the same time, there is significant variability in the onset time of precipitation at high CWV, suggesting that CWV could be used as a predictor for precipitation in convective parameterizations but that there is a strong stochastic element to the relationship as well. Power law scaling of precipitation events, noted in previous studies, is seen to depend on CWV.

It is tempting to compare and try to reconcile the temperature analyses in Chapter 2 with the dependence of convection on CWV, via entrainment, described in Chapter 3. On the one hand, temperature in the free troposphere tends to follow moist adiabats calculated without considering entrainment, which would imply that undilute convective plumes dominate. On the other hand, it seems that undilute CAPE is not a good predictor of precipitation, and that significant entrainment likely occurs through a deep lower-tropospheric layer.

One possible explanation for these two views of tropical deep convection is that the main convective cells are occurring in environments with high CWV, meaning that entrainment does not significantly dilute the plumes once convection becomes strong. This may be especially true in the intertropical convergence zone (ITCZ) and other areas of organized deep convection. The free-tropospheric temperature perturbations would then be constrained by these relatively undilute moist-adiabatic convective plumes.

This view of deep convection existing mainly within areas of high CWV ties in with the explanation of precipitation as a continuous phase transition proposed in Peters et al. (2002) and Peters and Neelin (2006). One important question, addressed via temporal analysis in Chapter 4, is the scale on which these relationships take place. This is particularly relevant when considering implications for convective parameterizations. For instance, how can probabilities and perturbation profiles on the sounding scale be transferred to GCM grid scales? Furthermore, what kind of grid-scale vertical moisture and temperature structure should be desired in models with convective parameterizations?

The main quality that these results suggest for improved convective parameterizations is less dependence of convection on the boundary layer moist static energy (and undilute CAPE). Connected with this would be increased sensitivity to free-tropospheric moisture, for instance via more realistic entraining plumes as discussed above. Even at high CWV, however, schemes should simulate significant variability of precipitation onset times. Positive feedbacks between convection and precipitation, and accurate modeling of processes such as shallow convection that help determine CWV evolution, are also necessary.

Bibliography

Arakawa, A., 2004: The cumulus parameterization problem: Past present and future. *J. Climate,* **17**, 2493–2525.

Arakawa, A. and W. H. Schubert, 1974: Interaction of a cumulus cloud ensemble with the large-scale environment Part I. *J. Atmos. Sci.,* **31**, 674–701.

Arakawa, H., 1950: Analysis of the tropopause and the stratospheric field of temperature of a mature typhoon. *Pap. Meteorol. Geophys.,* **2**, 1–5.

Austin, J. M., 1948: A note on cumulus growth in a nonsaturated environment. *J. Meteor.,* **5**, 103–107.

Bellon, G. and A. Sobel, 2008: Poleward-propagating intraseasonal monsoon disturbances in an intermediate-complexity axisymmetric model. *J. Atmos. Sci.,* **65**, 470–489.

Betts, A. K., 1973: Non-precipitating cumulus convection and its parameterization. *Quart. J. Roy. Meteor. Soc.,* **99**, 178–196.

Betts, A. K. and M. J. Miller, 1986: A new convective adjustment scheme. Part II: Single column tests using GATE wave BOMEX ATEX and arctic air-mass data sets. *Quart. J. Roy. Meteor. Soc.,* **112**, 693–709.

Biasutti, M., A. H. Sobel, and Y. Kushnir, 2006: AGCM precipitation biases in the tropical Atlantic. *J. Climate,* **19**, 935–958.

Bretherton, C. S., M. E. Peters, and L. E. Back, 2004: Relationships between water vapor path and precipitation over the tropical oceans. *J. Climate,* **17**, 1517–1528.

Bretherton, C. S., M. Widmann, V. Dymnikov, J. Wallace, and I. Bladé, 1999: The effective number of spatial degrees of freedom of a time-varying field. *J. Climate,* **12**, 1990–2009.

Brown, R. G. and C. S. Bretherton, 1997: A test of the strict quasi-equilibrium theory on long space and time scales. *J. Atmos. Sci.,* **5**, 624–638.

Brown, R. G. and C. Zhang, 1997: Variability of midtropospheric moisture and its effect on cloud-top height distribution during TOGA COARE. *J. Atmos. Sci.,* **54**, 2760–2774.

Bryan, G. H. and J. M. Fritsch, 2004: A reevaluation of ice-liquid water potential temperature. *Mon. Wea. Rev.,* **132**, 2421–2431.

Cheng, M.-D., 1989: Effects of downdrafts and mesoscale convective organization on the heat and moisture budgets of tropical cloud clusters. Part II: Effects of convective-scale downdrafts. *J. Atmos. Sci.,* **46**, 1540–1564.

Chiang, J. C. H. and A. H. Sobel, 2002: Tropical tropospheric temperature variations caused by ENSO and their influence on the remote tropical climate. *J. Climate,* **15**, 2616–2631.

Ciesielski, P. E., L. Hartten, and R. H. Johnson, 1997: Impacts of merging profiler and rawinsonde winds on impacts of merging profiler and rawinsonde winds on TOGA COARE analyses. *J. of Atmos. and Oceanic Tech.,* **14**, 1264–1279.

Ciesielski, P. E., R. H. Johnson, P. T. Haertel, and J. Wang, 2003: Corrected TOGA COARE sounding humidity data: Impact on diagnosed properties of convection and climate over the warm pool. *J. Climate,* **16**, 2370–2384.

Cifelli, R. and S. Rutledge, 1994: Vertical motion structure in maritime continent mesoscale convective systems: results from a 50-MHz profiler. *J. Atmos. Sci.,* **51**, 2631–2652.

Collimore, C. C., D. W. Martin, M. H. Hitchman, A. Huesmann, and D. E. Waliser, 2003: On the relationship between the QBO and tropical deep convection. *J. Climate,* **16**, 2552–2568.

Dai, A., 2006: Precipitation characteristics in eighteen coupled climate models. *J. Climate,* **19**, 4605–4630.

Danielsen, E. F., 1993: In situ evidence of rapid, vertical, irreversible transport of lower tropospheric air into the lower tropical stratosphere by convective cloud turrets and by larger-scale upwelling in tropical cyclones. *Geophys. Res.,* **98**, 8665–8681.

de Haij, M. J., 2005: Evaluation of a new trigger function for cumulus convection. Tech. Rep. TR-276, KNMI, De Bilt, Netherlands. 117 pp.

de Roode, S. R., P. G. Duynkerke, and A. P. Siebesma, 2000: Analogies between mass-flux and reynolds-averaged equations. *J. Atmos. Sci.,* **57**, 1585–1598.

DeMott, C. A. and S. Rutledge, 1998: The vertical structure of TOGA COARE convection. Part II: Modulating influences and implications for diabatic heating. *J. Atmos. Sci.,* **55**, 2748–2762.

Derbyshire, S. H., I. Beau, P. Bechtold, J.-Y. Grandpeix, J.-M. Piriou, J.-L. Redelsperger, and P. M. M. Soares, 2004: Sensitivity of moist convection to environmental humidity. *Quart. J. Roy. Meteor. Soc.,* **130**, 3055–3080.

Divakarla, M., C. Barnet, M. D. Goldberg, L. McMillin, E. S. Maddy, W. W. Wolf, L. Zhou, and X. Liu, 2006: Validation of atmospheric infrared sounder temperature and water vapor retrievals with matched radiosonde measurements and forecasts. *J. Geophys. Res.,* **111**, D09S15.

Durre, I., R. S. Vose, and D. B. Wuertz, 2006: Overview of the Integrated Global Radiosonde Archive. *J. Climate,* **19**, 53–68.

Emanuel, K., 1991: A scheme for representing cumulus convection in large-scale models. *J. Atmos. Sci.,* **48**, 2313–2335.

Emanuel, K. A., 1994: *Atmospheric Convection* (1st ed.). New York: Oxford University Press.

Eskridge, R. E., O. A. Alduchov, I. V. Chernykh, Z. Panmao, A. C. Polansky, and S. R. Doty, 1995: A comprehensive aerological reference data set (CARDS): Rough and systematic errors. *Bull. Amer. Meteorol. Soc.,* **76**, 1759–1775.

Fritsch, J. M. and J. M. Brown, 1982: On the generation of convectively driven mesohighs aloft. *Mon. Wea. Rev.,* **110**, 1554–1563.

Gill, A. E., 1980: Some simple solutions for heat induced tropical circulation. *Quart. J. Roy. Met. Soc.,* **106**, 447–462.

Grabowski, W. W., 2003: MJO-like coherent structures: Sensitivity simulations using the Cloud-Resolving Convection Parameterization (CRCP). *J. Atmos. Sci.,* **60**, 847–864.

Grabowski, W. W., 2006: Impact of explicit atmosphere-ocean coupling on MJO-like coherent structures in idealized aquaplanet simulations. *J. Atmos. Sci.,* **63**, 2289–2306.

Grabowski, W. W. and M. W. Moncrieff, 2004: Moisture-convection feedback in the tropics. *Quart. J. Roy. Meteor. Soc.,* **130**, 3081–3104.

Grabowski, W. W. and P. K. Smolarkiewicz, 1999: CRCP: a cloud resolving convection parameterization for modeling the tropical convecting atmosphere. *Physica D,* **133**, 171–178.

Haertel, P. T. and G. N. Kiladis, 2004: Dynamics of 2-day equatorial waves. *J. Atmos. Sci.,* **61**, 2707–2721.

Highwood, E. J. and B. J. Hoskins, 1998: The tropical tropopause. *Quart. J. Roy. Meteor. Soc.,* **124**, 1579–1604.

Holloway, C. E. and J. D. Neelin, 2007: The convective cold top and quasi equilibrium. *J. Atmos. Sci.,* **64**, 1467–1487.

Holloway, C. E. and J. D. Neelin, 2008: Moisture vertical structure and tropical deep convection. *J. Atmos. Sci.*, submitted.

Holton, J. R. and A. Gettelman, 2001: Horizontal transport and the dehydration of the stratosphere. *Geophys. Res. Lett.,* **28**, 2799–2802.

Houghton, H. G. and H. E. Cramer, 1951: A theory of entrainment in convective currents. *J. Meteor.,* **8**, 95–102.

Houze, Jr., R. A., 2004: Mesoscale convective systems. *Rev. Geophys.,* **42**, RG4003.

Huesmann, A. S. and M. H. Hitchman, 2001: The stratospheric quasi-biennial oscillation in the NCEP reanalyses: Climatological structures. *J. Geophys. Res.,* **106**, 11859–11874.

Jakob, C. and A. P. Siebesma, 2003: A new subcloud model for mass-flux convection schemes: influence on triggering, updraft properties, and model climate. *Mon. Wea. Rev.,* **131**, 2765–2778.

Jensen, M. P. and A. D. Del Genio, 2006: Factors limiting convective cloud-top height at the ARM Nauru Island Climate Research Facility. *J. Climate,* **19**, 2105–2117.

Johnson, R. H. and D. C. Kriete, 1982: Thermodynamic and circulation characteristics of winter monsoon tropical mesoscale convection. *Mon. Wea. Rev.,* **110**, 1898–1911.

Jordan, C. L., 1960: Abnormally cold tropopause temperatures in the equatorial pacific. *Mon. Wea. Rev.,* **88**, 151–154.

Kalnay, E. and coauthors, 1996: The NCEP/NCAR 40-year reanalysis project. *Bull. Amer. Meteorol. Soc.,* **77**, 437–471.

Khairoutdinov, M. F. and D. A. Randall, 2001: A cloud resolving model as a cloud parameterization in the NCAR community climate system model: Preliminary results. *Geophys. Res. Lett.,* **28**, 3617–3720.

Koteswaram, P., 1967: On the structure of hurricanes in the upper troposphere and lower stratosphere. *Mon. Wea. Rev.,* **95**, 541–564.

Kuang, Z. and C. S. Bretherton, 2004: Convective influence on the heat balance of the tropical tropopause layer: A cloud-resolving model study. *J. Atmos. Sci.,* **61**, 2919–2927.

Kuang, Z. and C. S. Bretherton, 2006: A mass-flux scheme view of a high-resolution simulation of a transition from shallow to deep cumulus convection. *J. Atmos. Sci.,* **63**, 1895–1909.

LeMone, M. A. and M. W. Moncrieff, 1994: Momentum and mass transport by convective bands: Comparisons of highly idealized dynamical models to observations. *J. Atmos. Sci.,* **51**, 281–305.

LeMone, M. A. and E. J. Zipser, 1980: Cumulonimbus vertical velocity events in GATE. Part I: Diameter, intensity and mass flux. *J. Atmos. Sci.,* **37**, 2444–2457.

Liljegren, J., S.-A. Boukabara, K. Cady-Pereira, and S. Clough, 2005: The effect of the half-width of the 22-ghz water vapor line on retrievals of temperature and water vapor profiles with a 12-channel microwave radiometer. *IEEE Trans. Geosci. Remote Sens.,* **43**, 1102–1108.

Lintner, B. R. and J. D. Neelin, 2007: A prototype for convective margin shifts. *Geophys. Res. Lett.,* **34 (L05812)**, 5.

Liu, C. and M. W. Moncrieff, 2004: Effects of convectively generated gravity waves and rotation on the organization of convection. *J. Atmos. Sci.,* **61**, 2218–2227.

Liu, W. T., W. Tang, and P. P. Niiler, 1991: Humidity profiles over the ocean. *J. Climate,* **4**, 1023–1034.

Malkus, J. S., 1954: Some results of a trade-cumulus cloud investigation. *J. Meteor.,* **11**, 220–237.

Manabe, S., J. Smagorinsky, and R. F. Strickler, 1965: Simulated climatology of a general circulation model with a hydrological cycle. *Mon. Wea. Rev.,* **93**, 769–798.

Mapes, B. E., 1993: Gregarious tropical convection. *J. Atmos. Sci.,* **50**, 2026–2037.

Mapes, B. E. and P. Zuidema, 1996: Radiative-dynamical consequences of dry tongues in the tropical troposphere. *J. Atmos. Sci.,* **53**, 620–638.

Mather, J. H., T. P. Ackerman, W. E. Clements, F. J. Barnes, M. D. Ivey, L. D. Hatfield, and R. M. Reynolds, 1998: An atmospheric radiation and cloud station in the tropical western Pacific. *Bull. Amer. Meteor. Soc.,* **79**, 627–642.

Moorthi, S. and M. J. Suarez, 1992: Relaxed Arakawa-Schubert: A parameterization of moist convection for general circulation models. *Mon. Wea. Rev.,* **120**, 978–1002.

Neelin, J. D., 1997: *The physics and parameterization of moist atmospheric convection*, Chapter Implications of convective quasi-equilibrium for the large-scale flow, pp. 413–416. Dortrecht, The Netherlands: Kluwer Academic Publishers.

Neelin, J. D., C. Chou, and H. Su, 2003: Tropical drought regions in global warming and El Niño teleconnections. *Geophys. Res. Lett.,* **30 (24)**, 2275.

Neelin, J. D., M. Munnich, H. Su, J. E. Meyerson, and C. E. Holloway, 2006:

Tropical drying trends in global warming models and observations. *Proc. Nat. Acad. Sci.,* **103**, 6110–6115.

Neelin, J. D., O. Peters, J. W.-B. Lin, K. Hales, and C. E. Holloway, Accepted 2008: Rethinking convective quasi-equilibrium: Observational constraints for stochastic convective schemes in climate models. *Philos. Trans. Roy. Soc. London A*.

Neelin, J. D. and N. Zeng, 2000: A quasi-equilibrium tropical circulation model—formulation. *J. Atmos. Sci.,* **57**, 1741–1766.

Neggers, R., J. D. Neelin, and B. Stevens, 2007: Impact mechanisms of shallow cumulus convection on tropical climate dynamics. *J. Climate,* **20**, 2623–2642.

Neggers, R. A. J., A. P. Siebesma, and H. J. J. Jonker, 2002: A multiparcel model for shallow cumulus convection. *J. Atmos. Sci.,* **59**, 1655–1668.

Nicholls, M. E., R. A. Pielke, and R. W. Cotton, 1991: Thermally forced gravity waves in an atmosphere at rest. *J. Atmos. Sci.,* **48**, 1869–1884.

Numaguti, A., R. Oki, K. Nakamura, K. Tsuboki, N. Misawa, T. Asai, and Y.-M. Kodama, 1995: 4-5-day-period variation on low-level dry air observed in the equatorial western Pacific during the TOGA COARE IOP. *J. Meteor. Soc. Japan,* **73**, 267–290.

Ogura, Y. and H. R. Cho, 1973: Diagnostic determination of cumulus cloud populations from observed large-scale variables. *J. Atmos. Sci.,* **30**, 1276–1286.

Pan, H.-L. and W. Wu, 1995: Implementing a mass flux convective parameterization package for the NMC medium-range forecast model. Office Note 409, NOAA/NMC/NCEP, Camp Springs, MD. 43 pp.

Pandya, R., D. Durran, and C. Bretherton, 1993: Comments on "Thermally forced gravity waves in an atmosphere at rest". *J. Atmos. Sci.,* **50**, 4097–4101.

Pandya, R. E. and D. R. Durran, 1996: The influence of convectively generated thermal forcing on the mesoscale circulation around squall lines. *J. Atmos. Sci.,* **53**, 2924–2951.

Parsons, D. B., K. Yoneyama, and J.-L. Redelsperger, 2000: The evolution of the tropical western Pacific atmosphere-ocean system following the arrival of a dry intrusion. *Quart. J. Roy. Meteor. Soc.,* **126**, 517–548.

Peters, O., C. Hertlein, and K. Christensen, 2002: A complexity view of rainfall. *Phys. Rev. Lett.,* **88**, 018701.

Peters, O. and J. D. Neelin, 2006: Critical phenomena in atmospheric precipitation. *Nature Physics,* **2**, 393–396.

Peters, O., J. D. Neelin, and S. W. Nesbitt, 2008: Mesoscale convective systems and critical clusters. *J. Atmos. Sci.*, submitted.

Plumb, R. A. and R. C. Bell, 1982: A model of the quasibiennial oscillation on an equatorial beta-plane. *Quart. J. Roy. Meteor. Soc.,* **108**, 335–352.

Randall, D. A. and D. M. Pan, 1993: Implementation of the Arakawa-Schubert cumulus parameterization with a prognostic closure. In K. A. Emanuel and D. J. Raymond (Eds.), *The Representation of Cumulus Convection in Numerical Models of the Atmosphere*, Volume 46 of *Meteorological Mono-*

graphs, pp. 137–144. Washington DC: American Meteorological Society.

Raymond, D. J., 1997: Boundary layer quasi-equilibrium (BLQ). In R. K. Smith (Ed.), *The Physics and Parameterization of Moist Atmospheric Convection*, pp. 387–397. Kluwer Academic Publishers.

Raymond, D. J., 2000: Thermodynamic control of tropical rainfall. *Quart. J. Roy. Meteor. Soc.,* **126**, 889–898.

Raymond, D. J. and A. M. Blyth, 1992: Extension of the stochastic mixing model to cumulonimbus clouds. *J. Atmos. Sci.,* **49**, 1968–1983.

Reid, G. C., 1994: Seasonal and interannual temperature variations in the tropical stratosphere. *J. Geophys. Res.,* **99**, 18923–18932.

Reid, G. C. and K. S. Gage, 1996: The tropical tropopause over the western Pacific: Wave driving, convection, and the annual cycle. *J. Geophys. Res.,* **101**, 21,233–21,241.

Reid, G. C., K. S. Gage, and J. R. McAfee, 1989: The thermal response of the tropical atmosphere to variations in equatorial Pacific sea surface temperature. *J. Geophys. Res.,* **94**, 14705–14716.

Robe, F. R. and K. A. Emanuel, 1996: Moist convective scaling: Some inferences from three-dimensional cloud ensemble simulations. *J. Atmos. Sci.,* **53**, 3265–3275.

Robinson, F. J. and S. C. Sherwood, 2006: Modeling the impact of convective entrainment on the tropical tropopause. *J. Atmos. Sci.,* **63**, 1013–1026.

Schumacher, C. and R. A. Houze, Jr., 2003: Stratiform rain in the tropics as seen by the TRMM Precipitation Radar. *J. Climate,* **16**, 1739–1756.

Scorer, R. S., 1957: Experiments on convection of isolated masses of buoyant fluid. *J. Fluid Mech.,* **2**, 583–594.

Sherwood, S. C., 1999: Convective precursors and predictability in the tropical western Pacific. *Mon. Wea. Rev.,* **127**, 2977–2991.

Sherwood, S. C., T. Horinouchi, and H. A. Zeleznik, 2003: Convective impact on temperatures observed near the tropical tropopause. *J. Atmos. Sci.,* **60**, 1847–1856.

Siebesma, A. P., P. M. M. Soares, and J. Teixeira, 2007: A combined eddy diffusivity mass flux approach for the convective boundary layer. *J. Atmos. Sci.,* **64**, 1230–1248.

Slingo, J. M., K. R. Sperber, J. S. Boyle, J.-P. Ceron, and coauthors, 1996: Intraseasonal oscillation in 15 atmospheric general circulation models: Results from an AMIP diagnostic subproject. *Climate Dynamics,* **12**, 325–357.

Sobel, A. H. and J. D. Neelin, 2006: The boundary layer contribution to intertropical convergence zones in the quasi-equilibrium tropical circulation model framework. *Theoretical and Computational Fluid Dynamics,* **20**, 323–350.

Sobel, A. H., S. E. Yuter, C. S. Bretherton, and G. N. Kiladis, 2004: Large-scale meteorology and deep convection during TRMM KWAJEX. *Mon. Wea. Rev.,* **132**, 422–444.

Stokes, G. M. and S. E. Schwartz, 1994: The Atmospheric Radiation Measurement (ARM) Program: Programmatic background and design of the cloud and radiation testbed. *Bull. Amer. Meteor. Soc.,* **75**, 1201–1221.

Stommel, H., 1947: Entrainment of air into a cumulus cloud. *J. Meteor.,* **4**, 91–94.

Susskind, J., C. D. Barnet, and J. M. Blaisdell, 2003: Retrieval of atmospheric and surface parameters from AIRS/AMSU/HSB data in the presence of clouds. *IEEE Trans. Geosci. Remote Sensing,* **41**, 390–409.

Teitelbaum, H., M. Moustaoui, C. Basdevant, and J. R. Holton, 2000: An alternative mechanism explaining the hygropause formation in tropical region. *Geophys. Res. Lett.,* **27**, 221–224.

Thuburn, J. and G. C. Craig, 2002: On the temperature structure of the tropical substratosphere. *J. Geophys. Res.,* **107**, 4017.

Tobin, D., H. E. Revercomb, R. O. Knuteson, B. Lesht, L. L. Strow, S. E. Hannon, W. F. Feltz, L. Moy, E. J. Fetzer, and T. Cress, 2006: Atmospheric radiation measurement site atmospheric state best estimates for atmospheric infrared sounder temperature and water vapor retrieval validation. *J. Geophys. Res.,* **111**, D09S14.

Tompkins, A. M., 2001a: Organization of tropical convection in low vertical wind shears: The role of cold pools. *J. Atmos. Sci.,* **58**, 1650–1672.

Tompkins, A. M., 2001b: Organization of tropical convection in low vertical wind shears: The role of water vapor. *J. Atmos. Sci.,* **58**, 529–545.

Trenberth, K. E. and L. Smith, 2006: The vertical structure of temperature in the Tropics: Different flavors of El Niño. *J. Climate,* **19**, 4956–4970.

Webster, P. J. and G. L. Stephens, 1980: Tropical upper-tropospheric extended clouds: Inferences from winter MONEX. *J. Atmos. Sci.,* **37**, 1521–1541.

Westwater, E. R., B. B. Stankov, D. Cimini, Y. Han, J. A. Shaw, B. M. Lesht, and C. N. Long, 2003: Radiosonde humidity soundings and microwave radiometers during Nauru99. *J. Atmos. Oceanic Technol.,* **20**, 953–971.

Wu, W., A. E. Dessler, and G. R. North, 2006: Analysis of the correlations between atmospheric boundary-layer and free-tropospheric temperatures in the tropics. *Geophys. Res. Lett.,* **33**, L20707.

Xu, K.-M. and K. A. Emanuel, 1989: Is the tropical atmosphere conditionally unstable? *Mon. Wea. Rev.,* **117**, 1471–1479.

Yoneyama, K., 2003: Moisture variability over the tropical western Pacific ocean. *J. Meteor. Soc. Japan,* **81**, 317–337.

Yu, J.-Y., C. Chou, and J. D. Neelin, 1998: Estimating the gross moist stability of the tropical atmosphere. *J. Atmos. Sci.,* **55**, 1354–1372.

Zhang, G. J. and N. A. McFarlane, 1995: Sensitivity of climate simulations to the parameterization of cumulus convection in the Canadian Climate Centre general circulation model. *Atmos.-Ocean.,* **33**, 407–446.

Zhang, G. J. and H. Wang, 2006: Toward mitigating the double ITCZ problem in NCAR CCSM3. *Geophys. Res. Lett.,* **33**, L06709.